ABSTRACT

Title of dissertation: THE PYROCONVECTIVE PATHWAY FOR STRATOSPHERIC WATER VAPOR AND AEROSOL

George P. Kablick III, Doctor of Philosophy, 2019

Dissertation directed by: Professor Zhanqing Li
Department of Atmospheric & Oceanic Science
Earth System Science Interdisciplinary Center

A detailed analysis of pyrocumulonimbus (pyroCb) cases is presented that explores their convective dynamics, stratospheric plume characteristics and downstream radiative effects. Satellite observations in conjunction with ground station data and radiative transfer models are used to quantify the impact that pyroCbs have on localized stratospheric aerosol and water vapor. The initial meteorological and fire conditions are explored using a cloud- and aerosol-resolving model to determine the dominant mechanics driving the convection and their effects on microphysics. Results show that intense sensible heat fluxes are the dominant convection trigger over a wildfire in an unstable atmosphere. Direct observations by cloud profiling radar of the active convective stage of a pyroCb are analyzed for the first time, and comparisons with non-pyro meteorological deep convection in the same vicinity and season show that the pyroCb has an extreme delay in the growth of precipitation-sized cloud droplets to altitudes above the homogeneous freezing level.

Stratospheric aerosol plume morphology is analyzed for several cases, and an empirical heat accumulation efficiency model is developed to describe observed radiatively-induced self-lofting in the stratosphere. The model results suggest pyroCb aerosol plumes are $\sim 30\%$ efficient at converting shortwave radiative heating into sensible heating, thereby driving buoyant uplift once injected into the stratosphere. PyroCbs directly inject H_2O vapor into the stratosphere, which is shown to be significantly large for two separate cases. The cloud-resolving model confirms a previous hypothesis that uniquely small ice particle microphysics can enhance stratospheric H_2O in detrained convective anvils. Satellite retrieval evidence suggests plume water vapor anomalies are a result of inefficient removal of small ice particles within the detrained pyroCb anvil. Model-injected total water—represented as the sum of all ice and absolute humidity—shows at least 30% of H_2O survives the convective detrainment stage, and diminishes within the evolving plume over the observation period when using satellite observations of H_2O as a benchmark. In the plumes presented herein, pyroCb H_2O anomalies are as large as 4 ± 3 ppmv above the background in the lower stratosphere. Detailed line-by-line radiative transfer simulations suggest that these anomalies produce an instantaneous longwave radiative forcing up to $+1.0$ W m^{-2} at the tropopause.

THE PYROCONVECTIVE PATHWAY FOR STRATOSPHERIC WATER VAPOR AND AEROSOL

by

George P. Kablick III

Dissertation submitted to the Faculty of the Graduate School of the
University of Maryland, College Park in partial fulfillment
of the requirements for the degree of
Doctor of Philosophy
2019

Advisory Committee:
Professor Zhanqing Li, Chair
Michael Fromm, Ph.D.
Professor Russell Dickerson
Professor Ross Salawitch
Professor George Hurtt

Dedication

For my parents and grandparents.

Acknowledgments

I'd like to thank my research advisor Zhanqing Li for providing wisdom, support, and the opportunity to pursue my Ph.D. research. I'm grateful for the encouragement. I'm also deeply grateful to Mike Fromm at the Naval Research Lab who has been a great friend and mentor. I'd also like to acknowledge Professors Russ Dickerson, Ross Salawitch and George Hurtt for serving on my dissertation committee.

There are numerous additional people who have helped me throughout this research, either through providing material support or beneficial discussion. They include, Seoung Soo Lee, Dave Peterson, Gerald Nedoluha, Alyn Lambert, Michael Schwartz, Steve Miller, Hugh Pumphrey, Pete Caffrey, Andrew Jongeward, and many others. Thank you all.

Finally, I would like to thank my wife Meredith for her unending patience, fortitude and encouragement, and also my children Lily and Peter for their comic relief.

Statement of Originality

This dissertation contains original research from which these major conclusions can be drawn:

1. Cloud radar profiles through active an active pyroCb show precipitation formation and droplet growth are suppressed in supercooled air until reaching the homogeneous freezing level.

2. PyroCb plumes injected into the stratosphere enhance local water vapor mixing ratios, and unique ice microphysics within detrained anvils probably contribute to this enhancement.

3. Empirical results using convective cloud modeling tests show there needs to be $\sim 30\%$ survival of total water in the stratosphere from ice and vapor to match observations.

4. Radiative-induced diabatic self-lofting is described with a heat accumulation model based on the first law of thermodynamics, and an empirical efficiency parameter to account for conversion of solar heating to buoyant uplift through temperature increases. The efficiency for three different cases is found to be $\sim 30\%$.

5. Global water vapor enhancements in the stratosphere are quantified for an extreme pyroCb event, and tropopause radiative forcing from this enhancement is found to be $+1.0$ W m^{-2}.

All of these conclusions are based on research that has been conducted by myself, either as the lead author on three papers or a co-author on two additional papers:

Kablick, G., M. Fromm, S. Miller, P. Partain, D. Peterson, S. Lee, Y. Zhang, A. Lambert, Z. Li (2018), The Great Slave Lake pyroCb of 5 August 2014: observations, simulations, comparisons with regular convection, and impact on UTLS water vapor, *J. Geophys. Res., 123*, (21), 12–332. (Chapter 2, 3)

Fromm, M., R. McRae, J. Sharples, and **G. Kablick** (2012), Pyrocumulonimbus Pair in Wollemi and Blue Mountains National Parks, 22 November 2006, *Aust. Meteorol. Ocean. J.*, (62), 117–126. (Chapter 2)

Kablick, G., M. Fromm, Z. Li (2019), Self-Lofting of Biomass Burning Plumes within the Stratosphere, *to be submitted to Mon. Wea. Rev.*. (Chapter 4)

Peterson, D., J. Campbell, E. Hyer, M. Fromm, **G. Kablick**, J. Cossuth, M. DeLand, (2018), Wildfire-driven thunderstorms cause a volcano-like stratospheric injection of smoke, *npj Clim. Atmos. Sci.*, (1:30) (Chapter 4)

Kablick, G., M. Fromm, M. Schwartz, H. Pumphrey, G. Nedoluha, Z. Li (2019), Radiative Effects of an Unprecedented Stratospheric Intrusion of Water Vapor from Pyroconvection, *to be submitted to J. Climate*. (Chapter 5)

Table of Contents

Dedication ii

Acknowledgements iii

Statement of Originality iv

List of Tables viii

List of Figures ix

List of Abbreviations xvii

1 Introduction 1
- 1.1 UTLS Water Vapor and Climate . . . 3
- 1.2 Tropopause-Involved UTLS H_2O Trends . . . 8
  - 1.2.1 Deep Convection and Ice Microphysics . . . 11
- 1.3 Pyrocumulonimbus . . . 14
- 1.4 Objectives . . . 19

2 PyroCb Events 21
- 2.1 Case Studies . . . 22
  - 2.1.1 Great Slave Lake 2014 . . . 22
  - 2.1.2 Pacific Northwest Event 2017 . . . 26
- 2.2 Properties of Active PyroCb . . . 30
  - 2.2.1 Weather and Fire Conditions . . . 36
  - 2.2.2 PyroCb and Cb Comparisons . . . 45
- 2.3 Detrained Stratospheric Plume Properties . . . 52

3 Cloud-Aerosol Modeling of Active PyroCb Convection 61
- 3.1 Model Experiments . . . 61
- 3.2 Results . . . 64

4 Diabatic-Lofting of Injected PyroCb Plumes 70
4.1 Stratospheric Injection Mass 72
4.2 Plume Rise Observations and Simulations 80
4.2.1 Satellite Observations 80
4.2.2 Modeling Plume Rise 87

5 Radiative Effects of Residual PyroCb-Injected UTLS Water Vapor 100
5.1 Observed Water Vapor Enhancements 101
5.2 Line-by-Line Simulations 108
5.2.1 Fixed Anomaly Results 110
5.2.2 Lagrangian Anomaly Results 116
5.3 The Big Picture 120

6 Summary of Work, Conclusions, and a Future Direction for PyroCb Impact Studies 124
6.1 PyroCb Convection and Cloud Modeling 124
6.2 Stratospheric PyroCb Aerosol 127
6.3 Water Vapor Forcing 129
6.4 Future Work 130

Bibliography 132

List of Tables

2.1 June–August 2014 deep convective core cases found using the modified CloudSat identification algorithm described in the text within a rectangular region between 50–65°N and 103–120°W, including the GSL pyroCb and Alberta Cb. 49

4.1 2017 PNE pyroCb plume potential temperature observations (θ) and model-predicted (θ_ε) using various efficiency parameters (ε). Also shown are CALIOP stratospheric AOD and SBDART radiative heating rate anomalies (ΔQ) in K day^{-1}. $n\Delta Q$ is the maximum temperature change assuming a steady state over n days between observations (K; only shown where $n > 1$, otherwise $\Delta Q = n\Delta Q$). Last row gives total change in θ and each θ_ε. θ_ε values in bold are closest match to plume θ. 92

4.2 As in Table 4.1, but for the 2014 GSL pyroCb plume. 95

4.3 As in Table 4.1, but for the 2009 Black Saturday pyroCb plume. . . . 97

4.4 PyroCb events with significant observational evidence of diabatic plume rise that have been published in peer-reviewed literature. Included are three additional cases not analyzed herein (all values of z in km and θ in K). 99

List of Figures

1.1 Perturbations and radiative transfer through AFGL midlatitude atmosphere. Model profiles in each panel show (a) temperature (black) and H_2O (blue), where the solid line is the standard mixing ratio and dashed/dotted lines are the +1 or −1 ppmv perturbations; (b) air density (black) and the percentage WVMR perturbation (blue); and (c) longwave fluxes (upward; red, downward; blue, net; black) and cooling rates (green). The eight lines in (d) are the flux and cooling rate differences between the +1 or −1 ppmv perturbations on the standard model results shown in (c). 7
1.2 Tropospheric phenomenon known to interact with the UTLS. 17

2.1 Visible imagery of the GSL pyroCb over the course of three hours on 5 August as seen by Aqua MODIS (a, e), Terra MODIS (b, d) and NPP VIIRS (c, f). Yellow star is location of the Buffalo Junction surface site, across which the active pyroCb moved. Red line in (e) is track of CALIOP and CloudSat (see Figure 2.6). Photographs in (g–h) taken by Mike Smith of Yukon Wildland Fire Management, and are used with permission. 24
2.2 The PNE pyroCb event at approximately 20:00 local time on 12 August 2017 as viewed by AVHRR. (a) BT_{11} and (b) BT_3 showing the typical pyroCb signature cold cloud tops in the thermal channel and warm cloud tops in the near infrared (discussed in Section 2.2. Shown here are four pyroCb anvils originating from three fires discussed in the text. Fire locations are displayed as red pixels in (b). Images created by Scott Bachmeier and released to public domain (CIMSS pyroCb blog). 27
2.3 (a–c) VIIRS images of the Pacific Northwest during the three days centered on the PNE (red dots are fire locations). Rows (d–f) are OMPS UVAI images on the days that the plume moved northwestward around a high pressure Omega-block pattern, "gathered" in northern Canada, and subsequently moved southeastward. OMPS images created by Colin Seftor and used with permission. 29

2.4 As in Figure 2.1c and 2.1f, but for VIIRS 3.7 μm (a, b) and 10.8 μm (c) BT of the GSL pyroCb. All values are in K. Images (b) and (c) are $\sim$ 100 minutes after a) on 5 August. Fire 14WB-025 is denoted with yellow arrow in (a) and (b). Note the darker color of the pyroCb anvil (yellow circle) in (b) as compared with the lighter cirrus clouds to the northwest (upper left of images) as the convection becomes detached from the fire, indicating an extremely small and narrow ice particle size distribution. 31
2.5 Aqua MODIS BT_{11} of the GSL pyroCb (a) and the concurrent Alberta Cb to the south (b) at 20:20 UTC. The red lines show the nadir ground track of CALIOP and CloudSat. Note the "cold-U" shape of the pyroCb outflow anvil with warmer temperatures corresponding to the central overshooting top. The Cb shows no such structure even though the minimum brightness temperatures are similar: -62 °C and -64 °C for pyroCb and Cb, respectively. 32
2.6 CALIOP 532 nm backscatter (top row) and CloudSat 94 GHz radar reflectivity (bottom row) at the 20:20 UTC intersection of the active GSL pyroCb (a,c) and Alberta Cb (b,d) cores (see red line in Figure 2.1e, 2.5a for pyroCb and Figure 2.5b for Cb). CALIOP shows that the GSL pyroCb has a highly attenuating anvil cloud with overshooting top near 14 km (a), and CloudSat indicates strong echoes in the mid-levels, but weak echoes near the surface, and no echoes between 13–14 km (c). The yellow dashed line indicates the CALIOP cloud top in both panels. Conversely for the Alberta Cb, CALIOP (b) and CloudSat (d) have similar cloud top heights, and the radar reflectivity shows a complex vertical structure of with large reflectivity near the cloud top and extending down to the surface. Also shown are the 0 °C and -38 °C isotherms from ERA-I reanalysis at both locations. 34
2.7 Synoptic-scale conditions from NARR showing winds and geopotential heights at 300 hPa (a), relative humidity and winds at 850 hPa (b), and surface frontal analysis (c). "$\times$" symbols denote location of GSL pyroCb. 36
2.8 Map of fire perimeters (yellow with black outlines) and ground observation sites (black circles) maintained by the Government of the Northwest Territories. Fire 14WB-025 spawned the GSL pyroCb. Data from three of the observation sites shown in Figure 2.9. Red dot marks location of photographs in Figure 2.1g,h. 38
2.9 Time series of temperature and relative humidity (a–c; black and blue, respectively), wind speed (d–f) and both instantaneous and 24-hour accumulated rainfall (g–h; orange and blue, respectively). Red vertical line on time series plots denotes time of pyroCb. The pyroCb moved directly over the Buffalo Junction Station (a,d,g). Ground-site data courtesy of Franco Nogarin of the Government of the Northwest Territories. 39

2.10 36-hour time-series of normalized hourly GOES-15 FRP (red) and the mean estimated fire kinetic temperature (black) centered on the time of pyroCb (green line). Note the large fire temperatures and peak in FRP just before initiation. Gray shading is local nighttime. Gaps in FRP are due to invalid retrievals by the WF_ABBA algorithm likely due to weak fire output in the local evening/morning. 40
2.11 Interpolated 18:00 UTC sounding for the GSL pyroCb. Red horizontal lines show CloudSat and CALIOP observed cloud boundaries. Atmospheric temperature between $\sim$ 900–1000 hPa is shown adjusted by using average ground station T_s (red dashed line), producing CAPE=1985 J kg^{-1} and CIN=1160 J kg^{-1} (blue and gray shading, respectively). Thick black horizontal lines show LCL and EL also computed with T_s. Green line is mixed-layer LCL (lowest 50 hPa) computed with T_s adjustment. CIN is limited to pressures between EL and the observed overshoot altitude in lower stratosphere. Dark yellow bar between 3.7–4.2 km is convective cloud base height range from "Full Simulation" modeling experiment (Chapter 3). . . . 43
2.12 (Left) CloudSat reflectivity and CALIOP β'_{532} through the Wollemi and Grose Valley pyroCb columns. (right) Trajectories initialized at the high OMI UVAI values through the ground track of these two nadir-looking instruments (black line) with the MODIS fire hot spots (orange outlines). This figure adapted from Figures 3 and 6 of *Fromm et al.* (2012). 46
2.13 CloudSat horizontal-mean reflectivity profiles plotted as a function of height above the LCL through deep convection during the period 1 June–31 August 2014 near the GSL pyroCb. Shown in (a) are the GSL pyroCb (blue), Alberta Cb (red) and the additional 15 meteorological DCC profiles identified. Blue and red shading represent the standard deviation about the mean for GSL pyroCb and Alberta Cb. Horizontal lines in a) show FL (dot-dashed), HFL (dashed), EL (solid) and CloudSat cloud top (dotted) for both the pyroCb and Cb. Green line is the radar reflectivity from ARW Full Simulation pyroCb model run. (b) Black line shows the linear regression slope of mean reflectivity profiles between these thermodynamic levels and gray shading shows the standard deviation for all cases. Individual regressions of the GSL pyroCb and Alberta Cb cases are shown in blue and red, respectively. 48
2.14 5-hourly GOES-15 IR brightness temperature imagery starting at 20:30 UTC on 08/05 comparing the anvil lifecycle of the GSL pyroCb (blue arrows) and Alberta Cb (red arrows). 53

2.15 (Top) Map of HYSPLIT trajectory showing intersections with relevant A-Train orbits. Segments are labeled A–I, and the date, segment time stamp and corresponding HYSPLIT hour are given in the inset table. (A–I) CALIOP VFM curtains showing the "stratospheric features" in black with MLS water vapor anomalies overlaid as colored rectangles (% relative to local climatology). Black dashed line is 2.5 PVU dynamical tropopause and green contours are potential temperature (K) from ERA-I reanalysis. Abscissae of A–I are in degrees of latitude, and orange vertical lines bound the curtain profiles used in Figures 2.17, 2.18. Corresponding β'_{532} curtains are shown in Figure 2.16. 55
2.16 As in Figure 2.15, but showing the β'_{532} instead of "stratospheric features" identified using the VFM product. Note the altitude range is extended compared with 2.15 to show more of the backscattering differences between strongly attenuating clouds in the troposphere with the stratospheric pyroCb plume. 56
2.17 MLS water vapor profiles through the pyroCb plume (red lines) observations shown in Figure 2.15. Blue lines are the profiles of background WVMR from the 2005–2014 JJA gridded climatology that fall within the region bounded by orange lines in panels A–I in Figure 2.13, blue shading shows the standard deviation of these background profiles. The gray dashed lines delineate the potential temperature boundaries of the plume over the course of its observable lifetime. 58
2.18 Mean values of MLS WVMR anomalies and IWC (black and blue lines, respectively) and median CALIOP δ_{532} (red lines) over the two-week observable lifetime of the GSL pyroCb plume. Each MLS point in this time series represents a per-profile vertical mean between 360–400 K for measurements encompassing the plume (dashed lines in Figure 2.14), and each CALIOP point is the median value for the entire "stratospheric feature" between 360–400 K. 59

3.1 ARW Full Simulation ice particle mixing ratio within the cirrus outflow at the equilibrium level ($\sim$ 13 km) during the mature stage of pyroconvection (approximately 3 hours after convection began). Red circle denotes fire hot-spot location used to initialize the simulation. Compare with VIIRS image in Figure 2.1f. 65
3.2 Profiles from four pyroCb model simulations showing the averaged vertical distributions of the a) spatiotemporally-averaged updraft mass fluxes, and b) ice mass densities. See text for descriptions of the four simulations. 66

3.3 Profiles of WVMR spatiotemporally averaged for each simulation for all cloud regions within the domain (solid lines), and surviving water post-detrainment (dashed lines), estimated here to be 30%. The latter includes vapor contributions from ice sublimation and existing absolute humidity. The MLS observation during the active pyroCb—when no WVMR enhancement is yet present—is shown as a gray line as a reference to the background profile. 68

4.1 The first reliable CALIOP β'_{532} intersection with PNE stratospheric plume on 14 August (∼1.5 days after injection) at 11:30 UTC. Overlaid are MLS observations of CO. Maximum CO mixing ratio observation is > 670 ppmv (white "×" near 70.5 °N). Columns of light vertical shading labeled 1 and 2 are locations used to assess total aerosol extinction for comparison with OMPS UVAI (see Figures 4.2 and 4.3). 76

4.2 Profiles of scattering ratio (left) and derived non-molecular extinction (aerosol particulates, right) from the PNE plume intersection in Figure 4.1. (a, b) correspond with column 1 and (c, d) with column 2. Vertical integration of plume extinction for tropopause height >11.5 km yields AOD $\simeq$ 3.5 and $\simeq$ 1.5, respectively. 77

4.3 Empirical results of mass estimation of the PNE plume shown in Figures 4.1 and 4.2 showing the a) along-track AOD derivation and b) simulated UVAI using the 330 nm and 390 nm channels. Red lines show a) the value of "total optical attenuation" of the downward-looking vertical CALIOP instrument (note a majority of the plume between 66-73 °N has fully attenuated the lidar) and b) stratospheric UVAI threshold. There is good agreement with the plume's simulated UVAI $\geq$ 15 and the stratospheric component of the CALIOP observation in 4.1. 79

4.4 CALIOP/MLS observation of the PNE plume on 3 September 2017 at 21:00 UTC (∼ 3 weeks post-injection). Location of CO maximum (∼ 170 ppbv) and large β'_{532} values show plume has risen at least 10 km above the injection height (white dashed line). 81

4.5 Hand-drawn trajectories of three sections of the 2017 PNE plume tracked using the dual MLS H_2O/CO threshold. Panel (a) shows the start date (12 September) when the plume could be sufficiently identified as three independently moving sections. The "1 Month" trajectory between the 12 August pyroCb date and the plume locations on 12 September is an approximation based on the plume tracking method described in the text. Panels (b–d) show termination dates of each plume section's observability. Colored dots are the GPH of the MLS plume observation (bottom colorbar). Inset in panel (d) focuses on the area over the mid-Atlantic where the Square plume completed a circumnavigation; locations are marked when observations occurred between 29 September and 2 October (bearing east toward west) and 11–25 November (bearing from southeast toward northwest, then abruptly shifting toward northeast). 83
4.6 Potential temperatures of all northern hemisphere MLS thresholded observations during the first three months of the PNE plume evolution. A constant H_2O threshold of 7 ppmv is applied with diminishing CO thresholds as the plume ages. The vertical dashed line marks the point at which the plume separates over central Asia, and the three dashed lines emanating from this time show the different ascent rates of three tracked plume sections. 85
4.7 Illustration of pyroCb smoke plume evolution from onset through decay. Left: available observations are used to define the injection-θ at a specific location and time. Middle: the NP-phase is when the earliest-possible 3D observations of the plume can be characterized, and coincides with strong diabatic-lofting potential due to high concentrations of absorbing aerosol. Right: the EP-phase is the period during which advection and dispersion are reducing the concentration of aerosol to the point of non-observability, and diabatic-lofting potential is rapidly diminishing. 86
4.8 (a) Observed and modeled diabatic rise of the PNE Square plume (see red trajectory in Figure 4.5). Blue "×" show the potential temperature of the CALIOP-observed plume centroid with error bars denoting the upper and lower backscatter boundaries, augmented with MLS plume observations of colocated HCN/CO maxima (green dots). Simulation of radiatively-forced diabatic lofting for various ε are shown over observations. Prince George radar echotop-based injection $\theta = 370$ K is noted. (b) The stratospheric AOD derived from CALIOP extinction. 91
4.9 As in Figure 4.8, but for the GSL pyroCb plume. NP phase is shorter than the 2017 PNE case before stratospheric ascent is observed. Also, this plume was only trackable for approximately two weeks, and had a much smaller total $\Delta\theta$. Injected plume $\theta = 357$ K, averaged over depth of CALIOP observation is noted. 94

4.10 As in Figure 4.8, but for the 2009 Black Saturday pyroCb plume. Green "○" in this case are MLS observations colocated HCN/CO maxima to fill CALIOP gap (light blue vertical bar between mid-February to mid-March). Blue "×" are CALIOP observations, and black "×" is surface lidar observation from São José dos Campos, Brazil. Melbourne surface radar echotop-based $\theta = 370$ K is noted. . 96

5.1 August 2017 histograms of all Aura MLS H_2O observations in the Northern Hemisphere lower stratosphere using coincident CO thresholds (a) $\geq$ 20 ppbv, (b) $\geq$ 30 ppbv, (c) $\geq$ 40 ppbv, (d) $\geq$ 70 ppbv. Count densities shown for each 1 km layer between GPH = 15-25 km for observations constrained by $380 \leq \theta \leq 600$ K. Note logarithmic scale. Observations to the left of 7 ppmv threshold (dashed line) were ignored for plume identification used in Chapter 4. 102
5.2 As in Figure 5.1 but for September 2017. 104
5.3 As in Figure 5.1 but for October 2017. 105
5.4 As in Figure 5.1 but for November 2017. 106
5.5 (left column) Aura MLS WVMR anomalies (red contours) and fixed local climatologies (black contours) within the three 2017 PNE pyroCb plumes after the 12 September separation. All contours in ppmv. (right column) Longwave LBLRTM heating rate anomalies throughout the troposphere and lower stratosphere computed from these observations. Square plume (top row), Triangle plume (middle row) and Circle plume (bottom row). Vertical gray bars indicate where MLS missed observations. 111
5.6 Fixed Anomaly H_2O longwave radiative heating (left column) and radiative heating anomalies (right column) for the individual dates of the three plume sections. Note the significant cooling within and above the plume and mild warming below the plume to the tropopause. 114
5.7 TOA (left) and tropopause-level (right) longwave RF using the H_2O Fixed Anomalies from Figure 5.5. Note the Square plume is confined to the tropics for most of its observable duration, and has a negative RF at TOA (a decrease in OLR), whereas the Triangle and Circle plumes are in the mid-latitudes, and have a positive RF at TOA. In all cases, there is a positive RF at the tropopause. 116
5.8 As in Figure 5.5, but vapor concentration anomalies and radiative heat flux differences are calculated using the Aura MLS Lagrangian H_2O climatology. 117
5.9 As in Figure 5.6, but for the Lagrangian climatology. (a) Note the Square plume has three general Q_{LW} profiles, and (c) the Triangle has two as these plumes move to different latitude bands through summer and winter months. 118
5.10 As in Figure 5.7, but for the Lagrangian climatology. 120

5.11 The global Aura MLS H_2O/CO data record with constant thresholds. All potential temperature observations are shown for the a) northern hemisphere and b) southern hemisphere where MLS observes $H_2O \geq 7$ ppmv and CO ≥ 70 ppbv. Highlighted are the 2017 PNE plume in the northern hemisphere and the lack of 2009 Black Saturday signal in the southern hemisphere. Note the annual signals between $380 < \theta < 400$ K are from the Monsoon and those between $550 < \theta < 600$ K are from each hemispheres polar vortex. 122

List of Abbreviations

a.m.s.l.	above mean sea level
AVHRR	Advanced Very High Resolution Radiometer
BT	brightness temperature
BTD	brightness temperature difference
CALIOP	Cloud-Aerosol Lidar with Orthogonal Polarization
CALIPSO	Cloud-Aerosol Lidar and Infrared Pathfinder Satellite Observation
CAPE	convectively available potential every
Cb	cumulonimbus
CCL	convective condensation level
CIN	convective inhibition
CPR	Cloud Profiling Radar (CloudSat)
DCC	deep convective clouds
ECMWF	European Centre for Medium-range Weather Forecasts
EL	equilibrium level
FL	freezing level
FPH	frost point hygrometer
GPH	geopotential height
GSL	Great Slave Lake
HFL	homogeneous freezing level
HYSPLIT	Hybrid Single-Particle Lagrangian Integrated Trajectory model
IWC	ice water content
LCL	lifting condensation level
MDT	mountain daylight time
MLS	Microwave Limb Sounder
MODIS	MODerate Imaging Spectroradiometer
NARR	North American Regional Reanalysis
NASA	National Aeronautics and Space Agency
NOAA	National Oceanic and Atmospheric Administration
NRL	Naval Research Lab
PBL	planetary boundary layer
ppmv	parts per million (per unit volume)
ppbv	parts per billion (per unit volume)
PSD	particle size distribution
PVU	potential vorticity units
pyroCb	pyrocumulonimbus
pyroCu	pyrocumulus
TTL	tropical tropopause layer
UTC	coordinated universal time
UTLS	upper troposphere/lower stratosphere
VMR	(water) vapor mixing ratio

w.r.t.	with respect to
θ	potential temperature
r_e	effective radius

Chapter 1: Introduction

The tropopause is a well-defined boundary between the troposphere and the stratosphere in the midlatitudes. This boundary is delineated in several ways, but the traditional meteorological definition is the "cold-point" temperature in a vertical sounding, defined by the World Meteorological Organization as the lowest altitude at which the lapse rate (Γ) becomes consistently $\Gamma \leq 2$ °C km^{-1} for a vertical depth of 2 km (*World Meteorological Organization*, 1992). The air above and below the tropopause is warmer than the boundary itself, producing a very stable region that acts to inhibit transport across it. This phenomenon is easily observed when an intense cumulonimbus (Cb) grows in height to a level of neutral buoyancy, also called an equilibrium level (EL), where the temperature of a saturated convective parcel equilibrates with the environmental temperature. Upon reaching an EL, a majority of the convective column is no longer buoyant, and clouds spread out to form a cirrus anvil. The tropopause represents one such boundary. Particularly intense updrafts in Cb can penetrate through this level and form an overshooting top, and these relatively rare events are a direct intrusion of tropospheric air and cloud matter into the lower stratosphere (LS).

On the other hand, in the tropical latitudes the tropopause interface is now

thought of as a transitional layer instead of a hard boundary (*Fueglistaler et al.*, 2009). Traditional parcel theory still adequately explains convective events in this region, but transport through the tropical tropopause layer (TTL) is thought to be more common than troposphere/stratosphere exchange in the midlatitudes because convection can be more sustained and intense. However, there is uncertainty in the dominant mechanisms of cross-boundary processes in both the tropics and midlatitudes.

Even in the tropics where the boundary is less well-defined, the isentropic surface (constant potential temperature) θ = 380 K is considered a highly stable "overworld" that receives minimal direct influence on short time scales from the troposphere (*Holton et al.*, 1995). The TTL and sources of transport through it have been (and are continuing to be) studied intensely as climate science increasingly acknowledges the large role the stratosphere has on surface and tropopause energy budgets, but aside from volcanic events, comparatively little attention has been given to midlatitude phenomenon that can directly influence the stratosphere (*Fromm et al.*, 2010).

Over the past two decades, there has been increasing recognition that pyrocumulonimbus (pyroCb) events are a common occurrence in the midlatitude summer, and they routinely penetrate the tropopause with a plume comprised of ice, smoke and biomass burning gases (*Fromm and Servranckx*, 2003; *Fromm et al.*, 2005, 2008a). The stratospheric aerosol impact of these events may be important on annual time scales when considering several events occur throughout a fire season, but singular pyroCb events can have major direct injections on the scale of

volcanoes (*Peterson et al.*, 2018). In addition to the effects on the stratospheric aerosol burden, recent work has shown that direct injection of ice during pyroCbs may play a role in determining down-stream water vapor mixing ratio (WVMR) in the stable layers of the LS (*Kablick et al.*, 2018).

The overall impact that these events have on climate via direct stratospheric injection is unknown, but may be important. The irregularity of major volcanic eruptions leads to an *ex post facto* determination of their overall importance on stratospheric processes, but pyroCbs are now recognized as a continuing seasonal occurrence with a basic understanding of the conditions necessary to generate them (*Peterson et al.*, 2017a,b). Therefore, it is worth studying this phenomenon in the context of climate as they may be prognosticable in the future.

In order to do such a climate study, the nature of pyroCb dynamics first needs to be established through convective structure, microphysics and detrainment properties, in addition to the individual radiative effects water vapor and aerosol have once injected into the stratosphere. This study starts this work. The rest of this chapter provides motivation with background information, and then details the objectives.

1.1 UTLS Water Vapor and Climate

Long-term WVMR records from different measurement sources disagree in both the magnitude and the sign of any trend that may exist in the upper troposphere and lower stratosphere (UTLS). For instance, *Hurst et al.* (2011) analyzed

a 30-year record from balloon-borne frost point hygrometer (FPH) measurements at the National Oceanic and Atmospheric Administration (NOAA) site in Boulder, Colorado, and concluded that there has been a $+1.0 \pm 0.2$ ppmv ($27 \pm 6\%$) increase since the start of the measurement period. Whereas *Hegglin et al.* (2014) constructed a merged satellite record using bias-corrected data from several space-borne instruments and a chemistry-climate model, and concluded both that the LS has experienced a negative WVMR trend of -0.27 ± 0.18 ppmv (2σ uncertainty) and that the Boulder balloon record is not representative of the global trend.

Lossow et al. (2018) presented an updated analysis on the Boulder dataset, and showed an altitude-dependent trend ranging between +0.1 and +0.45 ppmv decade^{-1}, but this result once again does not agree with zonally-averaged trends at the same latitude from the merged satellite data during the same time period. However prior to these studies, a different methodology was used by (*Solomon et al.*, 2010) to construct a merged data set with the same satellite retrievals, and found an increase in WVMR over this time period, but with strong decadal-scale oscillations. The causes of these decadal oscillations, as well as the trends and the discrepancies between averaging a continental point-measurement at Boulder and satellite zonal averages remain a source of debate. What remains clear, however, is the importance of lower stratospheric water on climate.

In their study, *Solomon et al.* (2010) explained that the semi-decadal decline in stratospheric WVMR reported between 2001–2005 was significant enough to mitigate the rate of surface warming from greenhouse gases by $\sim 25\%$. That result is based on full spectrum line-by-line radiative forcing calculations using the com-

bined balloon and satellite observations. However, there is disagreement over the magnitude of tropopause-level radiative forcing (RF) caused by stratospheric water vapor anomalies. Estimates of the adjusted climate response depend on the source of data and the type of radiative transfer model (RTM) used. Current estimates of RF range from +0.24 W m^{-2} for a $\sim$ 1 ppmv increase above the tropopause from 1980 to 2000 (*Solomon et al.*, 2010) to +0.12 W m^{-2} for a $\sim$ 0.7 ppmv increase from 1979 to 1997 (*Oinas et al.*, 2001). For comparison, the RF of anthropogenic CO_2 increases since 1750 is $+1.66 \pm 0.17$ W m^{-2} (*Forster et al.*, 2007), and the total contribution of H_2O to the overall clear sky energy budget is $\sim$ 71 W m^{-2} (*Kiehl and Trenberth*, 1997). Despite the difference in the magnitude of the estimates, and without considering the secondary effects on stratospheric chemistry, there is generally a good understanding that an increase in H_2O above the tropopause will cause warming in the troposphere and cooling in the stratosphere given the potency of the H_2O absorption spectrum.

Water vapor climate forcing can be shown from an instantaneous perspective (i.e., ignoring feedbacks and chemistry changes) using a model atmosphere with perturbed WVMR profiles, and computing RF. One-dimensional radiative forcing is defined in terms of the upward and downward flux ($F^{\uparrow}$ and $F^{\downarrow}$, respectively) as the inverse of the change in net flux (F^{net}) from a control state:

$$RF = -\Delta F^{net}, \tag{1.1}$$

where

$$\Delta F^{net} = (F^{\uparrow} - F^{\downarrow})_{anomaly} - (F^{\uparrow} - F^{\downarrow})_{control}. \tag{1.2}$$

Figure 1.1 shows the forcing experienced by imposing a ±1 ppmv water vapor anomaly on the Air Force Geophysical Laboratory (AFGL) standard midlatitude atmosphere ("control"). This figure shows the WVMR change in terms of an absolute amount (a) and a vertically-resolved percentage (b). Note that the percent change in Figure 1.1b is only shown for an increase. Temperature (a) and air density profiles (b) are held constant, and a 1-dimensional longwave (wavenumber $\tilde{\nu}$ between 10–3000 cm^{-1}) band model is used to compute the radiative flux and cooling rate for both the unperturbed and the perturbed WVMR profiles, which are applied uniformly throughout the total depth of the atmosphere.

This figure shows that increasing WVMR in the upper troposphere and lower stratosphere increases $\mathrm{F}^{\downarrow}$ at the tropopause while silghtly decreasing $\mathrm{F}^{\uparrow}$ (blue and red dashed lines in Figure 1.1d, respectively). The combined effect of this is to create a positive longwave RF. Note the black dashed line is $\Delta\mathrm{F}^{\mathrm{net}}$, so that negative values in the profile represent positive RF. The cooling rate is the flux divergence in a layer, so negative values of cooling rates—and in this case cooling rate differences—indicate warming with respect to the control atmosphere.

This simple example illustrates the importance of understanding short- and long-term changes in LS $\mathrm{H_2O}$ because this increase produces an instantaneous tropopause $RF > 0$. $\mathrm{H_2O}$ is also very important in stratospheric ozone budgets, and water vapor feedback has been estimated to be 0.3 W m^{-2} for a +1 °C temperature anomaly in the mid-troposphere (*Dessler et al.*, 2013), so the issue extends beyond direct radiative forcing.

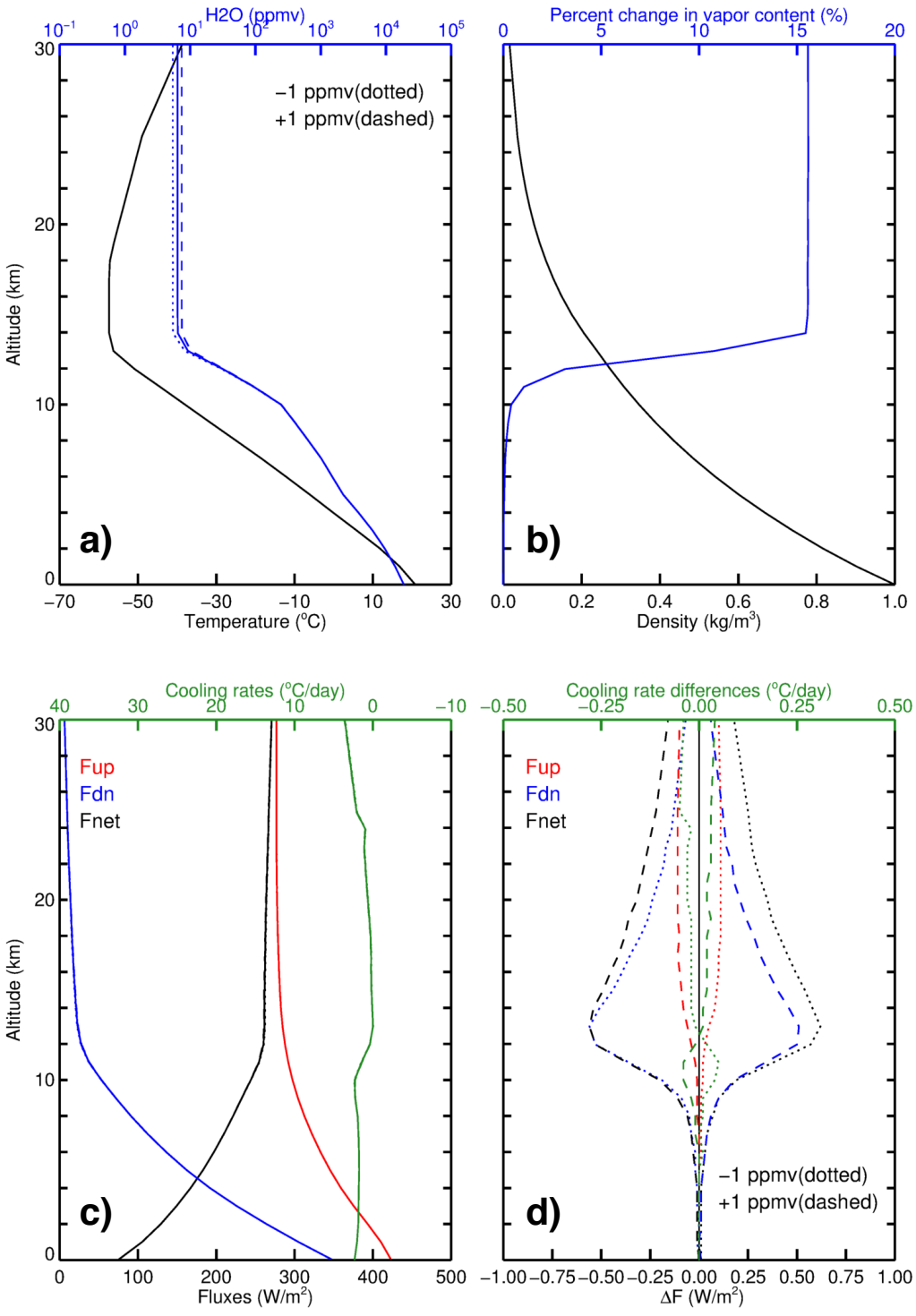

Figure 1.1: Perturbations and radiative transfer through AFGL midlatitude atmosphere. (Continued on following page)

Figure 1.1: (continued) Model profiles in each panel show (a) temperature (black) and H_2O (blue), where the solid line is the standard mixing ratio and dashed/dotted lines are the +1 or −1 ppmv perturbations; (b) air density (black) and the percentage WVMR perturbation (blue); and (c) longwave fluxes (upward; red, downward; blue, net; black) and cooling rates (green). The eight lines in (d) are the flux and cooling rate differences between the +1 or −1 ppmv perturbations on the standard model results shown in (c).

1.2 Tropopause-Involved UTLS H_2O Trends

An interesting approach taken by *Hurst et al.* (2011) was to statistically separate the midlatitude stratospheric water vapor observations series into distinct epochs based on statistical growth/decay trends. Doing this, they found significant growth in the trends of three out of four total epochs, with a significant decline in one epoch and an strong altitude gradient among the trends for all epochs (see their Figure 1). For the earliest epoch (1980–1990), they showed stronger trends near the tropopause—an indication that the majority of the increase was from tropospheric sources. The third epoch of their analysis, corresponding to the 2001–2005 decline noted by *Solomon et al.* (2010), was the only period with a negative trend at all altitudes.

The *Hurst et al.* (2011) study also presented average monthly profiles that showed an obvious increase in mixing ratio above 19 km, which they attributed

to photochemical production involving methane (see their Figure 3). The seasonal variation of the midlatitudes was also apparent below this altitude, with larger mixing ratios in the boreal summer months. This seasonal variability could be caused by two possibilities: 1) during boreal summer, there can be an increase in moisture transport from the tropical tropopause layer (TTL) from stronger isentropic mixing across the tropopause boundary with the weakening of the Hadley circulation and the sub-tropical jet (*Fueglistaler et al.*, 2009), or 2) there is an increase in overshooting convection in the midlatitudes, contributing to larger mixing ratios from detrained convective parcels.

That conclusion is based on the current understanding that the only significant sources of stratospheric H_2O are photochemical methane oxidation in the upper stratosphere (*Bates and Nicolet*, 1950) and meridional transport of comparatively moisture-rich air that has been lifted through the tropical tropopause (*Kley et al.*, 2000). However, if all stratospheric methane is oxidized (creating approximately two H_2O molecules per molecule of CH_4), it would still not create enough water to explain the observed increase over their 30-year Boulder balloon record.

It is possible that the dominant source of LS H_2O could be upwelling through the TTL. Tropical influences on midlatitude fluctuations in LS moisture are thought to be controlled by transient moisture uplift through the TTL where the WVMR of lifted air masses is subject to the ambient temperature of the surrounding air, and then those air masses are subsequently transported poleward (*Sherwood and Dessler*, 2001; *Fueglistaler et al.*, 2009; *Wang and Dessler*, 2012). In the tropics—the upward branch of the Hadley Circulation—integration of these transient events

results in a positive moisture flux into the stratosphere from below. The amount of water vapor that eventually crosses this vertical boundary is thought to be a function of the coldest temperature the air mass encounters as it is lofted. Thermodynamic considerations dictate that as a parcel is cooled, the saturation vapor pressure decreases and the vapor in the parcel is lowered to equilibrium by condensation to the ice phase (*Pruppacher and Klett*, 1997), Thus, the coldest temperature the parcel experiences would determine its water vapor mixing ratio upon entry into the LS. Typically this coldest temperature occurs at the tropopause, and colder temperatures inhibit moisture flux by "freeze drying" the air as it transported (*Jensen et al.*, 2001). The implied possibility in (*Hurst et al.*, 2011) is that this source of midlatitude LS H_2O may be increasing.

However, it is also possible—and even likely—that the FPH instruments used in the Boulder record have experienced inconsistencies in both manufacturing and calibration over the 30-year duration used in the study, and that these inconsistencies could be artificially causing a positive WVMR trend over this time period. This possibility is bolstered by the fact that the Boulder balloon record disagrees with various merged satellite records (*Hegglin et al.*, 2014). However, the vertical differences in rates of WVMR increase may have a physical source.

The cold-point temperature in the TTL is known to have a strong seasonal fluctuation, so there is a natural cycle to the moisture flux across the tropical tropopause. In fact, most of the LS H_2O trends discussed in *Hegglin et al.* (2014) are shown with the chemistry-climate model to be a result tropopause temperature fluctuations. The annual mean temperature at the tropical tropopause is $\sim$ 195 K

with a ~ 8 K peak-to-peak annual fluctuation (*Fueglistaler et al.*, 2009). The coldest temperatures occur during boreal winter and the warmest temperatures during boreal summer.

The dominant cause of these temperature fluctuations is thought to be a result of the seasonal migration of the Intertropical Convergence Zone (ITCZ), which increases (decreases) the radiative cooling as the latitude of maximum convection moves closer to (farther away from) the equator during the boreal winter (summer). Also, other cycles such as the El-Niño Southern Oscillation (ENSO) and the quasi-biennial oscillation (QBO) in the stratosphere affect the interannual variability of tropopause temperature (*Ramaswamy et al.*, 2001). In summary, there are strong natural cycles that can contribute to UTLS moisture fluctuations on shorter time scales. One lesser-explored aspect, however, is how ice microphysics may play a role, and to what extent any changes to this role would be natural. The main source of ice in the UTLS is deep convection, so could changing deep convection frequency or ice cloud properties influence LS H_2O?

1.2.1 Deep Convection and Ice Microphysics

A major conclusion of the *Hurst et al.* (2011) study was that the combination of methane-produced H_2O in the upper stratosphere and tropical changes do not adequately explain the vertical gradients of moisture growth or their magnitudes during the four epochs between 1980 and 2010. Intuitively, there would be a need for at least one other important mechanism that increases midlatitude stratospheric

water vapor with stronger contributions at higher altitudes, assuming the positive trends in the Boulder balloon record are not instrument/retrieval-related. Those authors postulate that a combination of dynamical and thermodynamical factors are involved, which would contribute to changes in both the creation and redistribution of H_2O.

Wang and Dessler (2012) showed the seasonality in LS moisture from 2005–2010 and the vertical phase shift in the UTLS mixing ratio at four isentropic levels as observed by the Microwave Limb Sounder (MLS) instrument on-board the Aura satellite (θ = 360, 370, 380 and 400 K corresponding to altitudes of approximately 15, 16, 17 and 18 km, respectively). That study confirmed previous conclusions from legacy H_2O-monitoring instruments that there is an upward propagation to higher altitudes, and it is not instantaneous; there is an $\sim$ 4 month phase delay in the peak value between the lowest level and the highest level 3 km above. This delay is referred to colloquially as the "atmospheric tape recorder" (*Mote et al.*, 1996).

In addition, *Wang and Dessler* (2012) also showed that there is a strong seasonal dependence on the maximum amount of LS WVMR independent of the tape recorder phenomenon, which is driven by the QBO's effect on tropopause temperature. They argued that the outlying events that produce maximum values (such as intense overshooting convection) are well-correlated with the seasonal-mean values. They suggested that this process indicates intense overshooting convection with its associated ice clouds and large WVMR does play a significant role in moistening the LS, at least in the tropics. However, for the sake of completeness it must be stated that tropical overshooting convection is relatively rare, and the major mech-

anism determining H_2O mixing ratios entering the stratosphere is still considered to be the traditional Brewer model of slow tropical tropospheric ascent driven by the meridional radiative budget imbalance (*Brewer*, 1949).

Therefore, the majority of stratospheric moisture budget studies are concerned with changes to UT mixing ratios, not overshooting convection. Depending on the ambient saturation vapor pressure at these levels where ice is detrained, there may be a net hydration or dehydration of these air masses due to the removal/survival processes of ice crystals (*Randel and Jensen*, 2013). It seems counterintuitive, but an upper tropospheric air layer already above saturation would cause detrained crystals to grow in size to a point at which they would fall out (gravitational settling), thus drying the air. The obverse is also true where subsaturated air would "remove" the crystals by sublimation *in situ*, thereby moistening the air. A recent long-term modeling- and observation-based study reaffirmed this process (*Schoeberl et al.*, 2018).

As *Sherwood* (2002a) suggested, anomalies in stratospheric moisture trends may be caused/augmented by changes to the microphysical properties of ice clouds by anomalous aerosol concentrations affecting convective properties. This effect would not be confined to the tropics because, for instance, aerosol-invigorated convection in the midlatitudes could result in more overshooting anvils. This would constitute an additional, independent source of moisture in the LS not subject either the supersaturation of UT air or the slow ascent across the tropical tropopause.

1.3 Pyrocumulonimbus

As the previous sections in this chapter have illustrated, there is ample motivation for understanding the processes involved with stratospheric penetration, and many of the known phenomenon that do so are the focus of many research projects. To that end, this project focuses on one that is under-studied: pyroCbs. These midlatitude events commonly inject plumes into the UTLS (*Damoah et al.*, 2006; *Fromm et al.*, 2010; *Peterson et al.*, 2017a). They typically form over large wildland fires in the mid- to high-latitudes on an annual basis, and produce a plume comprised of a mixture of biomass burning aerosols, gases, and cloud ice particles that otherwise would not be present in the UTLS in such abundance (*Fromm and Servranckx*, 2003).

Since their discovery, scientific understanding of these events has increased: a conceptual model has been put forth regarding the meteorological and burning conditions necessary for pyroCb development (*Peterson et al.*, 2017b); the droplet and ice particle size distributions (PSD) have been shown to possess a very small effective radius (*Rosenfeld et al.*, 2007); and the outflow anvils are known to have a distinct increase in lifetime compared with meteorological cumulonimbus forming in the same synoptic conditions (*Lindsey and Fromm*, 2008). However, there are still several aspects of the pyroCb phenomenon that require a better understanding, such as the internal dynamics of the updraft column, the relative importance of aerosol-cloud microphysical interactions, the stratospheric impact of injected smoke, ice, and water vapor.

Both observations and modeling studies of regular (non-pyro-) convection have shown that small ice particles result from larger quantities of cloud condensation nuclei (CCN) in the boundary layer (*Khain et al.*, 2005), and that anvil size is generally larger (*Fan et al.*, 2013; *Yan et al.*, 2014). In these situations CCN abundance reduces the average droplet size in the updraft columns, and a so-called "invigoration effect" may result (*Rosenfeld et al.*, 2008; *Li et al.*, 2011). A reduction in droplet size limits collisions and coalescence, thereby maintaining a greater amount of condensed water that will increase latent heating above the freezing level and enhance the buoyancy of rising air (*Rosenfeld and Woodley*, 2000; *Khain et al.*, 2005).

For pyroCb events, idealized model simulations have also shown that a large CCN concentration can significantly enhance latent heat release (*Reutter et al.*, 2014), but the role of this aerosol effect on updraft velocity was shown to be small when compared with buoyancy enhancements from extreme sensible heat fluxes over a fire (*Luderer et al.*, 2006). An additional consideration behind the large number density of small ice particles in convective clouds is the strength of the updraft itself. The supersaturations are larger in such conditions, leading to rapid generation of ice crystals above the freezing level (*Rosenfeld et al.*, 2007). Regardless of the dominant influence—whether it is a CCN effect on the PSD or the surface heat flux—it is certain that pyroconvection has intense updrafts and clouds with very small droplets and ice crystals.

A corollary to diminishing ice crystal size is that the inefficient removal of these particles has the potential to increase absolute humidity within an aging plume. Ice particles that comprise convective anvils undergo various removal processes as they

age, including sublimation and sedimentation. Sublimation occurs when conditions become sub-saturated with respect to ice as the anvil mixes with ambient air. In a study based on convective anvil penetration of the tropical tropopause, *Sherwood* (2002b) hypothesized that mixing drier air into ice-rich cirrus containing small particles would reduce the saturation ratio to the point that ice sublimation would increase downstream absolute humidity as compared with cirrus with larger particles.

In a previously-mentioned follow up paper, *Sherwood* (2002a) relied on geostationary satellites to infer there was a detectable anti-correlation between tropical UTLS absolute humidity and convective anvil ice particle size. In other words, smaller effective radii in convective cirrus near the tropical tropopause preceded an increase in water vapor concentrations at higher altitudes, to where tropical upper tropospheric air slowly migrates (*Fueglistaler et al.*, 2009). In addition to this gradual upward lifting, overshooting convection can directly deposit water into the LS as discussed in the previous section. Although locally significant, this mechanism is thought to be less important in the overall budget than the transient uplift of moisture in UT air (*Dessler*, 2002). The overall implication of these mechanisms is that the rate of moistening/drying in the TTL plays a direct role in determining the LS water vapor budget.

However, cross-tropopause transport in the mid-to-high-latitudes is comparatively rare, and is typically only a result of direct injection (*Holton et al.*, 1995; *Bedka*, 2011). Figure 1.2 illustrates the meteorological- and volcanic-source events known to impact the UTLS. Number 6 on the figure represents pyroCb that occur

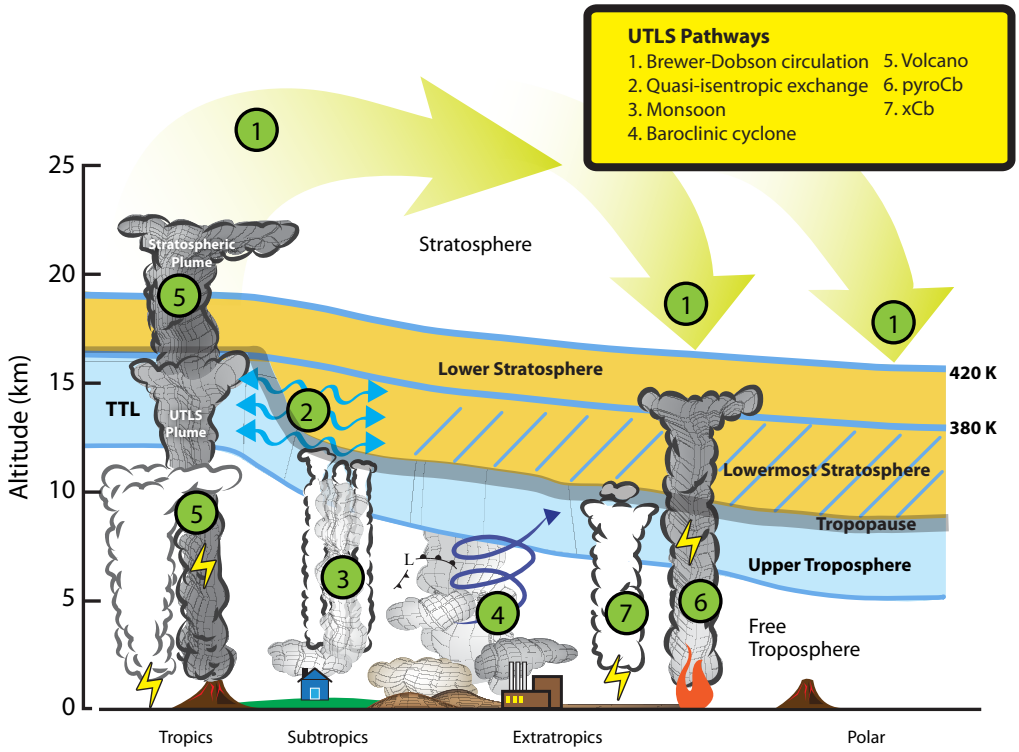

Figure 1.2: Tropospheric phenomenon known to interact with the UTLS.

poleward of the subtropics, where the tropopause is typically between 10-12 km a.m.s.l. As demonstrated in this figure, Cb have weak overall LS penetration, and the potential for direct injection of air masses into the stable regions above $\theta \simeq 380$ K is very small compared with pyroCb.

Another microphysical process to consider is sedimentation, which could reduce the impact a sublimating ice cloud would have on absolute humidity by removing a potential vapor source from the parcel. In this process ice precipitates to lower altitudes after the updrafts maintaining the suspended particles are weakened or as particles aggregate into sizes large enough to gravitationally overcome the updraft forces.

In their study on tropical convective anvils, *Jensen et al.* (2009) noted that

both the sublimation and growth rates of ice crystals are a function of the saturation ratio and a deposition coefficient (see their Figure 11). They used *in situ* aircraft observations during the Tropical Composition, Cloud, and Climate Coupling (TC4) campaign to argue that small ice crystals do not persist longer than a few hours; they either grow through deposition or they completely sublimate in subsaturated air; their results were consistent with previous work on other types of small-ice-crystal clouds such as wave clouds. In the case of a pyroCb, an anvil would need to have an ice saturation ratio very close to 1.0 in order for the crystals to neither sublimate nor grow too quickly to be removed by sedimentation. *Lindsey and Fromm* (2008) used infrared observations to show pyroCb anvils persisted between $\sim$ 18–30 hours longer than that of nearby meteorological Cb anvils post-detrainment, which would mean the saturation ratio must be favorable to ice for a longer period of time.

In addition to aerosols and ice, pyroCb are known to inject a large amount of combustion-generated gases into the stratosphere (*Pumphrey et al.*, 2011). One of these is water vapor, which has the distinct role of contributing to hydrometeor and latent heat processes throughout the depth of the convective cloud (*Potter*, 2005). Meteorological deep convection over North America and the Asian Monsoon is known to directly inject locally-substantial amounts of water vapor into the lower-most stratosphere, but the satellite-based studies have shown the net effect of those injections to be small (*Schwartz et al.*, 2013). PyroCb, however, are unusually intense and their cloud properties are distinct from Cb, so an important question is whether ice microphysics plays a role in the amount of water vapor injected into the LS during these events since changes to ice PSD may affect changes in sublimated

vapor down-stream. For this to be true, ice crystals would have to sublimate in the UTLS instead of being removed through sedimentation. The best way to address this question would be from *in situ* aircraft measurements through active and detrained pyroCb anvils. Unfortunately such an encounter has not been documented, so this study relies on remote sensing instruments and a cloud-resolving model.

Lastly, the net aerosol loading from pyroCb events is unknown, but is possibly a significant source of "background" UTLS aerosol optical depth. Stratospheric aerosol sources were once thought to be either volcanic in origin or chemically-produced locally with tropospheric sulfate precursors (*Brasseur and Solomon*, 1986). Smoke (black and brown carbon) are the main aerosol components of pyroCb plumes, and there is a strong need to understand the lifetime and evolution that these plumes experience once injected.

1.4 Objectives

The objectives of this study include the following:

1. Establish the convective lifecycle of a pyroCb with an emphasis on i) convective triggers, ii) aerosol influences on cloud microphysics, iii) meteorological conditions, and iv) stratospheric detrainment. Additional analysis is to compare pyroCb dynamics with regular convection. (Chapter 2)

2. Simulate pyroCb convective dynamics and detrained plume properties with an aerosol-cloud-resolving model, performing sensitivity tests on i) aerosol loading, ii) meteorological precursors and iii) fire-generated sensible heat flux. Es-

timate these individual contributions to stratospherically-injected total water content, including ice cloud mass and absolute humidity. (Chapter 3)

3. Develop a radiative transfer framework to simulate the stratospheric pyroCb aerosol plume morphology, and make an estimate of total mass injected for an extreme case. Validate the simulated results with observations. Examine additional cases from literature within the same radiative framework to test its robustness. (Chapter 4)

4. Set benchmarks for the water vapor component of pyroCb plume radiative forcing based on observed WVMR anomalies using a highly detailed absorption spectrum and a line-by-line radiative transfer model, and test the sensitivity of this forcing for two different climatologies used to compute the WVMR anomalies. (Chapter 5)

Chapter 2: PyroCb Events

The stratospheric effects of pyroCb injections may be better understood when analyzing the nature of the convective events themselves. Meteorological and fire-related dynamics contribute to both the initiation and the maintenance of convective growth, and it is possible the intensity of this relationship is directly related to the net stratospheric impact of the injected plumes. For example, recent studies have shown that pyroCb initiation can be triggered by either dynamical uplift from an approaching front (*Peterson et al.*, 2018) or by a sudden increase in fire energy output (*Kablick et al.*, 2018). Both of these types of triggers—although different mechanisms—are simply a perturbation to the atmospheric stability above the fire column.

This chapter provides an analytical overview of the meteorological conditions and the stratospheric impacts of two well-documented case studies, and augments this analysis with additional evidence from supplementary published cases. It focuses heavily on a pyroCb that formed south of Great Slave Lake (GSL) in the Northwest Territories of Canada in 2014, but introduces an additional pyroconvection case from the Pacific Northwest in 2017 used in later chapters.

The former pyroCb (hereafter "GSL pyroCb") is detailed herein because it

had very good observational coverage from both satellites and ground sites. Data collected from both these sources are substantial enough to provide detailed insight into its convective lifecycle, and allow for comparisons with regular (non-pyro) Cbs. Additionally, an aerosol- and cloud-resolving convective model is used to parse the important differences between surface heat fluxes and latent heating effects of extreme aerosol concentrations on the convection and subsequent plume properties, including the effect on detrained stratospheric water vapor.

The latter pyroCb, or rather pyroCb cluster (hereafter Pacific Northwest Event "PNE") created the largest-ever observed stratospheric pyroCb plume. It was observable using several satellite instruments for at least five months post-UTLS injection. It is introduced in this chapter, but the bulk of analysis on the PNE case is contained in Chapters 4 and 5.

2.1 Case Studies

2.1.1 Great Slave Lake 2014

The GSL pyroCb began at approximately 18:45 UTC on 5 August 2014 over fire 14WB-025 (number designation used by Parks Canada/Wood Buffalo National Park; 60.2°N, 115.5°W). The fire had been burning for approximately six days after a lightning strike on 30 July. There were many fires burning in and around the Wood Buffalo National Forest and GSL regions at the time, some of which had already produced pyroCbs prior to 5 August, but the GSL pyroCb had fortuitous satellite coverage in addition to several ground stations recording observations nearby during

the active stages of convection. Additionally, the detrained plume was observable by instruments in NASA's A-Train (*Stephens et al.*, 2002; *Winker et al.*, 2009) for over two weeks after the event. As such it provides a useful case for an examination of a complete pyroCb lifecycle, including any water vapor impact of UTLS-injected ice.

Over the course of three hours on 5 August multiple polar orbiting satellites captured the growth and development of the GSL pyroCb prior to, during, and after the active stages of convection. Figure 2.1 shows True-Color images by the MODerate Imaging Spectroradiometer (MODIS) from both the Aqua (a, e) and Terra (b, d) platforms and similar images by the Visible Imaging Infrared Radiometer Suite (VIIRS) on-board Suomi NPP (c, f). A combination of the high northern latitude summertime conditions and the unusually early local time for pyroconvection (12:45 MDT) allowed each of the these imagers to capture multiple daytime passes.

Figure 2.1a-f show the GSL fire near the center of the images, and document the pyroCb from the early stages of cumulus congestus (a–c) through the mature convective column (d, e) and the detraining anvil stage (f). At approximately 20:20 UTC (14:20 MDT), Aqua MODIS made its second daytime pass (e), which occurred directly over the pyroCb column. The red line in Figure 2.1e shows the nadir ground track of the active A-Train instruments discussed later in this section: the CloudSat Profiling Radar (CPR, *Stephens et al.*, 2002) and the Cloud-Aerosol Lidar with Orthogonal Polarization (CALIOP, *Winker et al.*, 2009). Apparent brightness of smoke and haze between each image are due to the increase/decrease in sunlight scattering into the sensor as the viewing angle changes.

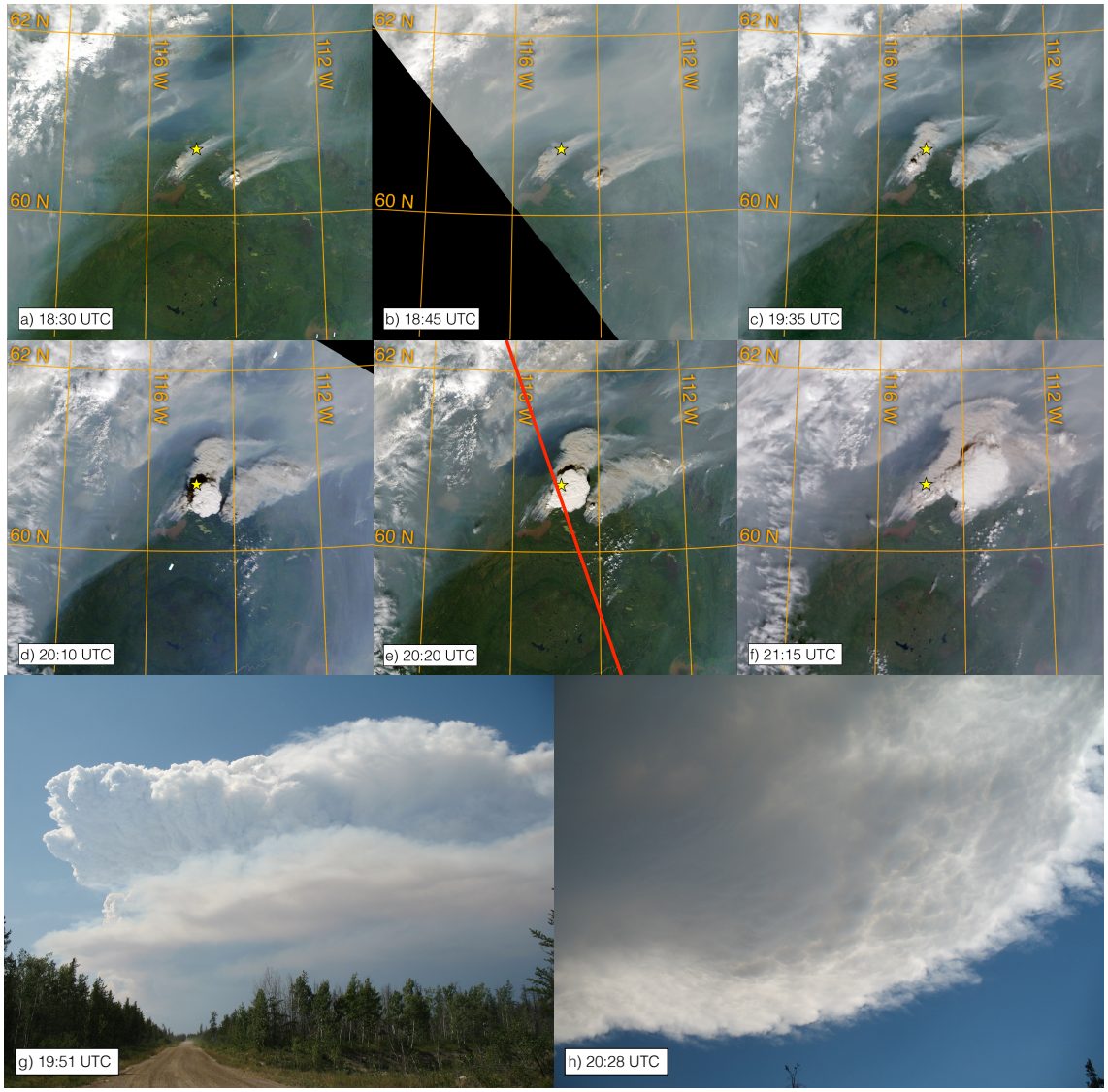

Figure 2.1: Visible imagery of the GSL pyroCb over the course of three hours on 5 August as seen by Aqua MODIS (a, e), Terra MODIS (b, d) and NPP VIIRS (c, f). Yellow star is location of the Buffalo Junction surface site, across which the active pyroCb moved. Red line in (e) is track of CALIOP and CloudSat (see Figure 2.6). Photographs in (g–h) taken by Mike Smith of Yukon Wildland Fire Management, and are used with permission.

Figure 2.1g-h are photographs taken by Mike Smith of Yukon Wildland Fire Management of the pyroCb approximately one-half hour apart during the "mature" stage of active pyroconvection (location where these photographs were taken is denoted as red circle on Figure 2.8 near Sandy Lake Road). Note the appearance of mammatus like clouds in Figure 2.1h when the anvil had moved overhead of the photographer's location.

In the days leading up to the GSL pyroCb, there was a large amount of smoke being generated in the region, and it prevented many of the perimeter flights used to accurately estimate daily fire progression [*personal communication with Northwest Territory Fire Resource personnel*]. However, perimeter data derived from MODIS Level 2 hot-spots indicate the fire consumed about 65400 ha in total during the six day period between ignition and the pyroCb event. The fire just to the east of center in Figure 2.1 at $\sim 114°$W (fire 14WB-028; hereafter "Eastern Fire") also produced a pyroCb. Cumulus congestus is also seen forming and dissipating over the Eastern Fire throughout the six snapshots in Figure 2.1, but it does not develop a pyroCb until after the anvil from the GSL pyroCb passes nearby, at which time it became apparent in geostationary imagery (discussed further in Section 2.2.2).

The intense convection from the Eastern Fire did not produce a mature a pyroCb until approximately 22:30 UTC, two hours after the GSL Fire. It is likely that the anvil from the Eastern Fire pyroCb interacted with the GSL pyroCb anvil blowoff to produce a larger UTLS plume than would have existed otherwise as indicated by the two-tiered appearance of the early morning visible-band "day after" plume at 11:30 UTC on 6 August (see Supporting Information Movie S2 in *Kablick*

et al. (2018)).

It is unknown why the two pyroCbs, both within the same region favorable to convection (discussed in Section 2.2.1), developed over two hours apart. Any number of factors such as fuel types and microscale meteorology could play a role in different rates of development for two pyroCb in the same region, but an in depth examination of the sensitivity to these variables is beyond the scope of this work. However, Section 2.2.1 analyzes the meteorological state and discusses the possible triggers for convection. Chapter 3 uses this information as initial conditions in several model simulations to show the surface heat flux is likely the most important factor in determining pyroCb generation.

2.1.2 Pacific Northwest Event 2017

Up until 12 August 2017, it was widely acknowledged by experts in the field that the largest pyroCb event (in terms of a stratospheric plume) was the "Black Saturday" event from 8 February 2009 in Victoria, Australia (*Siddaway and Petelina*, 2011; *Pumphrey et al.*, 2011). That event has been—and continues to be—widely studied both for the surface fire and weather conditions (*Dowdy et al.*, 2017) and the long-lasting UTLS impact (*Field et al.*, 2016). Then in the summer of 2017, four separate clusters of fires burning in the Pacific Northwest generated five total pyroCbs within the span of 5 hours on the afternoon of 12 August and generated the largest ever observed pyroCb plume (*Peterson et al.*, 2018). The fires were burning along the Cascades in Washington State and on the eastern side of the Coast

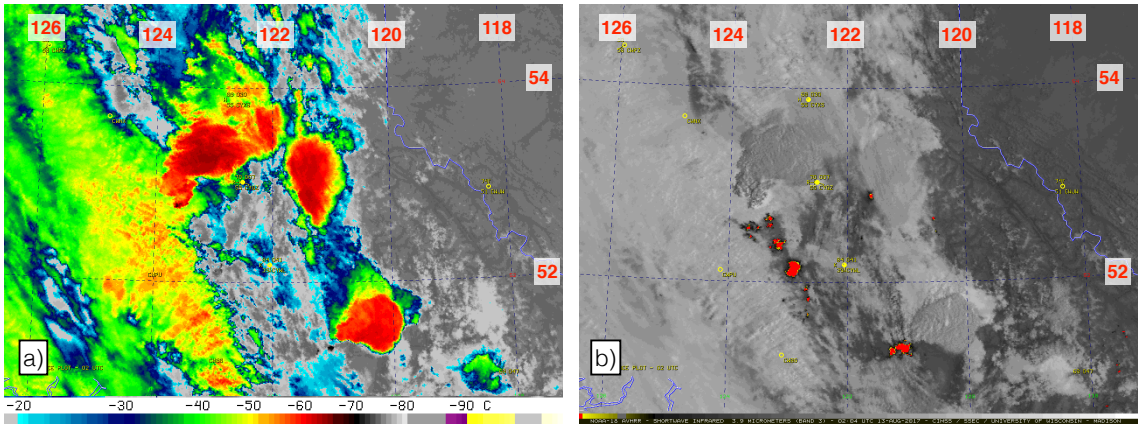

Figure 2.2: The PNE pyroCb event at approximately 20:00 local time on 12 August 2017 as viewed by AVHRR. (a) BT_{11} and (b) BT_3 showing the typical pyroCb signature cold cloud tops in the thermal channel and warm cloud tops in the near infrared (discussed in Section 2.2. Shown here are four pyroCb anvils originating from three fires discussed in the text. Fire locations are displayed as red pixels in (b). Images created by Scott Bachmeier and released to public domain (CIMSS pyroCb blog).

Mountain range in western British Columbia in advance of a frontal low pressure system moving in from the Pacific Ocean. Each pyroCb was active and intense for several hours, and the plumes of these fires were entrained into a synoptic jet that advected them to the northern coast of Canada over the next two days.

Figure 2.2 shows images from the polar-orbiting Advanced Very High Resolution Radiometer (AVHRR) of the mature stage of this pyroconvection swarm. The left panel (a) shows the thermal infrared brightness temperature at 10.8 μm (BT_{11}), and panel (b) shows 3.9 μm (BT_3). Red dots in panel (b) are the fire hot spots.

This convection occurred in an area that was very favorable to uplift with a very hot, dry and windy surface and an elevated moisture layer between 600–700 hPa associated with the advancing cold front.

Figure 2.3a–c shows VIIRS visible imagery over 11–13 August with fire hot spots overlaid as red dots. Panel (c) clearly shows the frontal clouds draped from southeast to northwest with a heavy concentration of smoke towards the top of the image. Rows (d–f) show the progression of the plume in terms of its Ultra-Violet Aerosol Index (UVAI) from the Ozone Mapping and Profiler Suite (OMPS) on-board Suomi NPP. The UVAI is a two channel algorithm that qualitatively detects both the concentration and altitude of absorbing aerosol plumes. Larger values correspond to both higher-altitude- and densely-concentrated-plumes, and this event generated values as large as 55 (unitless).

The progression over 12–16 August appears to show that the individual pyroCb plumes became "concentrated" as they moved around an Omega-block-patterned high pressure system that was situated over Alberta and Saskatchewan. Chapter 4 discusses of the early days of this plume concentration and possible consequences for its UTLS evolution. It also provides more information on the UVAI metric and its use in determining aerosol concentration. Chapter 5 examines this plume from a water vapor perspective, and estimates the UTLS H_2O component to radiative forcing.

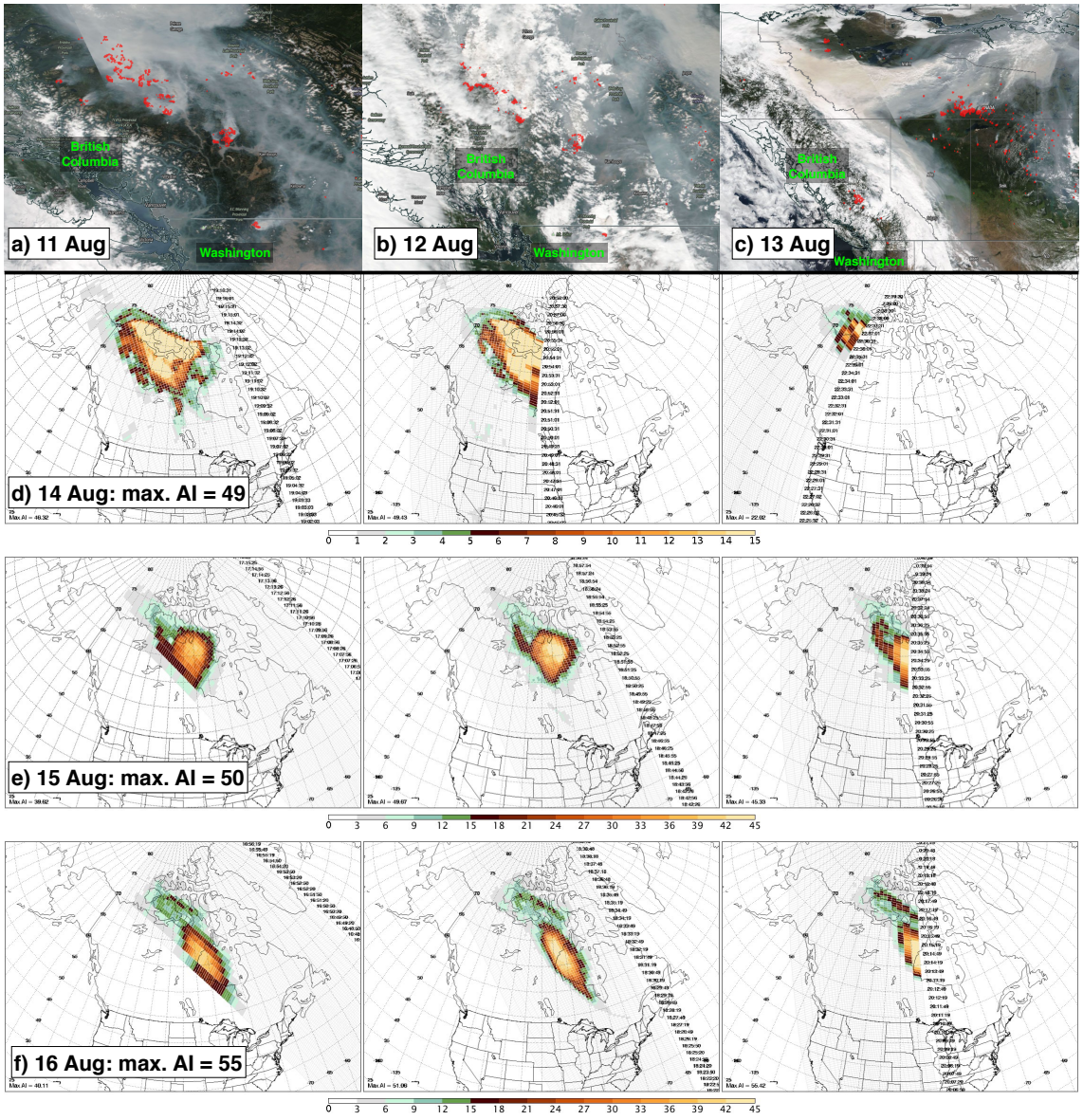

Figure 2.3: (a–c) VIIRS images of the Pacific Northwest during the three days centered on the PNE (red dots are fire locations). Rows (d–f) are OMPS UVAI images on the days that the plume moved northwestward around a high pressure Omega-block pattern, "gathered" in northern Canada, and subsequently moved southeastward. OMPS images created by Colin Seftor and used with permission.

2.2 Properties of Active PyroCb

This section utilizes the GSL pyroCb case to examine the similarities and differences between pyroCb and meteorological Cb cloud properties. Figure 2.4 contains VIIRS BT_3 during the times corresponding to Figure 2.1c,f. The images are constructed so the fire location hot spots identified by this channel are displayed as red-orange-yellow colors with the GSL Fire denoted by the yellow arrow, and the cooler BT_3 values corresponding to terrestrial and cloud temperatures are in gray-scale.

One common feature observed with pyroCbs in this part of the BT spectrum is a "warm" anvil (*Lindsey and Fromm*, 2008; *Fromm et al.*, 2010). *Lindsey et al.* (2006) explained there is a strong inverse relationship between daytime BT_3 and ice particle size for diameters <80 μm at a constant solar zenith angle since the solar reflectance component increases dramatically with decreasing effective radius (r_e). In the terrestrial-only infrared part of the spectrum (e.g., channels such as 11 and 12 μm), there is an insignificant contribution from solar reflectance, and for optically thick clouds at a given emitting temperature there is little difference in behavior of these BTs with particle size. The largest influence in these channels is the temperature of the cloud itself. A visual comparison of the pyroCb anvil BT_3 in Figure 2.4b (yellow circle) to that of the cirrus clouds in the upper left corner of the images highlight the effect of particle size. Similar effects between the thermal- and the near-IR BT channels are seen for the PNE case in Figure 2.2.

However, the optical thickness of a cloud needs to be accounted for when

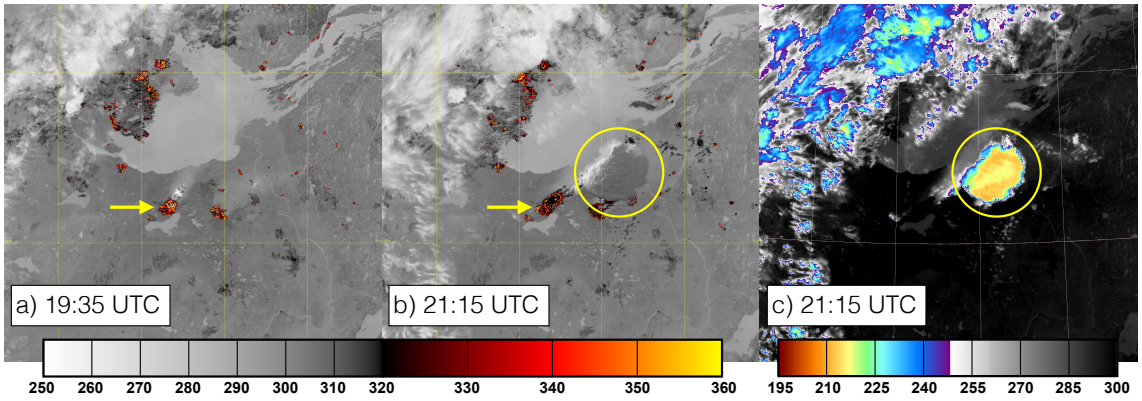

Figure 2.4: As in Figure 2.1c and 2.1f, but for VIIRS 3.7 μm (a, b) and 10.8 μm (c) BT of the GSL pyroCb. All values are in K. Images (b) and (c) are $\sim$ 100 minutes after a) on 5 August. Fire 14WB-025 is denoted with yellow arrow in (a) and (b). Note the darker color of the pyroCb anvil (yellow circle) in (b) as compared with the lighter cirrus clouds to the northwest (upper left of images) as the convection becomes detached from the fire, indicating an extremely small and narrow ice particle size distribution.

assuming daytime BT_3 "warmness" indicates a small r_e. Brightness temperatures from pixels containing semi-transparent clouds, for example, can have a significant contribution of radiance from emission below the cloud layer, making them appear warmer than opaque clouds at the same altitude. Figure 2.5a shows the BT_{11} from Aqua MODIS at 20:20 UTC (corresponding with Figure 2.1c). Minimum BT_{11} for the pyroCb top is -62 °C, and the anvil has a distinct "cold-U" feature typical of intense, overshooting thunderstorms (*Setvák et al.*, 2010).

One commonly used cloud optical opacity test is the brightness temperature

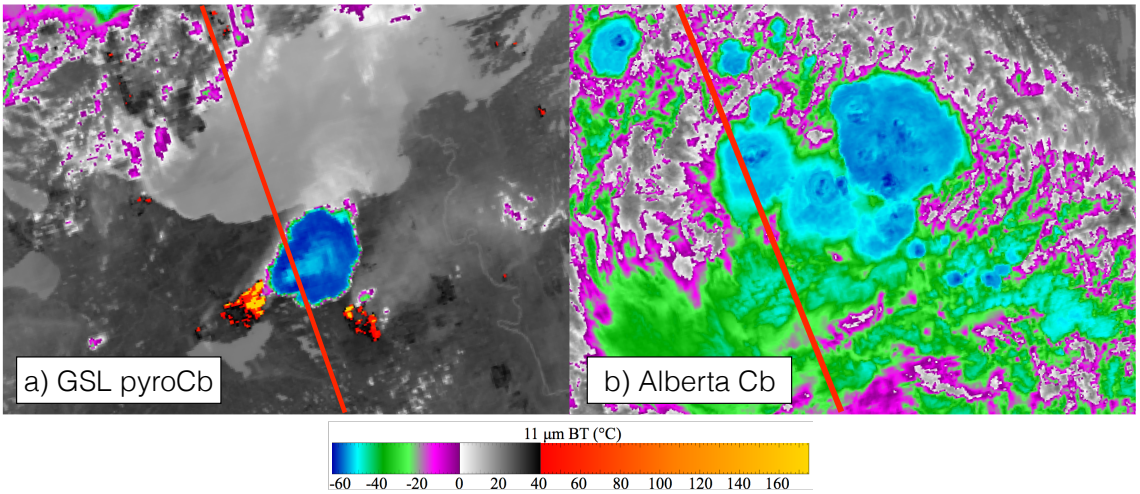

Figure 2.5: Aqua MODIS BT_{11} of the GSL pyroCb (a) and the concurrent Alberta Cb to the south (b) at 20:20 UTC. The red lines show the nadir ground track of CALIOP and CloudSat. Note the "cold-U" shape of the pyroCb outflow anvil with warmer temperatures corresponding to the central overshooting top. The Cb shows no such structure even though the minimum brightness temperatures are similar: −62 °C and −64 °C for pyroCb and Cb, respectively.

difference between two thermal infrared channels in the atmospheric window, in this case MODIS channels 32 (12 μm) and 31 (11 μm), denoted herein as BTD_{12-11}. Small absolute values ($|BTD_{12-11}| < 3.0$ °C) indicate optically thick clouds. This test was validated by *Peterson et al.* (2017a) for use with pyroCb anvils, and the result of that test on the GSL pyroCb anvil yields a BTD_{12-11} spread between −0.1 to +1.0 °C; well within the "optically thick" range. This result gives confidence that the warm daytime BT_3 values indicate an abundance of very small ice particles in the anvil.

A few minutes earlier during the same daytime Aqua MODIS pass, the A-Train observed a concurrent meteorological Cb in central Alberta (Figure 2.5b; hereafter "Alberta Cb") centered at 53.5°N. The Alberta Cb underwent convective development at approximately the same time ($\sim$ 18:45 UTC) as the GSL pyroCb as seen in GOES-West (GOES-15) imagery, and had a minimum $BT_{11} = -64$ °C with $|BTD_{12-11}| < 1.0$ °C, and a more uniform appearance to the BT field (no "cold-U"). CloudSat and CALIOP also passed directly over a deep convective portion of the Alberta Cb, as shown by a red line.

Figure 2.6 contains the "curtains" through both the GSL pyroCb and the Alberta Cb from these sensors. Level 1 CALIOP 532 nm total attenuated backscatter (β'_{532}) is shown above the corresponding CloudSat CPR 94 GHz radar reflectivity from the 2B-GEOPROF product, and overlaid on the images is a dashed line that represents the uppermost cloud observation by CALIOP for each case. The lidar detects the pyroCb overshooting cloud top altitude to be approximately 14 km a.m.s.l., whereas the radar does not observe this overshoot. It has a maximum cloud height detection of 13 km (Figure 2.6a, c). CALIOP observes large β'_{532} and full attenuation within a very narrow vertical depth (< 1 km), whereas the CPR has radar reflectivities beneath the noise threshold of -28 dBZ_e at these uppermost cloud top levels.

This discrepancy is not present with the Cb case, where both instruments detect a cloud near 12 km (Figure 2.6b, d). The sensitivities of these instruments to ice particle size have been documented in many places (*Miller and Stephens*, 2001; *Stephens et al.*, 2002; *Austin et al.*, 2009; *Delanoë and Hogan*, 2010) and is thought

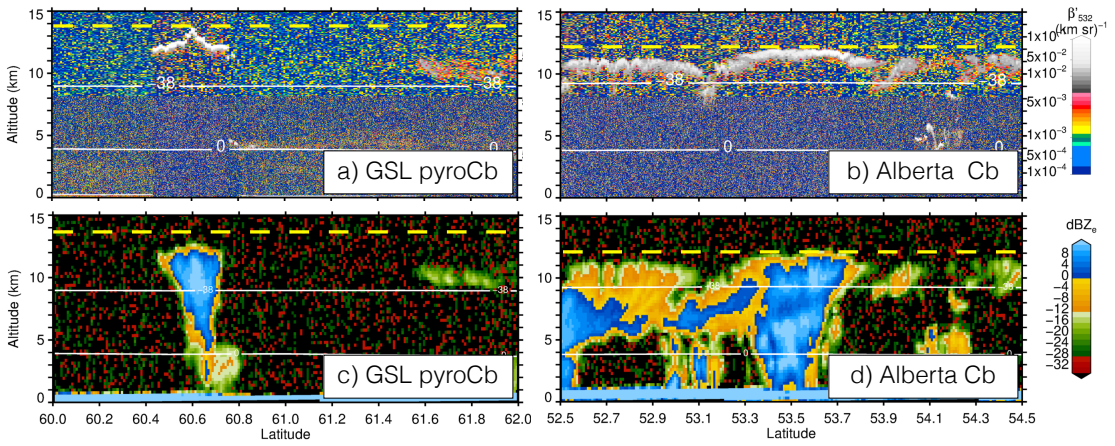

Figure 2.6: CALIOP 532 nm backscatter (top row) and CloudSat 94 GHz radar reflectivity (bottom row) at the 20:20 UTC intersection of the active GSL pyroCb (a,c) and Alberta Cb (b,d) cores (see red line in Figure 2.1e, 2.5a for pyroCb and Figure 2.5b for Cb). CALIOP shows that the GSL pyroCb has a highly attenuating anvil cloud with overshooting top near 14 km (a), and CloudSat indicates strong echoes in the mid-levels, but weak echoes near the surface, and no echoes between 13–14 km (c). The yellow dashed line indicates the CALIOP cloud top in both panels. Conversely for the Alberta Cb, CALIOP (b) and CloudSat (d) have similar cloud top heights, and the radar reflectivity shows a complex vertical structure of with large reflectivity near the cloud top and extending down to the surface. Also shown are the 0 °C and −38 °C isotherms from ERA-I reanalysis at both locations.

to be the cause of the cloud top discrepancy in the GSL pyroCb. The mid-visible CALIOP is most sensitive to the second moment of a PSD—proportional to the total cross-sectional area of all particles contributing to scattering—whereas the W-Band CPR is most sensitive to the sixth moment—proportional to the total volume

of scatterers. Therefore the GSL pyroCb anvil must be comprised of a large number of very small scatterers as compared with the Alberta Cb. Using this reasoning in combination with the warm BT_3 and cold BT_{11} (Figures 2.4 and 2.5, respectively) it is concluded that the GSL pyroCb generated an extremely narrow ice PSD with very small r_e. Note that these two instruments orbit in a formation designed to observe the same scene—nominally flying within 15 seconds of each other—so differences in cloud morphology between observations is minimal and would not account for the apparent cloud top discrepancy.

An interesting feature of note in Figure 2.6c is the large value of radar reflectivity associated with apparently dry smoke just to the northwest of the pyroCb. This smoke is visible below $\sim$ 4 km between 60.7–60.8°N (compare with visible MODIS image in Figure 2.1e), and has values approaching -5 dBZ_e. Smoke by itself typically does not produce detectable CloudSat radar reflectivities, but being close to the source, it is likely that this smoke contains chaff or other relatively large biomass-burning debris that has not yet fallen out (*Fromm et al.*, 2012). Plotted on top of each panel in Figure 2.6 are the isotherms at $T = 0$ and -38 °C from the CloudSat ECMWF-AUX product—the freezing level (FL) and homogeneous freezing level (HFL), respectively.

These thermodynamic levels are known to be important boundaries for latent heat processes in convection, so they are denoted on these curtains for later reference. In Section 2.2.2 these thermodynamic boundaries are used along with the lifting condensation level (LCL) and equilibrium level (EL) to discuss the microphysical interpretation of the CPR reflectivity profiles of the GSL pyroCb and Alberta Cb.

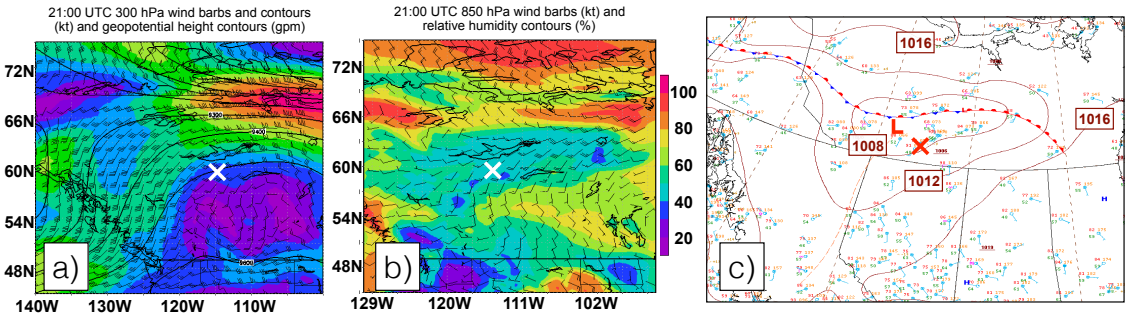

Figure 2.7: Synoptic-scale conditions from NARR showing winds and geopotential heights at 300 hPa (a), relative humidity and winds at 850 hPa (b), and surface frontal analysis (c). "×" symbols denote location of GSL pyroCb.

Also included is a statistical analysis of additional CPR intercepts through deep convective clouds (DCC) from the same region and season. Prior to that discussion, however, it is useful to establish the meteorology and fire precursors.

2.2.1 Weather and Fire Conditions

Figure 2.7 show the weather conditions in place prior to the initiation of convection. Winds and geopotential heights at 300 hPa from the North American Regional Reanalysis (NARR, *Mesinger et al.*, 2006) indicate the pyroCb formed at the southern edge of a jet entrance-region with an approaching shortwave trough aligned with the Pacific Northwest coast (Figure 2.7a). These conditions are known to be favorable for updraft formation and convection (*Uccellini and Johnson*, 1979). There was also an approaching increase in tropospheric moisture around 850 hPa (Figure 2.7b).

PyroCb modeling has shown mid-tropospheric moisture can be entrained into the convective column and contribute to instability aloft (*Trentmann et al.*, 2006), and observational statistics of all intense pyroCbs from 2013 within North America seem to confirm this (*Peterson et al.*, 2017b). Additionally, a strong low-level jet was also in place at 850 hPa which could have increased entrainment rates, helping to sustain the convection once it began (see wind barbs in Figure 2.7b). Ground observation sites operated by the government of the Northwest Territories recorded surface temperatures ≥ 32 °C, relative humidities $\sim 20\%$ and sustained wind speeds between 15-20 k h^{-1} (see Figures 2.8 and 2.9). These are the classic hot, dry, and windy conditions associated with intense wildland fires.

The traditional fire-weather indicators, the Haines Indices (*Haines*, 1988), were high-risk at the time of the GSL pyroCb with values of 6, 6, and 3, for the low-, mid-, and high-elevation variants, respectively. A stationary surface boundary was generating convection to the north/northwest around this time (Figure 2.7c), but did not appear to reach far enough south to directly impact the pyroCb location as evidenced by the lack of independent (non-pyro) cloud formation in the immediate vicinity of the fire (see Figure 2.1). Therefore, with favorable conditions, but without the dynamical trigger in place to initiate the convection, it is concluded that the fire itself was the trigger, and provided the necessary energy to initiate convection.

This conclusion is supported by the behavior of GOES-West fire radiative power (FRP) and kinetic fire temperature just before the GSL pyroCb began. A 36-hour time series of these values is shown in Figure 2.10, centered around the time of pyroconvection (green line). Within this timeframe, the temperature of the

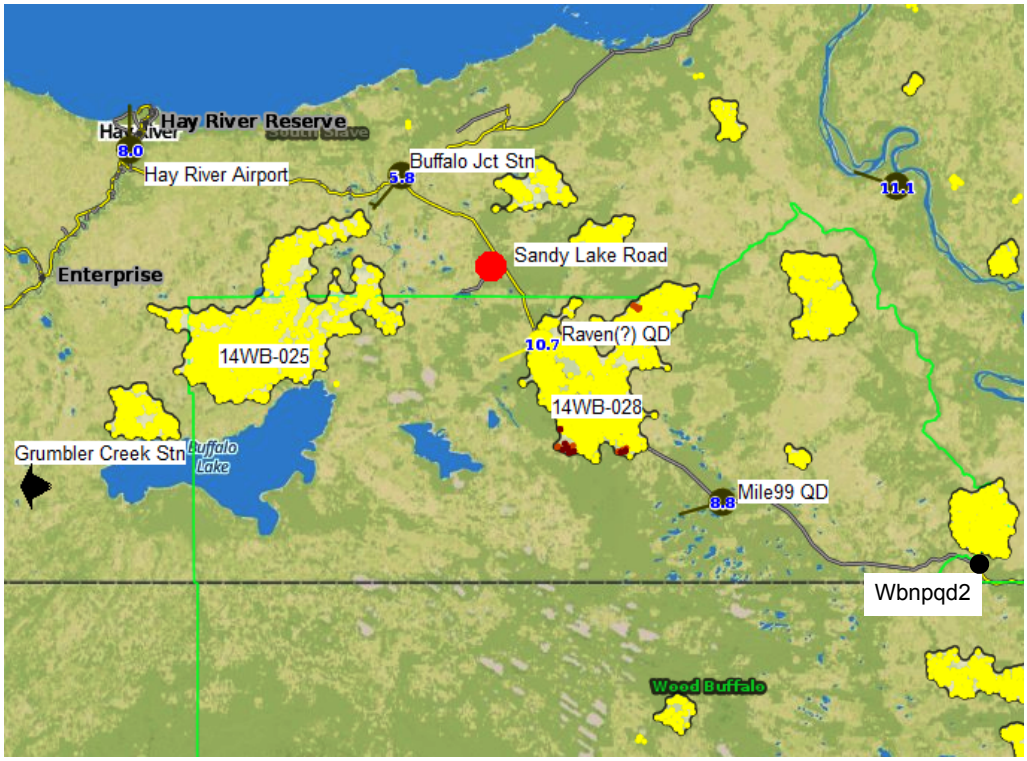

Figure 2.8: Map of fire perimeters (yellow with black outlines) and ground observation sites (black circles) maintained by the Government of the Northwest Territories. Fire 14WB-025 spawned the GSL pyroCb. Data from three of the observation sites shown in Figure 2.9. Red dot marks location of photographs in Figure 2.1g,h.

fire (black dots) oscillates between 500-700 K, but the pyroCb only forms after the strong increase in FRP (red line) just before to 18:00 UTC (12:00 MDT). The FRP increased from < 500 MW to > 6000 MW in less than 2.5 hours prior to the pyroCb, and fire temperatures increased by ~ 150 K over the same time. This preceding rapid increase in FRP is consistent with the conceptual model put forth in *Peterson et al.* (2017b). On this day the fire spread quickly, burning at an average rate of 2725 ha h^{-1} based on daily MODIS fire perimeter data, which is an order of magnitude

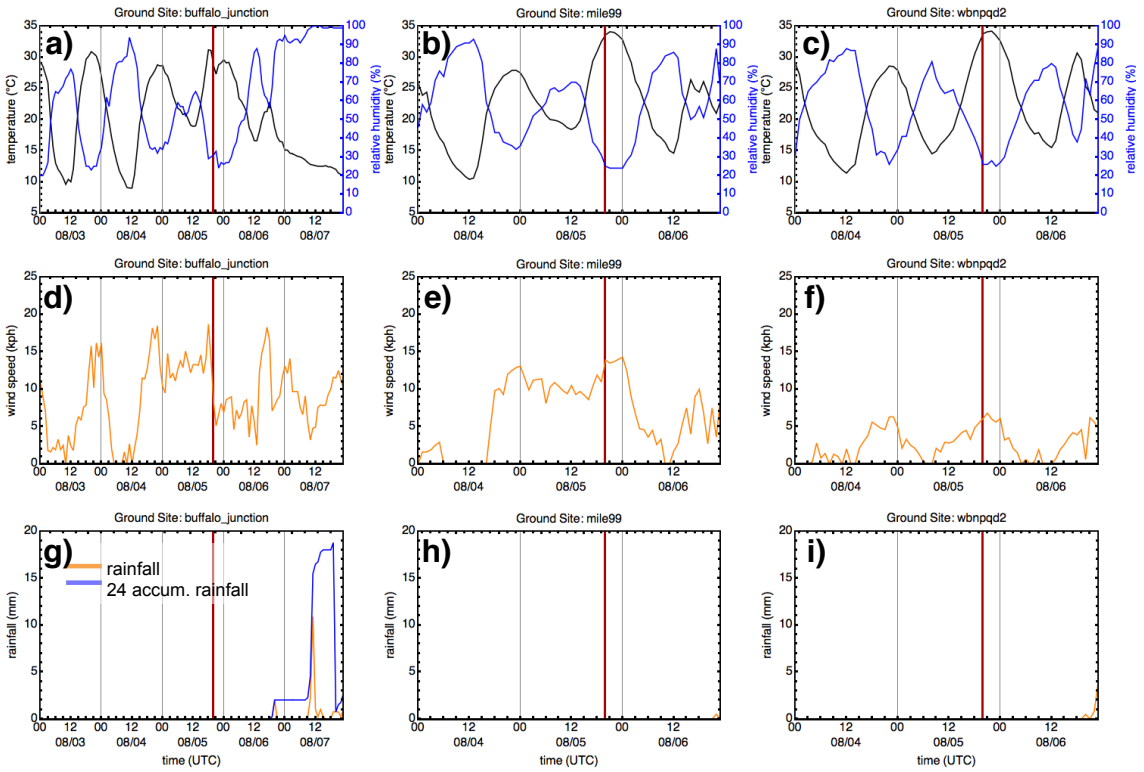

Figure 2.9: Time series of temperature and relative humidity (a–c; black and blue, respectively), wind speed (d–f) and both instantaneous and 24-hour accumulated rainfall (g–h; orange and blue, respectively). Red vertical line on time series plots denotes time of pyroCb. The pyroCb moved directly over the Buffalo Junction Station (a,d,g). Ground-site data courtesy of Franco Nogarin of the Government of the Northwest Territories.

larger than all other days on which the fire burned. The surface heat fluxes generated by such a rapid increase in FRP would certainly trigger the initial upward motion of surface and planetary boundary layer (PBL) parcels in an unstable atmosphere.

Figure 2.2.1 shows an interpolated sounding using the 5 August 12:00 UTC and

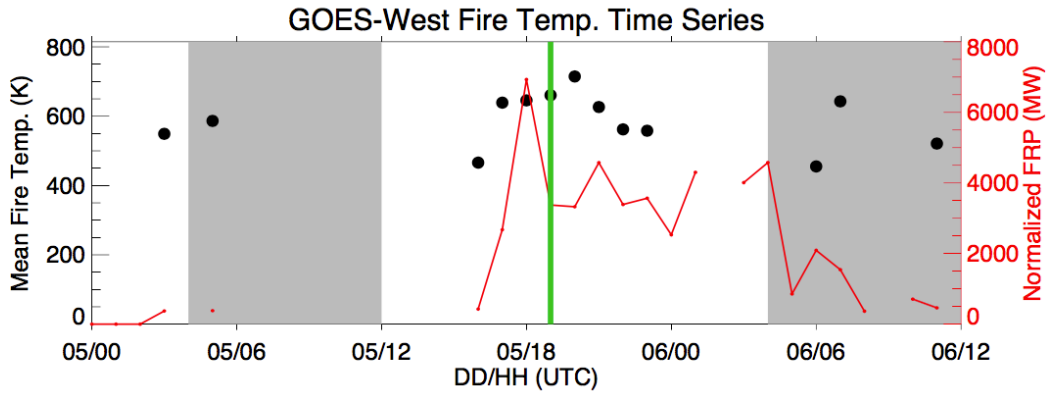

Figure 2.10: 36-hour time-series of normalized hourly GOES-15 FRP (red) and the mean estimated fire kinetic temperature (black) centered on the time of pyroCb (green line). Note the large fire temperatures and peak in FRP just before initiation. Gray shading is local nighttime. Gaps in FRP are due to invalid retrievals by the WF_ABBA algorithm likely due to weak fire output in the local evening/morning.

6 August 00:00 UTC soundings from the nearby Ft. Smith observation station. To construct this sounding, a temporal linear interpolation was used at each pressure to estimate the T and dewpoint temperature (T_d) at 18:00 UTC. Beneath the remaining PBL inversion, an atmospheric temperature adjustment is estimated at this time by connecting the top of the inversion with the mean surface temperature (T_s = 35 °C) measured at nearby ground stations (red dashed line below 1 km). This adjustment gives the sounding a general appearance of the "inverted-V" type, which was also shown in *Peterson et al.* (2017b) to be a typical precursor to intense pyroCb development.

The convectively available potential energy (CAPE) of the sounding without

the T_s adjustment is approximately 250 J kg^{-1} with an LCL of 1.8 km (not shown). This value increases to 1985 J kg^{-1} (blue shading in Figure 2.2.1) with an LCL of 2.5 km when using the T_s adjustment. One noteworthy feature of this sounding is the moist layer of air around 450 hPa associated with the advancing trough. The dewpoint depression at this pressure ($\sim$ 4.5 °C) is the lowest in the free troposphere. Entrainment of dry air into growing convection at this pressure would typically reduce buoyancy by cooling the air through evaporation (*Simpson*, 1980), but it is possible that the higher relative humidity associated with this layer would limit the drying effects of entrainment, and therefore be less inhibitive to vertical cloud development.

For pyroCb cases, it could be argued that the convective condensation level (CCL), rather than the LCL, is more appropriate to use as an estimate for cloud formation because the CCL represents the level at which a surface parcel would saturate from lifting due to heating, rather than forced dynamical uplift. However, in the case of the adjusted sounding, the CCL is found to be at an altitude $\sim$ 2.6 km, which is near enough to the LCL for the difference to be ignored. This occurs because the adjusted PBL temperatures closely follow a dry adiabatic profile. At the time the pyroCb began, T_s had almost reached the convective temperature ($T_c \simeq$ 36 °C) needed to trigger free convection above the condensation level. All these arguments have been made without considering an increase to the PBL air temperature from fire-enhanced surface heat fluxes, which should be quite large as indicated by FRP. Thus, although dynamical triggers were likely on the cusp of interacting with the GSL fire, and T_s was approaching T_c in nearby non-fire areas, it is safe to conclude

that the fire triggered the convection.

Additional features shown in Figure 2.2.1 are the cloud boundaries seen by CALIOP and CloudSat. The overshooting top peaks at $\sim$ 14 km and the cloud base (according to radar reflectivity) is near 4 km. The large difference between the LCL and the cloud base is most likely attributed to the large difference between the adjusted sounding and the actual T and T_d from surface heat flux contributions previously mentioned. Indeed, *Lareau and Clements* (2016) used ground-based mobile doppler lidar to show cloud bases over fires are typically much higher than LCLs determined from nearby soundings. The GSL pyroCb retrieved kinetic fire temperature was $>$ 300 °C, which leaves little doubt that the lower-most PBL lapse rate should be super-adiabatic (the CAPE under this condition would be on the order of 15000 J kg^{-1}). The equilibrium level (EL) of the adjusted sounding at 12.4 km is representative of the tropopause.

The gray shading in Figure 2.2.1 represents the inhibiting energy (CIN) needed to overshoot into the lower stratosphere to 14 km (CALIOP cloud top). The gray area is encompassed by this cloud top, and both the parcel temperature and sounding temperature, which have a vertex at the EL. This CIN value is 1160 J kg^{-1}), and—using parcel theory—would necessitate an updraft velocity on the order of 50 m s^{-1} at the EL for convection to reach the observed overshoot altitude. Unfortunately, the GSL pyroCb did not occur within range of a operational doppler radar, so no confirmation can be made, but this updraft velocity is consistent with intense overshoots from regular convection that have been modeled to inject water vapor into the lower-most stratosphere (*Wang*, 2003).

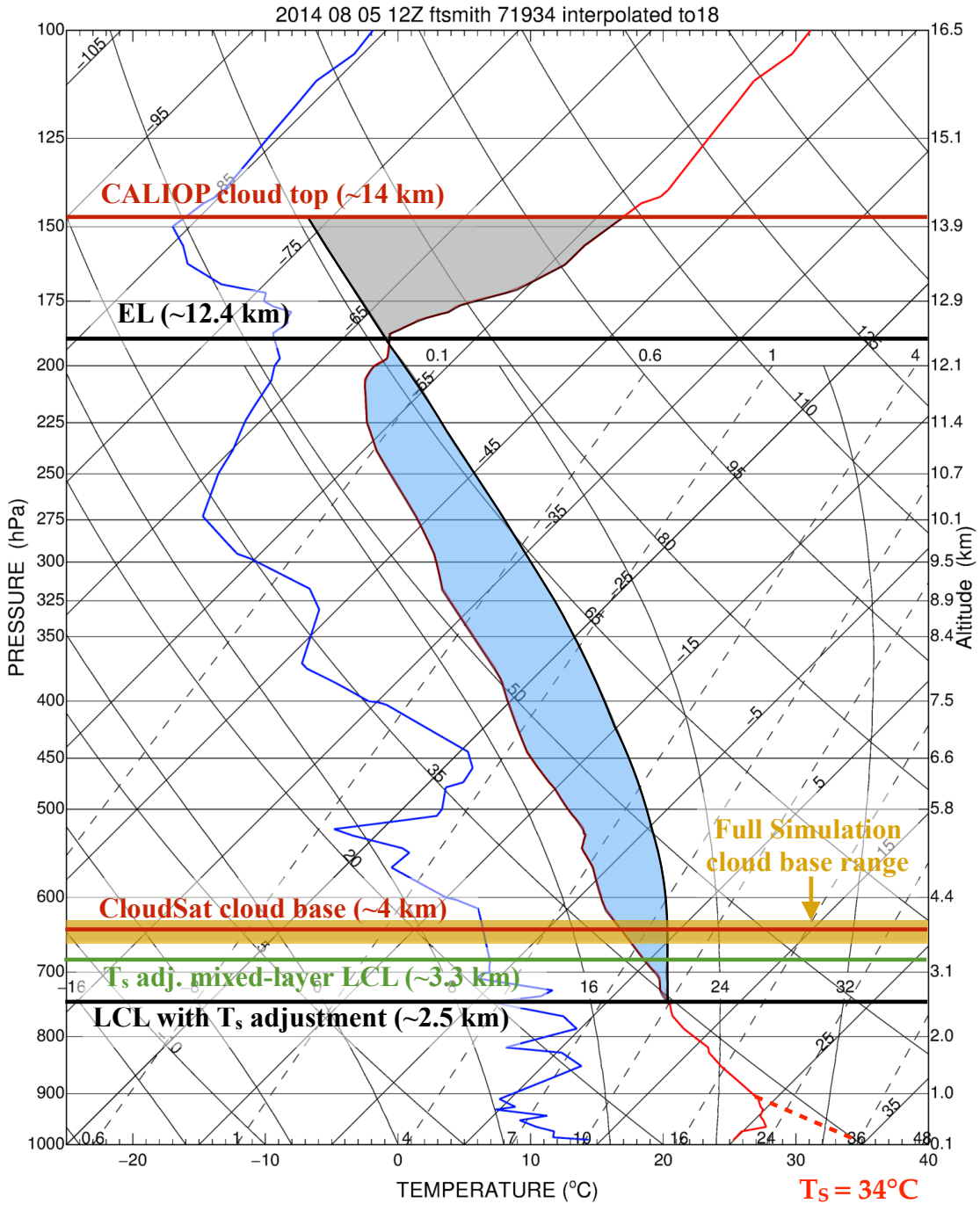

Figure 2.11: Interpolated 18:00 UTC sounding for the GSL pyroCb. (Continued on following page)

Figure 2.11: (continued) Red horizontal lines show CloudSat and CALIOP observed cloud boundaries. Atmospheric temperature between $\sim$ 900–1000 hPa is shown adjusted by using average ground station T_s (red dashed line), producing CAPE=1985 J kg^{-1} and CIN=1160 J kg^{-1} (blue and gray shading, respectively). Thick black horizontal lines show LCL and EL also computed with T_s. Green line is mixed-layer LCL (lowest 50 hPa) computed with T_s adjustment. CIN is limited to pressures between EL and the observed overshoot altitude in lower stratosphere. Dark yellow bar between 3.7–4.2 km is convective cloud base height range from "Full Simulation" modeling experiment (Chapter 3).

An interesting feature of the GSL pyroCb is the apparent lack of precipitation during its most intense stage. The Buffalo Junction ground station (denoted by the star in Figure 2.1) was operating nominally at the time when the pyroCb advected over its location, and recorded no precipitation even as the wind speed peaked above 18 km h^{-1} and surface temperature dipped by approximately 4 °C, presumably in response to downdrafts or temporary cloud cover (see Figure 2.9). Despite attempts to estimate precipitation amounts with CloudSat reflectivity, the estimates are not scientifically useful over land surfaces due to a lack of reliable path-integrated attenuation [*Matthew Lebsock, CloudSat product developer, personal communication*]. However, the CPR did measure significant reflectivity from the surface through the deepest part of the pyroCb, and Figure 2.6c shows a vertical gap between the surface return and the cloud base. These features provide additional confidence that there

was little-to-no precipitation during the mature stage of this event. Note that the narrow column of radar echoes observed below the cloud base in Figure 2.6c is likely dense smoke/lofted debris as discussed previously.

2.2.2 PyroCb and Cb Comparisons

Previous studies of pyroconvection have rarely had the ability to leverage observations of the interior during the active convective stage. Some exceptions to this generality include the following: aircraft have flown through developing pyrocumulus to take radiative flux measurements (*Gatebe et al.*, 2012), ground-based operational radar has been used to determine pyroconvective cloud tops from the upper-most echoes (*Dowdy et al.*, 2017), and doppler lidar has been deployed to remote locations to estimate entrainment rates and density currents within pyroconvection (*Lareau and Clements*, 2016). To our knowledge, however, only one other pyroCb case has had a direct penetration of the active convective column by CloudSat and CALIOP within the $\sim$ 12-year data record: the 2006 Wollemi case in Australia presented in *Fromm et al.* (2012). However, that CloudSat intersection occurred over 40 km to the east of the fire as the pyroCb was being advected away by strong winds, and it is possible that the CPR did not capture the full vertical depth of the cloud (see Figure 2.12). Note, however that Figure 2.12a shows the UVAI from the Ozone Monitoring Instrument (OMI) to be well correlated with the pyroCb.

Thus, the current GSL pyroCb case is strategic because of contemporaneous active profiling through the updraft core of a pyroCb and nearby Cb. In this section,

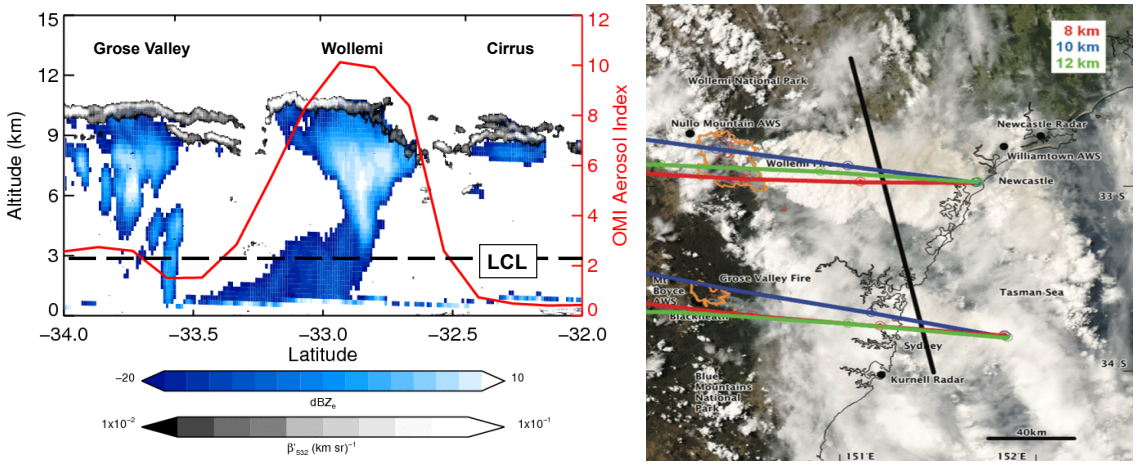

Figure 2.12: (Left) CloudSat reflectivity and CALIOP β'$_{532}$ through the Wollemi and Grose Valley pyroCb columns. (right) Trajectories initialized at the high OMI UVAI values through the ground track of these two nadir-looking instruments (black line) with the MODIS fire hot spots (orange outlines). This figure adapted from Figures 3 and 6 of *Fromm et al.* (2012).

CPR reflectivity is used to qualitatively estimate the internal hydrometeor structure of the GSL pyroCb by partitioning the profile according to the thermodynamic levels outlined in Section 2.2.1, and comparing it to the Alberta Cb and several other Cbs that were observed over the course of two months in the same region.

The mean CloudSat radar reflectivity profiles for the "deep convection" portions of the GSL pyroCb and concurrent Alberta Cb are shown in Figure 2.13a (blue and red lines, respectively). The shading about each of these two profiles is a horizontal standard deviation of CloudSat reflectivity within these portions of each storm. Here, "deep convection" is defined using the following two sequences

in an attempt to select the most intense profiles. This methodology is similar to the algorithm used in CloudSat Level 2 Product 2B-CLDCLASS with the following variations: the assignment of vertical cloud boundaries, the application of MODIS thermal infrared BT selection criteria, and the additional reflectivity thresholds. First, use the co-located CloudSat ECMWF-Aux product to a) determine the LCL altitude to use as the cloud base and b) determine the uppermost EL, and then use the 2B-CLDCLASS to c) find profiles with a single continuous cloud layer between the cloud base and EL. Second, use 2B-GEOPROF to d) confirm radar reflectivity values ≥ 6 dBZ$_e$ at 8 km a.m.s.l. or ≥ 4 dBZ$_e$ at 9 km a.m.s.l., and then use Aqua MODIS to e) confirm $\mathrm{BT}_{11} \leq -40$ °C and f) $\mathrm{BTD}_{12-11} > -0.5$ °C. After the deep convection CPR profiles are identified, the reflectivities are horizontally-averaged to reduce noise.

Also shown in Figure 2.13a are 15 additional deep convection core (DCC) profiles from June-August identified using the above algorithm for the same region in Canada (light gray lines). Table 2.1 gives the latitude, longitude and CloudSat "granule" identification number of all 17 DCC cases, including the GSL pyroCb, Alberta Cb. All of these DCC profiles are plotted as a function of altitude above the cloud base (local LCL) to normalize the differences since convective cloud growth begins at the cloud base. The horizontal lines in Figure 2.13a represent the relevant thermodynamic levels for the pyroCb (blue) and Cb (red), and show the freezing level (FL; 0°; dot-dashed), homogeneous freezing level (HFL; −38°; dashed), the equilibrium level (EL; solid) and the CloudSat cloud top (dotted). Here, the CloudSat cloud top is defined as the lowest level above which the median reflectivity drops

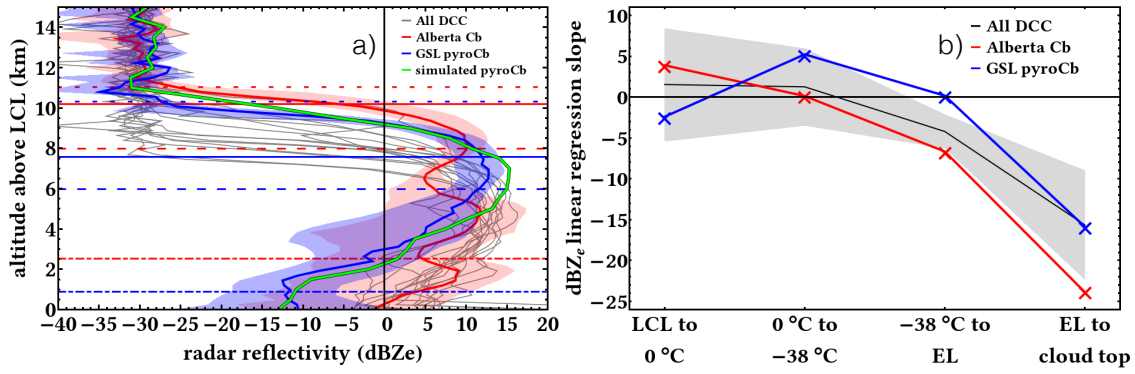

Figure 2.13: CloudSat horizontal-mean reflectivity profiles plotted as a function of height above the LCL through deep convection during the period 1 June–31 August 2014 near the GSL pyroCb. Shown in (a) are the GSL pyroCb (blue), Alberta Cb (red) and the additional 15 meteorological DCC profiles identified. Blue and red shading represent the standard deviation about the mean for GSL pyroCb and Alberta Cb. Horizontal lines in a) show FL (dot-dashed), HFL (dashed), EL (solid) and CloudSat cloud top (dotted) for both the pyroCb and Cb. Green line is the radar reflectivity from ARW Full Simulation pyroCb model run. (b) Black line shows the linear regression slope of mean reflectivity profiles between these thermodynamic levels and gray shading shows the standard deviation for all cases. Individual regressions of the GSL pyroCb and Alberta Cb cases are shown in blue and red, respectively.

below the noise threshold (-28 dBZ$_e$) for a distance of of 1 km. Defining the cloud top this way prevents spurious reflectivity values that may exist above a DCC from being identified as the cloud top. Situations with multiple cloud layers are flagged as non-DCC and ignored (i.e., the reflectivity increases above the noise threshold

Table 2.1: June–August 2014 deep convective core cases found using the modified CloudSat identification algorithm described in the text within a rectangular region between 50–65°N and 103–120°W, including the GSL pyroCb and Alberta Cb.

Date	approx. lat/lon (°N, °W)	CloudSat granule
06/02	(52,110)	43073
06/09	(57,144)	43175
06/11	(58,111)	43204
06/22	(52,107)	43364
06/25	(53,112)	43408
06/27	(55,110)	43437
06/29	(51,105)	43466
07/04	(59,114)	43539
07/06	(51,107)	43568
07/06	(55,108)	43568
07/06	(62,113)	43568
07/20	(54,111)	43772
07/24	(53,104)	43830
07/24	(61,109)	43830
08/05	(53,111) - Alberta Cb	44005
08/05	(61,115) - GSL pyroCb	44005
08/09	(56,106)	44063

for a continuous altitude range at heights > 1 km above a cloud top).

The pyroCb has a reflectivity of -10 dBZ$_e$ at cloud base compared with values ranging from approximately -5 to 5 dBZ$_e$ for the Alberta Cb and other meteorological DCC observations. The peak reflectivity for all DCC (including the GSL pyroCb) is $\sim$ 10 dBZ$_e$, and generally occurs between 5 to 8 km above the cloud base. The Alberta Cb shows a profile consistent with mid-level precipitation with two bright bands just beneath both the FL and HFL, whereas the GSL pyroCb profile has a more monotonic increase between the FL and HFL. Included for reference in Figure 2.13a is a simulated CloudSat radar reflectivity profile from the modeled

GSL pyroCb discussed in Chapter 3 (green profile).

To better quantify the differences in these profiles, a linear regression slope of reflectivity between the aforementioned thermodynamic levels is computed. Figure 2.13b shows the values of these regression slopes for the GSL pyroCb (blue), Alberta Cb (red) and all DCC cases (black; this includes the Alberta Cb). The gray shading is the standard deviation about the mean of all meteorological DCC. The pyroCb stands out with a few interesting features: 1) reflectivity between the LCL and FL decreases by -2 dBZ$_e$, whereas the meteorological DCC have positive slopes, 2) there is a large positive slope ($+5$ dBZ$_e$) between the FL and HFL, with DCC having a neutral or only slightly positive slope, and 3) the pyroCb has a neutral slope between the HFL and EL, whereas all meteorological DCC are strongly negative.

Radar reflectivity at 94 GHz through a cloud is proportional to the total condensed water content, so the profile regression slopes are representative of the change in integrated hydrometeor volume with height. Therefore a weak(strong) positive{negative} slope indicates a slowly(rapidly) growing{diminishing} hydrometeor distribution between the thermodynamic levels. Using this interpretation, the GSL pyroCb most likely has relatively weak droplet growth just above the cloud base that rapidly increases in the layer between the FL and HFL. This could be caused by an overabundance of CCN as predicted by the invigoration effect discussed in *Rosenfeld et al.* (2008), but it may also be a result of intense updrafts from surface heating and a subdued saturation ratio at the cloud base. The large positive slope in reflectivity (~ 5 dBZ$_e$) between the FL and HFL indicates a rapid

growth in total condensed water between these levels. This is likely due to the strong updrafts from the latent heat of freezing and/or buoyancy driven by surface heat flux. The slopes between the EL and cloud top are all strongly negative for all cases, including the GSL pyroCb. This is because of the rapidly diminishing condensate above the EL.

In the GSL pyroCb case, the regression slope between these levels is similar to the meteorological DCC slopes, even though the ice particles in these levels were shown to be smaller than the Cb, and should therefore have weaker reflectivity. Considering the difference in CALIOP and CloudSat cloud tops, however, the magnitude of this regression slope value is probably biased low because the actual cloud top (as seen by CALIOP) is about 1 km above the CPR-observed cloud top. If the regression was computed between the EL and CALIOP cloud top, the slope would be approximately -10 dBZ$_e$ per the depth of the layer.

These CloudSat reflectivity profiles augment the passive imagery to help show the GSL pyroCb contained a large number of very small ice particles near the cloud top. The warm BT$_3$, cold BT$_{11}$ and weak |BTD$_{12-11}$| confirmed the presence of small ice r_e, and since the $\sim$ 10 dBZ$_e$ reflectivity at EL is similar to other DCC (with larger ice particles) it is likely a result of a larger abundance of those small particles.

One result of this shift toward smaller, more numerous ice particles is an increase in anvil lifetime. Figure 2.14 contains four snapshots of GOES-15 IR brightness temperatures starting at 20:30 UTC on 5 August (a) and progressing every five hours until 11:30 UTC on 6 August. Similar to the results of (*Lindsey and Fromm*,

2008), the GSL pyroCb anvil (blue arrow) remains detectable with cold brightness temperatures for much longer than the Alberta Cb (red arrow) by several hours. The pyroCb anvil actually has brightness temperature values well below the −40 °C threshold (*Fromm et al.*, 2010) for at least 24 hours, at which point it becomes indistinguishable from nearby meteorological cirrus. On the other hand, the Cb anvil dissipates almost completely within the 12 hours depicted in Figure 2.14. A 25-hour animation of this GOES-15 imagery beginning at 19:30 UTC on 5 August is provided as Supporting Information (Movie S1) in *Kablick et al.* (2018). It is possible that upper-level descending air from a synoptic ridge contributed to the Cb anvil dissipating quicker than the pyroCb anvil, but the magnitude of this effect is unknown. However, in the next section it is shown that the ice within the pyroCb anvil remained detectable for greater than five days post-detrainment, which is several days longer than mid-latitude meteorological Cb anvils (*Lindsey and Fromm*, 2008).

2.3 Detrained Stratospheric Plume Properties

The GSL pyroCb plume was observed multiple times by A-Train instruments over the subsequent two weeks following 5 August. In particular, CALIOP and MLS were able to capture the particle and gaseous constituents, respectively. One of the objectives of this study is to quantify what effect this plume had on the downstream water VMR concentrations. To that end, a climatology of water VMR is computed using all available Level 2, Version 4 MLS H_2O data from the years

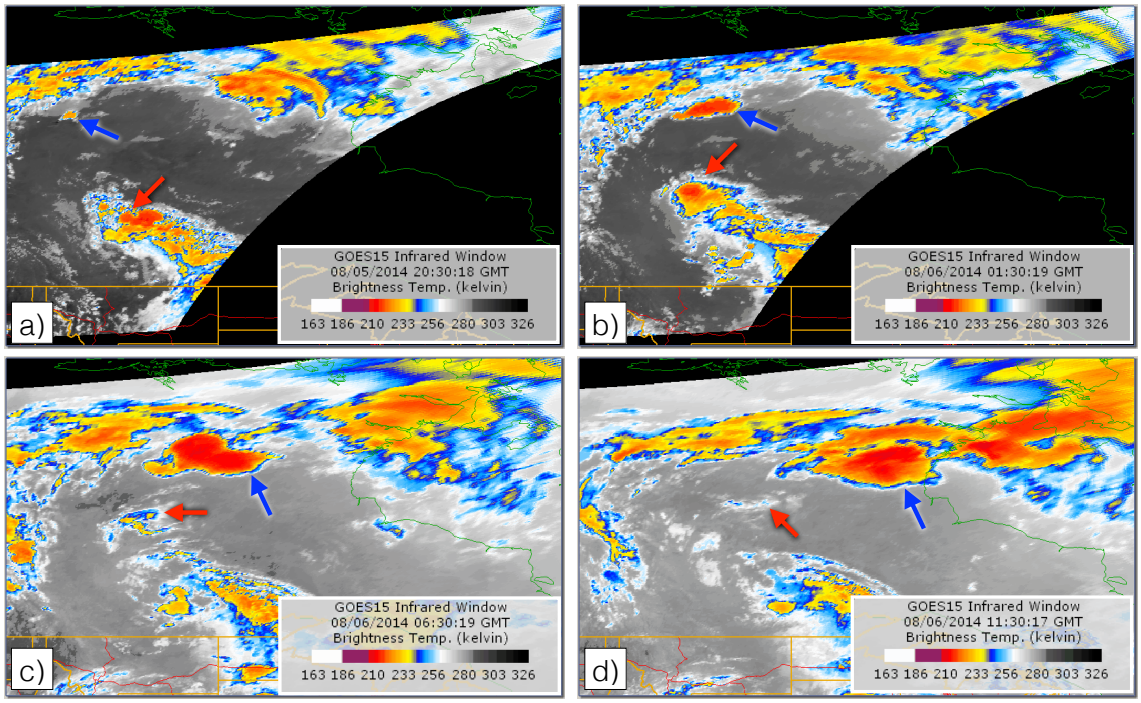

Figure 2.14: 5-hourly GOES-15 IR brightness temperature imagery starting at 20:30 UTC on 08/05 comparing the anvil lifecycle of the GSL pyroCb (blue arrows) and Alberta Cb (red arrows).

2005–2014 (*Livesey et al.*, 2018) for the months of June-August.

MLS H_2O data is retrieved on pressure surfaces, and is considered scientifically valid for pressures $\leq$ 316 hPa. Because the focus is on the UTLS, the MLS Temperature product is used to convert these pressures to potential temperatures (θ), and then average the vertically-resolved H_2O profiles on isentropic levels. All data from this time period is then averaged on a 10°×5° (longitude×latitude) grid. Individual plume anomalies are then computed by subtracting the three-dimensional climatology from observed values in each MLS profile. The MLS GPH product (geopotential

height, *Schwartz et al.*, 2008) is used to approximate the altitude above mean sea level (a.m.s.l.) of the vapor anomalies for co-location with the CALIOP backscatter profiles. This step ensures that the analyzed vapor concentrations are spatiotemporally concomitant with any aerosol/ice layer identified using CALIOP.

Figure 2.15 shows the path the plume followed, and the individual observations made by CALIOP and MLS over the two weeks post-UTLS injection. The map in the upper panel has contains a Hybrid Single-Particle Lagrangian Integrated Trajectory model (HYSPLIT) forward trajectory (*Stein et al.*, 2015) initialized from the first A-Train observation segment (denoted with an "A") on 5 August. Additional observations are noted along the trajectory with eight orbit segment nadir-tracks denoted with letters B–I.

The plume made its way eastward over the Atlantic during the week following injection, and then it made a cyclonic loop around western Europe between 10-15 August as the winds in the UTLS were being driven by a baroclinic storm. Over the following days it moved over northern Asia as the CALIOP backscatter signal weakened, until it became undetectable after 20 August. These detections were corroborated using the nearest HYSPLIT hour that matched the orbit segment (red circles along the trajectory). MLS water VMR was synchronized with CALIOP backscatter, and the VMR anomaly was computed using the climatology at that location.

The nine panels below the map in Figure 2.15 correspond with the A-I observations locations. Each of these panels contains the "vertical feature mask" (VFM) product derived from CALIOP β'_{532}, the MLS water vapor anomaly in percent (open

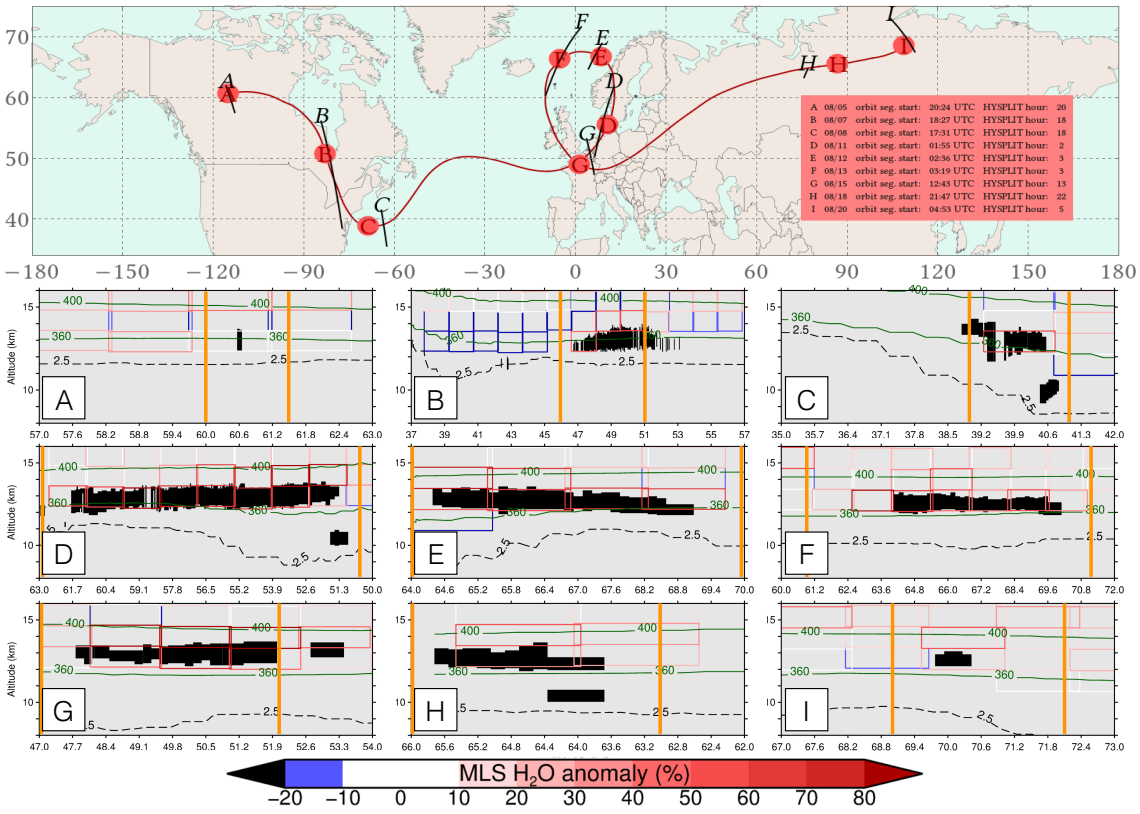

Figure 2.15: (Top) Map of HYSPLIT trajectory showing intersections with relevant A-Train orbits. Segments are labeled A–I, and the date, segment time stamp and corresponding HYSPLIT hour are given in the inset table. (A–I) CALIOP VFM curtains showing the "stratospheric features" in black with MLS water vapor anomalies overlaid as colored rectangles (% relative to local climatology). Black dashed line is 2.5 PVU dynamical tropopause and green contours are potential temperature (K) from ERA-I reanalysis. Abscissae of A–I are in degrees of latitude, and orange vertical lines bound the curtain profiles used in Figures 2.17, 2.18. Corresponding β'_{532} curtains are shown in Figure 2.16.

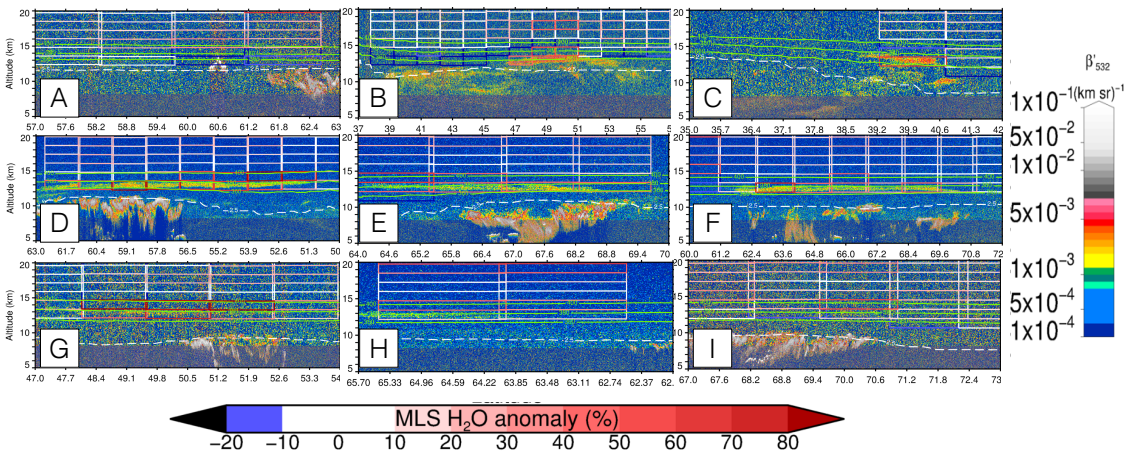

Figure 2.16: As in Figure 2.15, but showing the β'_{532} instead of "stratospheric features" identified using the VFM product. Note the altitude range is extended compared with 2.15 to show more of the backscattering differences between strongly attenuating clouds in the troposphere with the stratospheric pyroCb plume.

squares plotted to match the limb-sounding measurement volume geometry; color bar below each panel), the 2.5 PVU isosurface used to approximate the dynamical tropopause location (white dashed line), and the $\theta = 360$, 380 and 400 K isentropes (green lines). Note the good correspondence between the positive VMR anomalies and the plume locations in the stratosphere at each observation (segments B-I) after the primary injection from the active pyroCb (segment A). The nighttime observations by CALIOP (segments D, E, F, and H) contain less noise, and the backscatter plume is more readily discernible. Many of the MLS observations contain anomalous VMR values $> 80\%$ surrounding the CALIOP plume locations. Figure 2.16 shows the native CALIOP β'_{532} used in determining the VFM areas in Figure 2.15.

Individual profiles of the VMR values corresponding with these plume inter-

sections are shown in Figure 2.17, plotted here using potential temperature as the vertical coordinate. Approximate altitude from the GPH product is shown on the right-side ordinate axis. The red lines are the absolute magnitude (not the anomaly) of the VMR observation, and the blue lines represent the climatology values that correspond with the plume-portion of the orbit segment shown in the Figure 2.15 map.

To help orient the viewer, the individual curtains shown in Figure 2.15A–I span a larger latitude range than the plume width denoted on the Figure 2.17A–I panels. Horizontal gray dashed lines mark the 360 and 400 K isentropic boundaries to which the plume was confined during its observable lifetime. Note the increase in VMR at θ = 390 K ranging from 1 to 5 ppmv greater than the climatology as the plume ages and undergoes the cyclonic movement in segments D–G. In the two final segments (H, I), individual VMR anomalies are still as large as 2 ppmv above climatological values.

The pyroCb injected a large abundance of small ice particles combined with smoke that underwent diffusion over the subsequent days. To test the hypothesis of ice sublimation increasing down-stream absolute humidity within the plume these VMR anomalies are combined with MLS retrievals of ice water content (IWC). Figure 2.18 shows a time series of the MLS VMR anomalies (black line) along with corresponding MLS IWC observations (blue line) and CALIOP depolarization ratio (δ_{532}, red line). Vertical gray dashed lines denote the times of each orbit segment.

The MLS values plotted in Figure 2.18 are averaged between 360–400 K for the plume locations within each orbit segment, and the CALIOP depolarization

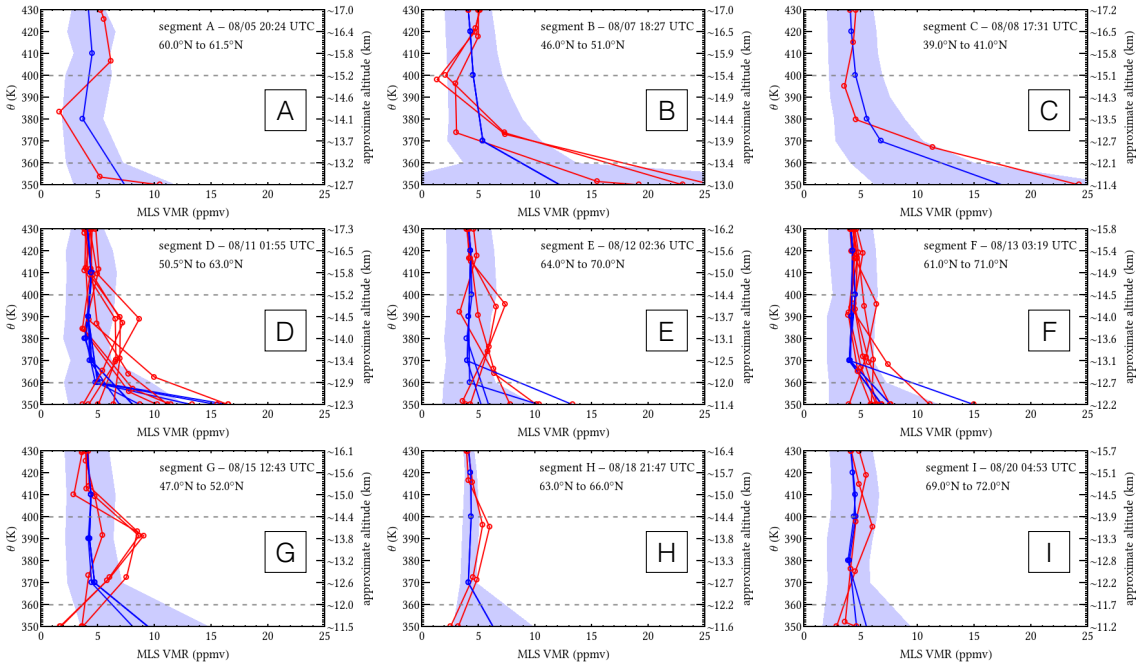

Figure 2.17: MLS water vapor profiles through the pyroCb plume (red lines) observations shown in Figure 2.15. Blue lines are the profiles of background WVMR from the 2005–2014 JJA gridded climatology that fall within the region bounded by orange lines in panels A–I in Figure 2.13, blue shading shows the standard deviation of these background profiles. The gray dashed lines delineate the potential temperature boundaries of the plume over the course of its observable lifetime.

ratio values represent an averaged value corresponding to all backscatter pixels that fall within to the MLS measurement volume. The initial A-Train observation (A; hour 0) has an IWC value of 8.3 mg m^{-3}, and then over the next 50 hours reduces to 1 mg m^{-3}, at which point the VMR anomaly has become positive. Over the subsequent 100 hours, IWC diminishes to 0 mg m^{-3} as the VMR anomaly increases to a plume-averaged value of $\sim$ 2 ppmv (45%), and remains large for the next three

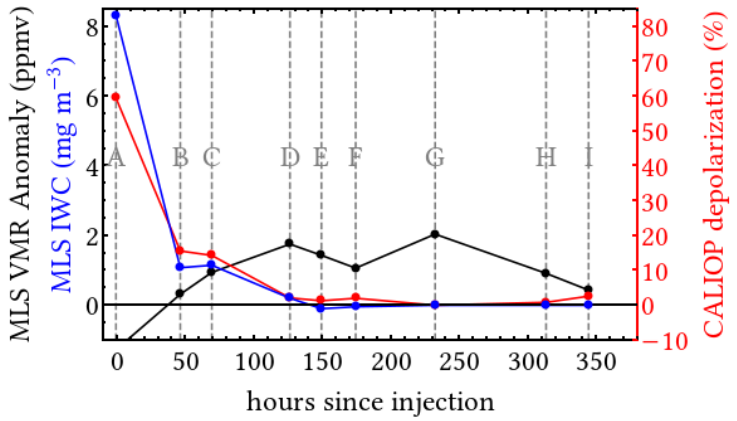

Figure 2.18: Mean values of MLS WVMR anomalies and IWC (black and blue lines, respectively) and median CALIOP δ_{532} (red lines) over the two-week observable lifetime of the GSL pyroCb plume. Each MLS point in this time series represents a per-profile vertical mean between 360–400 K for measurements encompassing the plume (dashed lines in Figure 2.14), and each CALIOP point is the median value for the entire "stratospheric feature" between 360–400 K.

observations (segments E–G). After the plume has aged 350 hours, there are no more detections made by the A-Train that can confidently be attributed to the pyroCb source.

CALIOP depolarization ratio is examined as an additional test for ice presence. On a pixel-by-pixel basis, values of δ_{532} should approach $\sim$ 50% when significant amounts of ice are present (*Hu et al.*, 2009). However as shown in Figure 2.18, the average values remain less than 2% at all observation times. These values are artificially small because of the large number of insignificantly depolarizing pixels

that fall within the MLS measurement volume included in the average. Therefore, the δ_{532} values shown in Figure 2.18 should be viewed as a qualitative representation of the combined depolarization from all particles (and molecules) that fall within the MLS retrieval volume.

As was shown in Section 2.2, the pyroCb anvil is comprised of ice, but the average δ_{532} of segment A is small because at that initial observation, the anvil had a very small footprint within the MLS volume. Additionally, it is likely that in noisy daytime observations when bright clouds are present in the troposphere below the plume (e.g., segment G) the increase in δ_{532} would be affected by multiple scattering within those clouds, so the relatively large δ_{532} seen in G is probably unrealistic. When accounting for the issues with segments A and G, the behavior of δ_{532} loosely resembles the MLS IWC behavior. Segments B–F and H–I show a diminishing δ_{532} as the VMR initially increases and then decreases with age.

Chapter 3: Cloud-Aerosol Modeling of Active PyroCb Convection

The non-hydrostatic and compressible Advanced Research Weather Research and Forecasting (ARW) model (*Skamarock et al.*, 2005) is used to estimate the sensitivity of the GSL pyroCb to specific variables. The model is run for four conditions. First, a control pyroCb simulation is established using the geography and weather forcing of the GSL pyroCb event (Full Simulation). The remaining three model runs are repeats of the Full Simulation with individual alterations to initial conditions. The second simulation has aerosol concentrations over the fire reduced to background values (Low Aerosol), the third has reduced moisture advection in the PBL and free troposphere (Low Moisture), and the fourth has surface sensible and latent heat fluxes reduced to background values (Low Heat Flux). The purpose of these simulations is to test the effect of surface CCN concentrations, moisture entrainment, and surface heating on pyroCb cloud properties.

3.1 Model Experiments

The simulations are run for a 24-hour period starting at 12:00 UTC on 5 August and ending at 12:00 UTC on 6 August. A fifth-order monotonic advection scheme is used for the advection of cloud variables (*Wang et al.*, 2009), and radiation

is handled with the one-dimensional Rapid Radiative Transfer Model (*Fouquart and Bonnel*, 1980; *Mlawer et al.*, 1997). To capture the mesoscale structure of the pyroCb, and to resolve cloud processes, the model horizontal domain is set to 200×200 km^2 using a 500 m resolution and a domain depth of 20 km at 200 m resolution. A bulk double-moment microphysics parameterization is used that emulates a bin microphysics scheme for the calculation of collection and sedimentation processes. This parameterization is generally referred to as the bin-bulk scheme and was first implemented into Regional Atmospheric Modeling System (RAMS) at Colorado State University (*Walko et al.*, 1995; *Saleeby and Cotton*, 2008).

For the Full Simulation, the surface sensible and latent heat fluxes are set to 150 and 310 W m^{-2}, respectively in the non-fire regions of the domain. A hot-spot representing the fire is modeled as a circle centered in the domain with diameter=20 km, and sensible and latent heat fluxes are set to 15000 and 1800 W m^{-2}, respectively. These values are based on the previous modeling studies by *Trentmann et al.* (2006) and *Luderer et al.* (2006). *Beringer et al.* (2003) noted that sensible heat fluxes are much greater than latent heat fluxes over fire (large Bowen Ratio), and *Trentmann et al.* (2006) noted that there exists a positive feedback between these fluxes due to increased entrainment of low level moisture as a fire emits more sensible heat.

In the present model setup, this interaction is ignored, and all heat values are prescribed without any meteorological coupling. Therefore, the results here are not designed to mimic reality with respect to fire-atmosphere interaction, but are idealized so that sensitivity of convective properties between model runs can be

more readily compared. Directly over the fire, the aerosol concentration is set to 15000 cm^{-3} within the PBL, and decreases exponentially with height in the free troposphere. Within the PBL at non-fire locations, the concentration is set at 150 cm^{-3}, also decreasing exponentially with height above this level.

A big question regarding pyroCb development is the individual effects of surface heat fluxes, fire-produced aerosol particles, and moisture entrainment illustrated by *Peterson et al.* (2017b). Toward the goals of assessing convective intensity, properties of detrained cirrus, and impacts on UTLS moisture, it is useful to re-run the control simulation with high heat flux/low aerosol and with low heat flux/high aerosol. To estimate the effect of the former, the Low Aerosol simulation is done by repeating the Full Simulation with PBL aerosol concentrations reduced to the background level (150 cm^{-3}). Then, to estimate the role played by surface heat fluxes, the Low Heat Flux run maintains the large aerosol concentrations of the Full Simulation, but has reduced surface latent and sensible heat fluxes to the background values (310 and 150 W m^{-2}, respectively) in the within fire spot.

However for these conditions, it is found that surface latent and sensible heat fluxes in the fire spot are too low to form a cloud, so a potential temperature perturbation is prescribed over the fire spot to trigger a cloud, following *Weisman and Klemp* (1982). The horizontal extent of this perturbation is identical to that of the fire spot and the vertical extent is 2.8 km, and the maximum perturbation is 1.8 K. This perturbation has been used by numerous previous studies and considered to have negligible influences on cloud development, although it triggers the formation of a cloud.

As discussed in Chapter 2, the GSL pyroCb occurred during a substantial advection of moisture in the mid-troposphere. NARR data also showed an immediate increase in surface relative humidity at the time of convection (20–30% $\rightarrow$ 50–60%). It is possible this advection contributed a significant amount of moisture to the atmosphere over the fire—and therefore instability—just before pyroCb formed, or that it was entrained during convection.

To test whether these moisture sources had any impact on convection, the Full Simulation run is repeated again by reducing the level of moisture advection by a factor of 5 in the PBL and free troposphere throughout the simulation period (Low Moisture run). Since the simulations are started two hours prior to the formation of the pyroCb, this reduction is applied to the period before and after convection starts to limit entrainment from both the surface through the cloud base and the free atmosphere through the sides of congestus.

3.2 Results

In Figure 2.1, the pyroCb anvil is observed to advect to the northeast of the fire spot due to the southwesterly winds at the outflow altitude. In the Full Simulation, a convective column forms over the fire spot, and is accurately advected northeastward as the GSL pyroCb does in reality. Figure 3.1 shows the field of cloud-ice mixing ratio (representing the outflow anvil) at the top of the simulated pyroCb and at a time that corresponds to the satellite image in Figure 2.1f. The modeled anvil cirrus cloud is $\sim$ 80 km in diameter and is in fairly good agreement

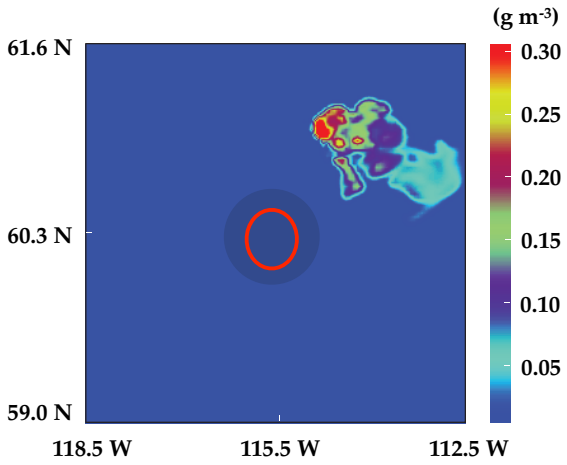

Figure 3.1: ARW Full Simulation ice particle mixing ratio within the cirrus outflow at the equilibrium level ($\sim$ 13 km) during the mature stage of pyroconvection (approximately 3 hours after convection began). Red circle denotes fire hot-spot location used to initialize the simulation. Compare with VIIRS image in Figure 2.1f.

with the VIIRS observation, giving confidence in the ability of the ARW setup to reproduce the morphology.

Among the observed CloudSat 94 GHz radar profiles shown in Figure 2.13 is a simulated 94 GHz radar reflectivity profile from the Full Simulation modeled pyroCb (shown as green line). This profile is shown plotted above the cloud base, and the simulation time corresponds with the CloudSat overpass time of 20:20 UTC, which is $\sim$ 2 hours after the simulated convection began. The shape of the Full Simulation radar profile reasonably matches the shape of the GSL pyroCb CloudSat-observed profile, indicating the model represents the high cloud base reasonably well.

As mentioned previously, heat fluxes over fires can produce extremely large

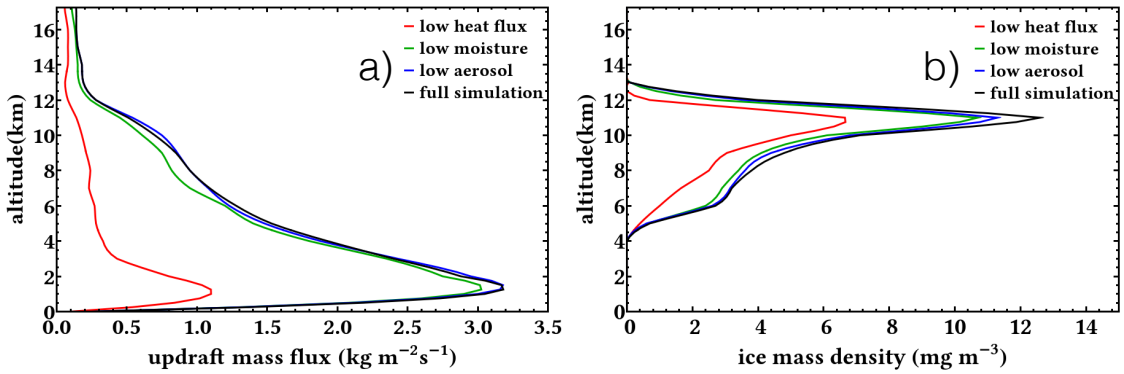

Figure 3.2: Profiles from four pyroCb model simulations showing the averaged vertical distributions of the a) spatiotemporally-averaged updraft mass fluxes, and b) ice mass densities. See text for descriptions of the four simulations.

updrafts from enhanced buoyancy, but increased CCN concentrations are also known to enhance updrafts from latent heat release. The results of *Luderer et al.* (2006) showed heat fluxes dominate the updraft velocities over aerosol influences, and that result is confirmed here. Figure 3.2a shows the vertical distributions of the time- and domain-averaged updraft mass flux—a standard representation of the cloud dynamic intensity—for all four model runs. The black line is the Full Simulation, which has a peak value of 3.2 kg m^{-2} s^{-1} at the top of the PBL.

The bump in the updrafts between 8–11 km is due to a buoyancy push from the latent heat of freezing. The Low Aerosol run (blue line) closely follows the Full Simulation profile throughout the depth of the troposphere with minimal deviation. The impact of limiting moisture entrainment (green line) is slightly stronger than limiting aerosol concentrations. Although this profile is similar to the Full Simula-

tion mass fluxes, the model shows a greater reduction in updrafts, especially between 7–9 km where mass fluxes are 10–15% less than the Low Aerosol run. This implies that any invigoration from an aerosol increase is likely dependent on the availability of moisture. However, the most significant negative impact on the strong updraft mass fluxes demonstrated in the Full Simulation comes from a reduction in surface heat fluxes (red line), which is ~ 4 times smaller than the other runs. Limiting sensible and latent heating from the fire down to background values produces a peak updraft mass flux of 1.1 kg m^{-2} s^{-1} and a upper tropospheric peak of ~ 0.3 kg m^{-2} s^{-1}. Among the variables tested here, this result confirms fire-induced surface heat fluxes play the most important role in pyroCb intensity.

The different model runs produce comparable differences in cloud-ice mass densities (Figure 3.2b). Similar to the updraft mass fluxes, the fire-induced surface heat fluxes play the most important role in the amount of cloud ice particularly just below the tropopause. The ice mass density peaks ~ 12.8 g m^{-3} at the EL for the Full Simulation with minimal reductions in the Low Aerosol and Low Moisture runs (~ 11.5 and ~ 10.8 g m^{-3}, respectively). Of the various ways that surface heat fluxes, moisture entrainment and aerosol concentrations may influence ice cloud properties, the common mechanism is updraft buoyancy. These ice mass densities are not surprising given the updrafts shown in Figure 3.2a.

The additional mechanism to consider is an increased number density of ice particles caused by an increased droplet number density from CCN nucleation. Figure 3.2b shows that this mechanism does not seem to have much influence on the ice mass density because the Low Aerosol result does not deviate significantly from

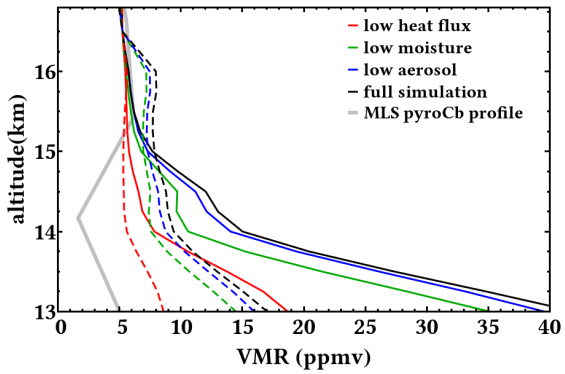

Figure 3.3: Profiles of WVMR spatiotemporally averaged for each simulation for all cloud regions within the domain (solid lines), and surviving water post-detrainment (dashed lines), estimated here to be 30%. The latter includes vapor contributions from ice sublimation and existing absolute humidity. The MLS observation during the active pyroCb—when no WVMR enhancement is yet present—is shown as a gray line as a reference to the background profile.

the Full Simulation result. It is possible the microphysics scheme is unable to substantially account for changes in surface aerosol concentrations, but it is more likely that the updraft velocity is overwhelmingly more important on determining the ice mass density. Therefore, the results indicate that increased CCN concentrations have much less importance on the ice distribution than the surface heat flux.

Vertical distributions of the averaged water vapor mixing ratio from all four simulations are shown in Figure 3.3, plotted above the model tropopause ($\sim$ 13 km). These values (solid lines) are horizontally averaged in the non-cloud areas, which are defined as columns with a zero liquid and ice water path. Again, there

are differences between vapor detrainment values from the Full Simulation and the other three runs, but the Low Heat Flux run has the most significant deviation. For example, at 14 km the Full Simulation has a clear-sky average VMR=13 ppmv, the Low Aerosol run has 12 ppmv, the Low Moisture run has 9 ppmv and the Low Heat Flux has < 2 ppmv. These values, however, are instantaneous values after the pyroCb ceases, and do not account for sublimation from the aging ice cloud detrained at these altitudes.

Because MLS observations showed the GSL pyroCb plume absolute vapor concentrations peak between 8–9 ppmv after one week, it appears there should be approximately a 30% survival of total water from both detrained vapor and sublimated ice in order to reach these values. This 30% survival amount is applied to each model run and shown as dashed lines in Figure 3.3. The cloud ice mass density from each simulation is converted to parts per million and is combined with the molecular water vapor and multiplied by 0.3. At 14 km, the value from the Full Simulation is between 7–8 ppmv, the Low Aerosol is ~ 7 ppmv, the Low Moisture is ~ 6 ppmv, and the Low Heat Flux is ~ 3 ppmv.

Chapter 4: Diabatic-Lofting of Injected PyroCb Plumes

The physics behind plume self-lofting are straight forward (*Crutzen and Birks*, 1982; *Radke et al.*, 1990). The basic idea is that a sufficiently optically-dark aerosol pall absorbs shortwave electromagnetic radiation and undergoes diabatic heating within a volume of air that otherwise would not have such a heating anomaly. This diabatic heating increases the temperature within the air volume and generates buoyancy. Upward motion of the air volume continues until it reaches thermal equilibrium, either from reaching an altitude at which ambient temperature causes radiative equilibrium or from turbulent diffusion of the aerosol reducing the volume absorption coefficient.

This radiatively-induced self-lofting of dark aerosol plumes was studied extensively throughout the 1980s when the so-called Nuclear Winter phenomenon gained traction during the Cold War (*Crutzen and Birks*, 1982; *Turco et al.*, 1983; *Sagan et al.*, 1983; *Thompson et al.*, 1984; *Turco et al.*, 1984; *Thompson and Schneider*, 1986; *Turco et al.*, 1990). During that time, pyroCb had not yet been discovered, and the smoke that made it into the stratosphere in the Nuclear Winter modeling scenarios was based on a best-estimate of the density and optical properties of tropospheric plumes that would emanate from urban conflagration (typically not

from the direct stratospheric injection of plumes from detonation columns of bombs themselves).

The studies relied on extremely dense smoke plumes and highly absorptive optical properties to get the smoke to gradually make its way into the stratosphere through diabatic self-lofting, overcoming the stability of the tropopause. More recent Nuclear Winter research has relied on the same hypothetical smoke conditions (*Robock et al.*, 2007a,b; *Toon et al.*, 2007). It should be noted that several of the Nuclear Winter studies referenced the World War II bombing campaign in both Europe and Japan and the resulting firestorms as an event that could be scaled-up to replicate a Nuclear Winter precursor. No convincing evidence has ever been published showing that the Dresden Firestorm in Germany, the intensive sustained bombing campaigns in Japan, nor the Hiroshima and Nagasaki nuclear detonations had any impact on stratospheric radiative budgets or surface climate (*Robock and Zambri*, 2018).

PyroCb events, on the other hand, are known to directly inject smoke into the stratosphere because of the impact that the surface heat fluxes have on convective updraft velocities (*Luderer et al.*, 2006; *Trentmann et al.*, 2006, and Chapters 2, 3 herein). It remains unknown whether the Nuclear Winter scenarios and their proposed plume evolutions are valid because such a high-yield event thankfully has never occurred, but based on peer-reviewed pyroCb research both modeling and observational plumes from massive wildfires are stratospherically-injected through deep convective processes and not through slow ascent across the tropopause by radiatively-induced self-lofting.

However, once the pyroCb plume is in the LS, self-lofting can be observed. Previous research has attempted to associate pyroCb plumes with a self-lofting mechanism, specifically with the 2009 Black Saturday plume (*Laat et al.*, 2012). Unfortunately that study misinterpreted the maximum height of the active convection columns from several pyroCbs on Black Saturday, and assumed a high rate of radiative heating in order to put the plume into the stratosphere. Ground-based radar observations show that the conclusions of *Laat et al.* (2012) were flawed because a majority of the plume was directly injected into the LS prior to self-lofting (*Dowdy et al.*, 2017).

This chapter explores pyroCb plume diabatic self-lofting. The focus is on the extreme 2017 PNE case, but comparisons are made with the Black Saturday plume and the comparatively much weaker 2014 GSL pyroCb. LS observations are examined in the days and months that followed these events, and a diabatic model framework is developed using solar radiative anomalies from extinction observations and an empirical heat accumulation model. Prior to that analysis, it is insightful to discuss the amount of aerosol stratospherically-injected. Examining the very large amount mass of aerosol injected during the 2017 PNE will put the diabatic-lofting discussion in better context.

4.1 Stratospheric Injection Mass

As was demonstrated in *Peterson et al.* (2018), the 2017 PNE plume was unprecedented in the amount of pyroCb aerosol directly injected into the stratosphere.

The aerosol mass loading was estimated to be 0.2 ± 0.1 Tg based on a combined passive and active remote sensing methodology, using CALIOP lidar and OMPS Nadir Mapper (NM) instrument. The estimation leveraged the fact that OMPS UVAI (and products of similar instruments like OMI and TOMS) is larger when either the plume optical thickness and/or altitude is increased, and that for sufficiently thick UTLS plumes there is an empirical threshold of UVAI that delineates stratospheric vs. tropospheric presence (*Torres et al.*, 2002). In other words, when a plume is optically opaque, physically deep and has layers above and below the tropopause, there exists a UVAI value that would determine which pixels are in the stratosphere and which pixels are in the troposphere.

This methodology is made possible by a fortuitous combination of earth-observing satellite instruments making nearly simultaneous measurements in sun-synchronous orbits. For example, the OMPS NM on-board Suomi NPP collects a wide swath of imagery in the afternoon ascending orbital node that was typically within a 1–2 hr of vertical profiles from the CALIOP lidar (at the time of this writing, CALIPSO has now been moved out of the A-Train to a lower orbit with CloudSat, and the orbital characteristics cause a periodic overlap with NPP that will continuously change with correction maneuvers). The rest of this section briefly details the main results of *Peterson et al.* (2018)—that a pyroCb injected an aerosol plume on the scale of a small volcano—and provides the methodology-validation that the present author undertook as a part of that study.

The total mass of aerosol injected into the stratosphere is defined as the product of the mass density (M_ρ) and the stratospheric plume volume (V). Mass density

of the aerosol plume is defined as

$$M_\rho = \frac{\beta'_{532} S}{\sigma}, \tag{4.1}$$

where the S is the extinction-to-backscatter ratio (colloquially referred to as the "lidar ratio"), and σ is the mass extinction coefficient. *Vaughan et al.* (2005) state in the CALIOP Level 1 algorithm theoretical basis document (ATBD) that S is an empirical parameter ranging between 40–60 sr^{-1} for smoke plumes, depending on age, and $\sim$ 70 sr^{-1} for volcanic sulfate. The lidar observation (Figure 4.1) used for determining aerosol mass is within 48 hours of the plume injection, and was shown in *Peterson et al.* (2018) to be mostly free of clouds and ice. With this assumption of a smoke-only plume, all computations presented herein utilize $S = 60$ sr^{-1} and a single scatter albedo $\omega_0 = 0.9$, which are appropriate for aging boreal fire plumes (*Reid et al.*, 2005). For this case, a range of σ between 3.0–6.0 m^2 g^{-1} (*Nikonovas et al.*, 2017) is used for the final M_ρ estimate.

To estimate V (= plume area $\times$ thickness), each component are determined individually from different instruments. Stratospheric area is determined by computing the area subtended by all OMPS pixels containing UVAI values above the threshold, and thickness is determined from the depth of stratospheric component of the plume in concurrent CALIOP lidar profiles. A UVAI threshold = 15 has been shown to be an accurate cutoff for stratospheric pyroCb plumes (*Fromm et al.*, 2008b), and is used here. Using this cutoff produces a plume area approximately $8{\times}10^5$ km^2, and the lidar profiles resolved a plume between 1.0–2.0 km thick, giving a stratospheric $V \simeq 1.475{\times}10^{15}$ km^3. CALIOP β'_{532} are input into Equation 4.1,

and profiles of M_ρ are averaged, resulting in total mass estimate between 0.1–0.3 Tg.

Figure 1 from *Peterson et al.* (2018) shows how this value compares to the 2008 Kasatochi eruption and the large Chisholm pyroCb event. Kasatochi's 2008 eruption is considered a moderate volcanic event with a Volcanic Explosivity Index (VEI) of 4, and had an estimated initial aerosol mass between 0.2–0.5 Tg ignoring secondary particle formation. The Chisholm pyroCb was estimated to have a mass between 0.018–0.109 Tg (*Fromm et al.*, 2008b), depending on the choice of optical properties and using an UVAI threshold = 15.

The first reliable CALIOP overpass of the PNE plume occurred on 14 August 2017 at approximately 11:30 UTC, and is shown in Figure 4.1. Previous overpasses on 12 and 13 August had ambiguous β'_{532} and δ_{532} properties that reduced confidence in the pyroCb source attribution. The majority of the plume is situated between 12 and 13 km in altitude with strong backscatter and full attenuation of the lidar. The overlaid, open boxes show the simultaneous MLS CO retrievals (similar to the water vapor anomalies shown in Figures 2.15 and 2.16). The maximum CO value for this scene ($\sim$ 678 ppbv; white "×") occurs near the highest plume altitude near 70.5°N. Columns labeled "1" and "2" are used in the radiative transfer simulations detailed below. Because Figure 4.1 is a nighttime observation, the closest NPP overpass does not provide an OMPS UVAI; the leftmost panel in Figure 2.3d (14 August 19:12 UTC) is the best representation of a UVAI measurement corresponding to this CALIOP curtain.

Figure 4.2 shows columns 1 and 2 from Figure 4.1 in terms of their average

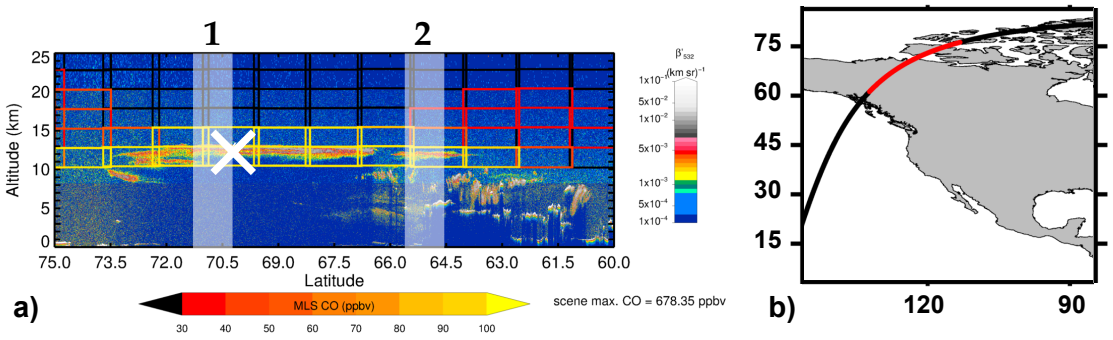

Figure 4.1: The first reliable CALIOP β'_{532} intersection with PNE stratospheric plume on 14 August (∼1.5 days after injection) at 11:30 UTC. Overlaid are MLS observations of CO. Maximum CO mixing ratio observation is > 670 ppmv (white "×" near 70.5 °N). Columns of light vertical shading labeled 1 and 2 are locations used to assess total aerosol extinction for comparison with OMPS UVAI (see Figures 4.2 and 4.3).

scattering ratio, and the determined particle extinction profiles. The vertically-dependent threshold recommended by the official CALIOP "feature finding algorithm" (*Winker et al.*, 2009) is shown as the discontinuous blue line in (a, c). The scattering ratios (green line) greater than this threshold are considered "features" (i.e., non-molecular), and are used to determine particle extinction profiles (b, d) and stratospheric AOD using the following steps: i) aerosol feature layers are identified using the scattering ratio threshold, ii) β'_{532} values within the identified layers are multiplied by S to estimate particle-only optical extinction coefficients, and iii) vertical integration of these coefficients in the stratosphere determines stratospheric AOD. For this case the tropopause as determined by the nearby 12:00 UTC Norman

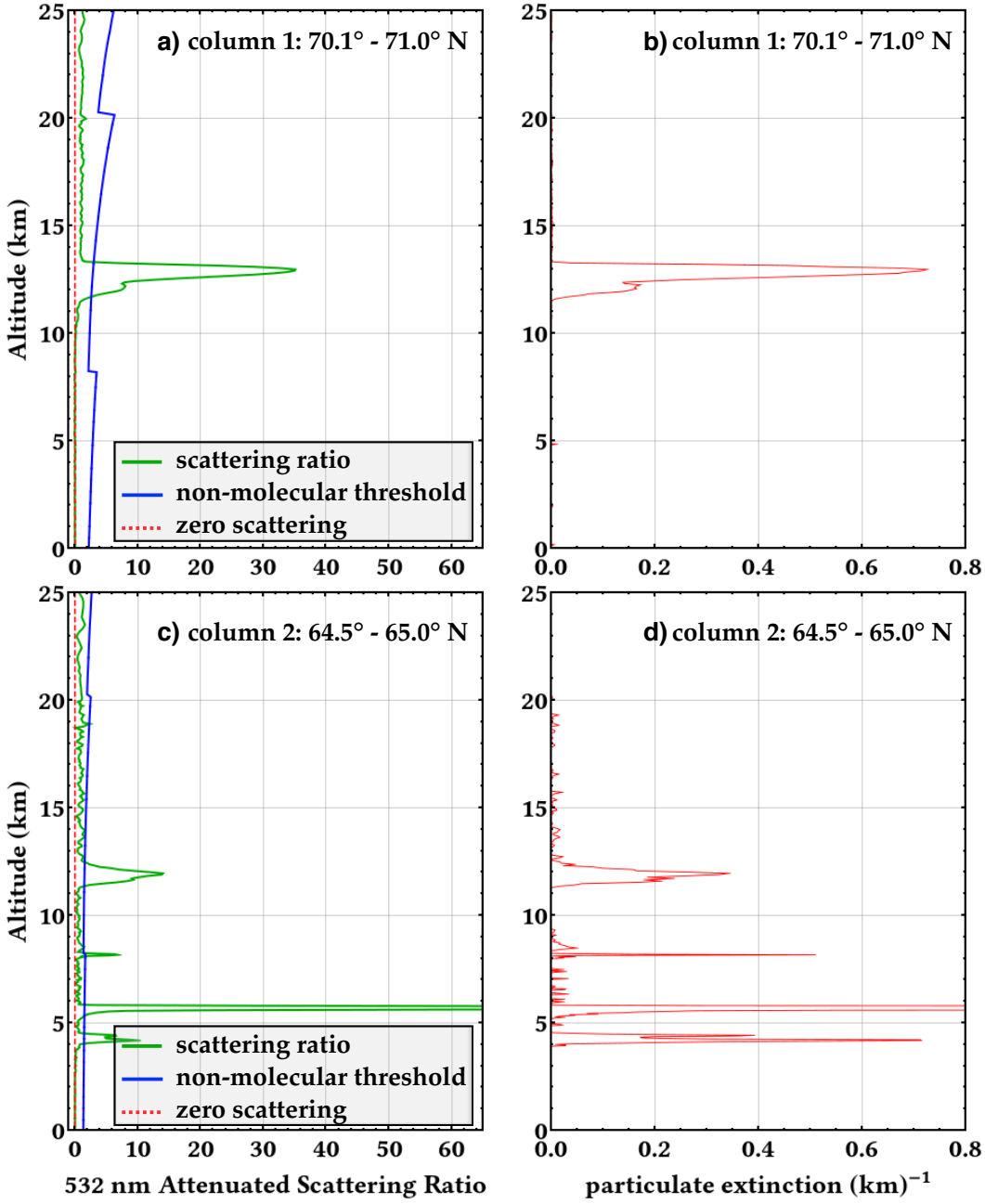

Figure 4.2: Profiles of scattering ratio (left) and derived non-molecular extinction (aerosol particulates, right) from the PNE plume intersection in Figure 4.1. (a, b) correspond with column 1 and (c, d) with column 2. Vertical integration of plume extinction for tropopause height >11.5 km yields AOD $\simeq$ 3.5 and $\simeq$ 1.5, respectively.

Wells radiosonde is 11.5 km, which is approximately $\theta \simeq 370$ K. This agrees with the initial injection potential temperature determined from surface weather radar at Prince George, British Columbia (discussed in the next section).

Radiative transfer simulations using the Santa Barbara DISORT Radiative Transfer (SBDART; *Ricchiazzi et al.*, 1998) model are used to give confidence in the mass estimation algorithm. The validity of UVAI threshold (= 15) is tested with two channel ultraviolet simulations ($\lambda = 330$ and 390 nm) using the CALIOP stratospheric extinction profiles shown in Figure 4.2. Figure 4.3 shows the stratospheric AOD (a) and simulated UVAI from SBDART (b) along the CALIOP orbit track (red orbit segment on Figure 4.1b). According to the CALIOP ATBD, the lidar typically is fully attenuated by optical thicknesses > 3, denoted by the red line across Figure 4.3a. There is a large section of the plume that is consistently at or above this value between 66–73°N and is at an altitude high enough to create an UVAI greater than the 15 threshold (red line on panel (b)).

Comparing this independent UVAI estimation with OMPS shows that the known stratospheric components of the plume (as determined with CALIOP) are well thresholded using UVAI = 15. In other words, computing the area of the plume using this threshold does indeed subset the UVAI field into a stratospheric-only component. Therefore, stratospheric mass estimates for this pyroCb plume using this methodology are more likely to be an underestimate than an overestimate because the lidar is fully attenuated along thicker sections of the plume and result in an underestimate of plume depth.

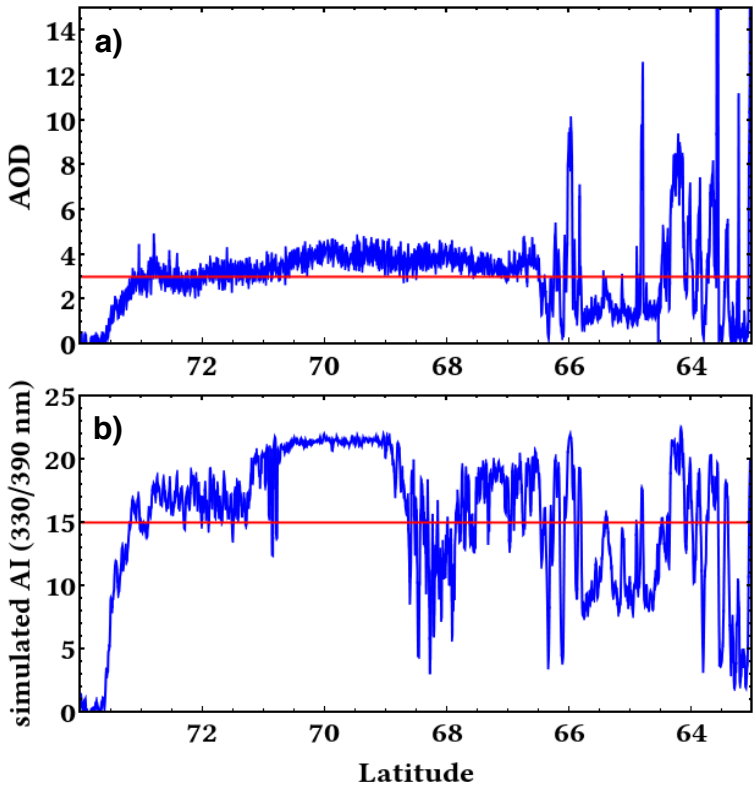

Figure 4.3: Empirical results of mass estimation of the PNE plume shown in Figures 4.1 and 4.2 showing the a) along-track AOD derivation and b) simulated UVAI using the 330 nm and 390 nm channels. Red lines show a) the value of "total optical attenuation" of the downward-looking vertical CALIOP instrument (note a majority of the plume between 66-73 °N has fully attenuated the lidar) and b) stratospheric UVAI threshold. There is good agreement with the plume's simulated UVAI ≥ 15 and the stratospheric component of the CALIOP observation in 4.1.

4.2 Plume Rise Observations and Simulations

4.2.1 Satellite Observations

This section details the dramatic diabatic rise of the 2017 PNE plume by combining satellite observations with radiative transfer modeling. The plume is tracked for several months after the 12 August pyroCbs occurred using dual MLS thresholds of concurrent H_2O and CO, and confirmed with CALIOP extinction observations. Figure 4.4 shows the plume on 3 September about three weeks after the pyroCbs injected it. The white dashed line is the maximum injection height observed on 12 August at $\sim$ 11.5 km. The white "$\times$" once again shows the location of the maximum MLS CO for this particular scene ($\sim$ 170 ppbv), and at this time is around $z = 22$ km where CALIOP β'_{532} confirms the plume's presence. Computing a velocity from this observation and the injection height on 12 August puts the average rate of rise over the first three weeks at roughly 400 m day^{-1}, an extraordinary rate never-before observed with a pyroCb plume.

Anomalously large stratospheric mixing ratios of both H_2O and CO are a defining characteristic of this event, and the reliable, global observations of Aura MLS make tracking this plume straightforward. This instrument is used to perform a plume-tracking analysis (as opposed to analyzing spatiotemporal averages of MLS species) for the following two reasons. First, the best way to track stratospheric aerosol would be with the high-resolution CALIOP lidar. Other instruments such as limb-profilers would work, but CALIOP has reasonably good spatiotemporal cover-

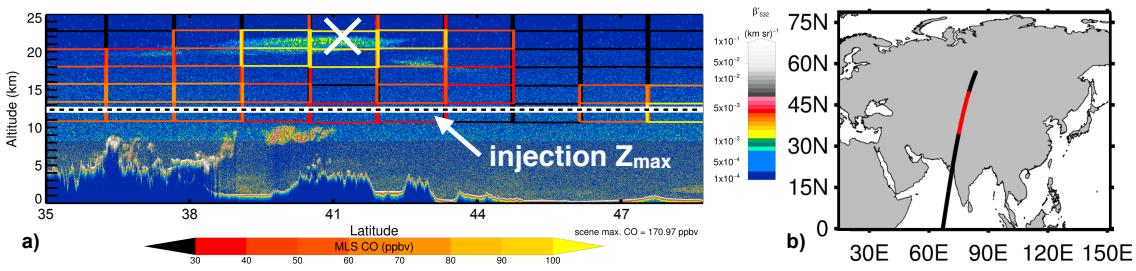

Figure 4.4: CALIOP/MLS observation of the PNE plume on 3 September 2017 at 21:00 UTC ($\sim$ 3 weeks post-injection). Location of CO maximum ($\sim$ 170 ppbv) and large β'$_{532}$ values show plume has risen at least 10 km above the injection height (white dashed line).

age, and has high vertical and horizontal resolution unmatched by solar occultation or limb-scatter instruments for stratospheric aerosol (*Fromm et al.*, 2014). However, CALIOP suffered a $>$ 1 week data gap during the month of September 2017, and connecting observations with HYSPLIT trajectories (as was done in Chapter 2) is problematic over such a long time without observations to validate them. Also, HYSPLIT does not account for diabatic heating of plumes, so forecasting a track position can lead to significant errors when self-lofting may be involved. The continuous monitoring by MLS alleviates this problem. Second, a goal of this research is to estimate the radiative forcing impact of stratospheric pyroCb plumes, and water vapor anomalies need to be quantified in order to accomplish this goal (see Chapter 1). Thus, in addition being the primary tracking method of the plume, MLS observations are used to suss out individual species anomalies and estimate a "real-time" radiative forcing of the plume (Chapter 5).

To track the plume, a dual threshold of MLS $H_2O \geq 7$ ppmv with a concurrent CO ≥ 70 ppbv is applied to all MLS observations at isentropic levels $600 \geq \theta \geq 380$ K. After 25 September the CO threshold is lowered to 40 ppbv, and after 10 October it is lowered to 30 ppbv. On 19 November both thresholds are lowered: $H_2O \geq 6$ ppmv and CO ≥ 20 ppbv. Because MLS retrieves species mixing ratios on pressure surfaces, the Level 2 Temperature product is used to compute θ. Figure 4.5 shows four time steps in this tracking process. Panel (a) starts one month post-event on 12 September, at which time a large section of the pyroCb plume (shown in Figure 4.4) separated into three distinct and trackable sections over central Asia. From this point onward in the study—including Chapter 5—these three sections are referred to as the "Triangle," "Circle," and "Square" plumes for convenience and ease of identification. The trajectory shown in Figure 4.5a is an approximation of the actual path the plume took over the course of one month post-stratospheric injection. It was tracked during this time using the MLS threshold mentioned herein, but the individual dates between 12 August–12 September are omitted for space. Note that typical zonal mean wind velocity in the LS at these latitudes is ~ 15 m s^{-1} (*Wallace*, 2003), which agrees with the observed wind velocity ~ 16 m s^{-1}.

In Figure 4.5b–d, these three sections are tracked by connecting the MLS observations of points that exceed the dual threshold criteria (green trajectory; Triangle plume, blue; Circle plume, and red; Square plume). The colored dots on the maps are locations where MLS observations exceed the dual thresholds. These dots are colored according to their altitude as determined with the geopotential height (GPH) product. The last observable day of each plume is shown in the

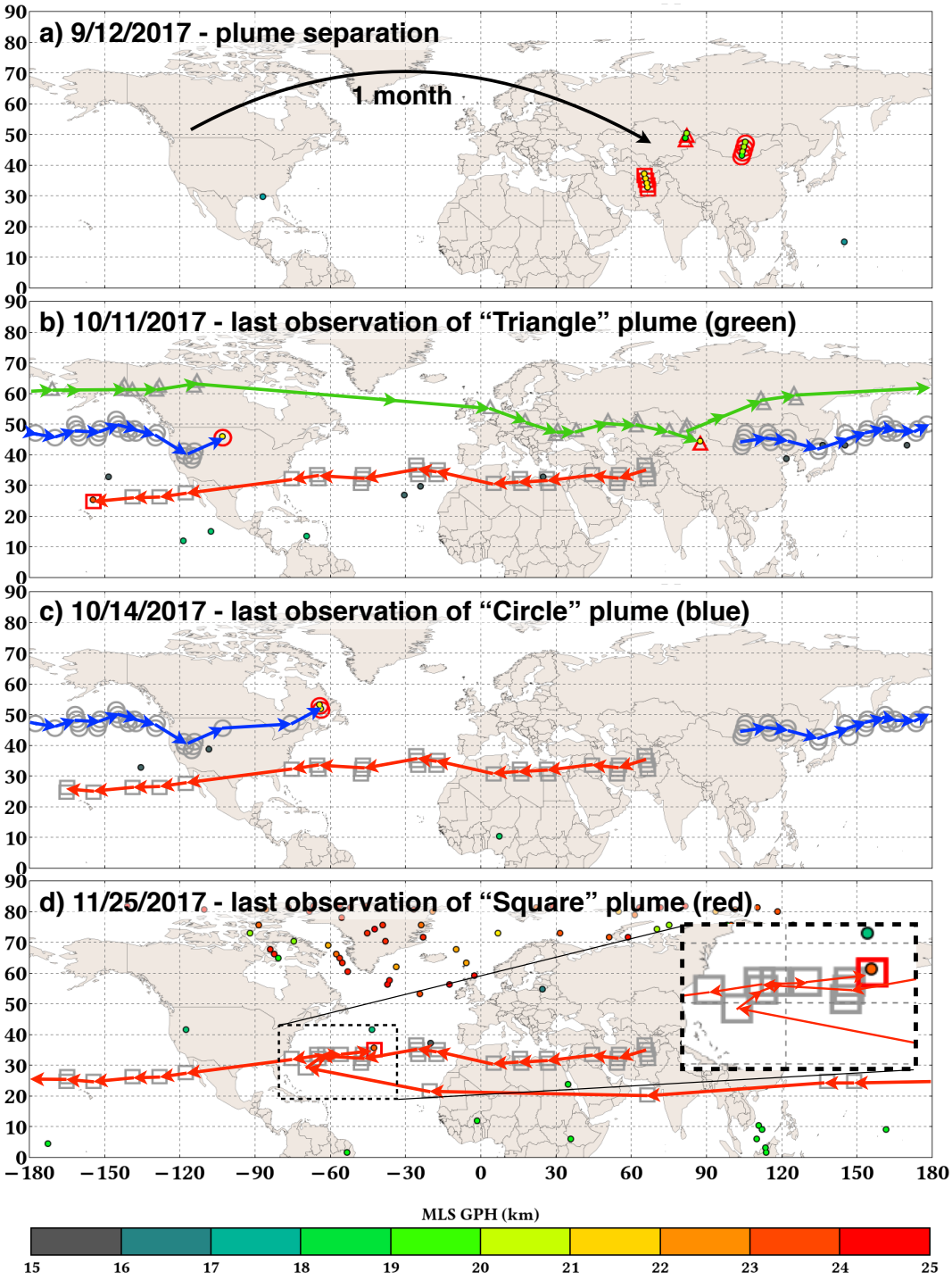

Figure 4.5: Hand-drawn trajectories of three sections of the 2017 PNE plume tracked using the dual MLS H_2O/CO threshold. (Continued on next page)

Figure 4.5: (continued) Panel (a) shows the start date (12 September) when the plume could be sufficiently identified as three independently moving sections. The "1 Month" trajectory between the 12 August pyroCb date and the plume locations on 12 September is an approximation based on the plume tracking method described in the text. Panels (b–d) show termination dates of each plume section's observability. Colored dots are the GPH of the MLS plume observation (bottom colorbar). Inset in panel (d) focuses on the area over the mid-Atlantic where the Square plume completed a circumnavigation; locations are marked when observations occurred between 29 September and 2 October (bearing east toward west) and 11–25 November (bearing from southeast toward northwest, then abruptly shifting toward northeast).

bottom panels; (b) Triangle, (c) Circle, and (d) Square. Note that panel (a) shows the start of the trajectories in (b–d). MLS and CALIOP were also used prior to 12 September, but in the interest of space, they are left off this figure. However data from those dates are included in the self-lofting analysis below. Each of these plume sections circumnavigated the globe at least once, and the Square plume was actually lofted high enough in the tropical lower stratosphere to encounter the Easterlies, and shifted course back toward the west prior to circling the globe.

Figure 4.6 combines all MLS dual threshold observations from the northern hemisphere (NH) between 12 August and 18 November, and displays them at their θ level. The vertical dashed line is the 12 September plume separation date (Fig-

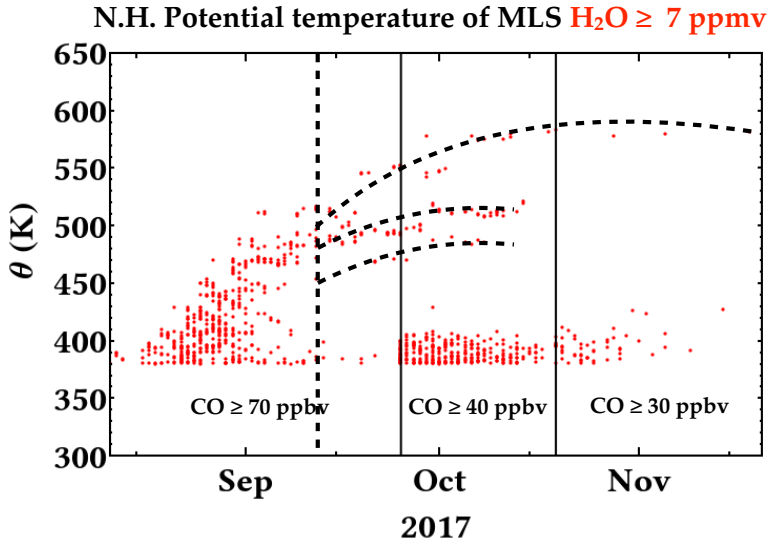

Figure 4.6: Potential temperatures of all northern hemisphere MLS thresholded observations during the first three months of the PNE plume evolution. A constant H_2O threshold of 7 ppmv is applied with diminishing CO thresholds as the plume ages. The vertical dashed line marks the point at which the plume separates over central Asia, and the three dashed lines emanating from this time show the different ascent rates of three tracked plume sections.

ure 4.5a), and the three dashed lines emanating from this date represent from top-to-bottom the approximated diabatic rise of the Square, Circle, and Triangle plume sections, respectively. The apparent diabatic increase is greater than 200 K for this H_2O/CO thresholds, and from these observations it is apparent that the rate of plume rise is greater in the early stages of the plume lifetime (before 12 September). This is most likely due to aerosol diffusion as the plume ages, which would reduce radiative heating throughout the solar daytime.

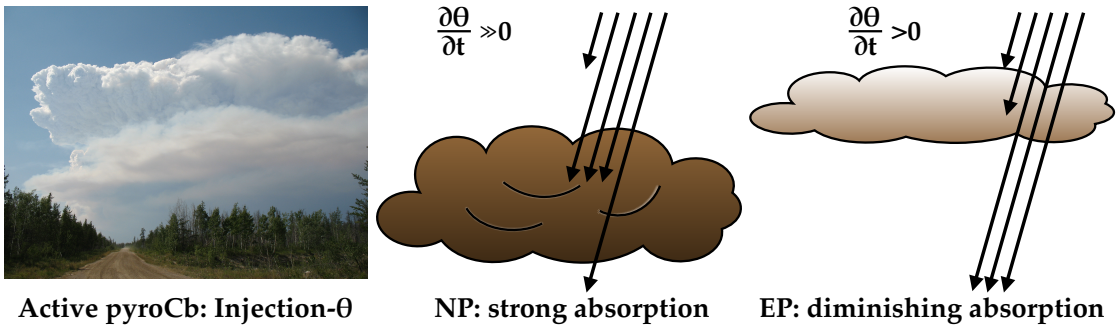

Figure 4.7: Illustration of pyroCb smoke plume evolution from onset through decay. Left: available observations are used to define the injection-θ at a specific location and time. Middle: the NP-phase is when the earliest-possible 3D observations of the plume can be characterized, and coincides with strong diabatic-lofting potential due to high concentrations of absorbing aerosol. Right: the EP-phase is the period during which advection and dispersion are reducing the concentration of aerosol to the point of non-observability, and diabatic-lofting potential is rapidly diminishing.

A schematic of this process is shown in Figure 4.7, where the early stages of plume life are denoted as the "nascent plume" (NP) and the latter stages as the "evolving plume" (EP). Black arrows represent incoming solar irradiance, which is more greatly absorbed during the NP stage than in the EP stage. The next section will mathematically demonstrate this concept and use SBDART to model the radiatively-forced plume rise.

4.2.2 Modeling Plume Rise

To simulate the lofting observed in the MLS and CALIOP observations, SBDART is used to calculate longwave and shortwave radiative heating rates using the stratospheric extinction profiles. This analysis focuses on the Square section of the 2017 PNE plume, but two additional cases are analyzed for comparison: 1) the much smaller August 2014 GSL pyroCb, and 2) the February 2009 Australian Black Saturday pyroCb event. Extinction coefficients at 532 nm are derived from CALIOP β'_{532} and $S = 60$ sr^{-1}, and plume optical depth is calculated using vertical integration for heights where $\theta > 380$ K. SBDART is set up to calculate full-spectrum irradiance using these optical depths and plume density profiles, using $\omega_0 = 0.9$, and mie scattering asymmetry parameter = 0.7. The model atmosphere provided with CALIOP data (derived from NASA's GEOS-5) is used for temperature, humidity and upper stratospheric O_3 profiles (*Winker et al.*, 2009). To calculate the diabatic heating anomaly, model runs are performed for the same atmospheres at each observation except with clear skies, and the resulting profiles are subtracted from the aerosol results.

In simple terms, each CALIOP observation is used as an independent data point in a time series of plume heating anomalies. These heating rate anomalies are assumed to proportionally increase the temperature of the plume, are thus are accrued to the initial UTLS-injection potential temperature (θ_0) to estimate the rate of diabatic-rise. At each observation, the modeled difference between the clear sky and the plume heating rate profiles yields the aerosol-only heating rate anomaly,

so the diabatic rise at the i^{th} model time step is then estimated by accumulating all these anomalous values (units of K day^{-1}) from the 0^{th} through the $(i-1)^{\text{th}}$ time step.

The total change in plume potential temperature can be represented by the thermodynamic energy equation:

$$\frac{D\theta}{Dt} = \varepsilon(Q - \frac{g_0}{c_p}w). \tag{4.2}$$

Here, the coefficient ε is defined as the efficiency that the sum of internal heating and work has on affecting θ changes within the plume, Q is the radiative heating rate, which is simply

$$Q = -\frac{1}{\rho c_p}\frac{d}{dz}(\mathrm{F}^{\text{net}}), \tag{4.3}$$

g_0 is the acceleration due to gravity, c_p is the specific heat at constant pressure, ρ is the air density, F^{net} is the net flux as defined in Chapter 1, and w is the isothermal vertical velocity.

An appropriate scale assumption is that w is time-independent because of the highly stratified environment of the LS. It is possible that for long duration events the Brewer-Dobson uplift in the lower stratosphere could play a small roll in the diabatic rise of plumes. However, the time-scale for plume duration would need to be measured in years because observations have shown Brewer-Dobson velocities at these altitudes are approximately 0.02–0.03 cm s^{-1} (17–25 m day^{-1}), which means a parcel would gain 1 km in altitude about every two months (*Minschwaner et al.*, 2016). For all documented pyroCb aerosol lifetimes this time scale is too long, and w can be ignored as a term that would do work on the system. Therefore, Equation 4.2

can be reduced to

$$\Delta\theta = \varepsilon \Delta Q \Delta t, \tag{4.4}$$

and the simulated potential temperature at the i^{th} observation step of the plume can be written as

$$\theta_{\varepsilon,i} = \varepsilon \sum_{i=1}^{N} (n\Delta Q_{i-1} + \theta_{i-1}), \tag{4.5}$$

where n is the number of lapsed days between the i^{th} and $(i-1)^{\text{th}}$ CALIOP extinction observations and N is the total number of observations. Because ε is assumed to be time-independent due to the nature of stratospheric stability, the approximated physical processes contained within ε include small impact quantities such as diffusion, turbulence, latent heating, etc; processes that are on long times scales in the LS. It also provides a simple way to bundle the errors in the optical property assumptions, SBDART physics, CALIOP extinction estimations, etc.

The plume-rise model defined by Equation 4.5 is a simplification of the nature of LS dynamics, but with the understanding that ε is an empirical parameter to be used as a test against observed rates of plume-rise. This model is applied to observations made during the 2017 PNE Square plume (Figure 4.8), the 2014 GSL pyroCb plume (Figure 4.9) and the 2009 Black Saturday plume (Figure 4.10), and the data from these cases are tabulated in Tables 4.1–4.3, respectively.

The radiative heating anomaly (ΔQ) is computed from SBDART by taking the difference between the heating of the aerosol layer and a clear sky with the same temperature and humidity profiles. Aerosol layer boundaries used in the SBDART profile inputs are determined from the CALIOP extinction profiles used to retrieve

stratospheric aerosol optical depth.

Potential temperature levels of each CALIOP plume extinction observation (at which ΔQ_i is computed) are not considered when calculating $\theta_{\varepsilon,i}$ (the plume's heat accumulation summation). These observations are only used as input into the SBDART model that produces heating rate profiles. In other words, this model time series is "independent" in that there is no attempt to correct a prognosticated $\theta_{\varepsilon,i}$ with observations of plume θ. The empirical ε is the only parameter by which the model results are "corrected" to match observations. A range of ε values have been applied, and $\varepsilon = 100\%, 50\%, 30\%$ are shown in Figures 4.8–4.10, with the additional $\varepsilon = 10\%$ shown in Tables 4.1–4.3.

Figure 4.8 shows observed and modeled diabatic plume rise of the Square plume section of the PNE case (see red trajectory in Figure 4.5). This is the highest, and most optically thick section of the PNE plume that is trackable. It also moves south into the tropics (≤ 30 °N), and slowly moves westward in this region for about one month between early October and early November.

In Figure 4.8a, CALIOP β'_{532} is used to determine the θ centroid at each observation, and is shown as a blue "×". Blue lines extending from each CALIOP "×" denote the range of plume thickness. Light blue bars during the month of September are periods of CALIOP data gaps. Also, replotted here (as in Figure 4.6) are all NH MLS measurements greater than the dual H_2O/CO threshold (green "○") to provide information during these CALIOP data gaps. Corresponding plume AOD is shown in (b). The pyroCb injection $\theta = 370$ K is shown on the plot, and is determined from the highest surface weather radar echo top altitude from the

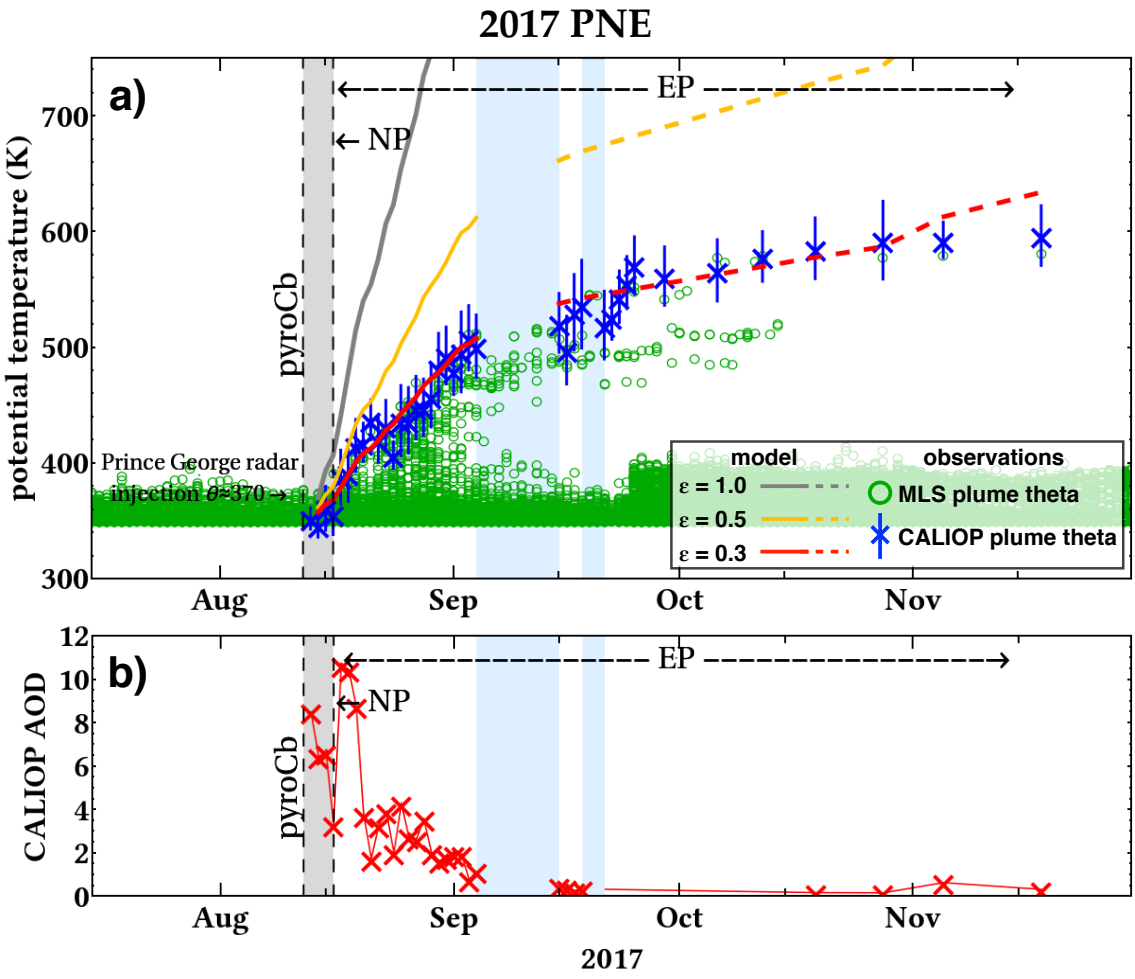

Figure 4.8: (a) Observed and modeled diabatic rise of the PNE Square plume (see red trajectory in Figure 4.5). Blue "×" show the potential temperature of the CALIOP-observed plume centroid with error bars denoting the upper and lower backscatter boundaries, augmented with MLS plume observations of colocated HCN/CO maxima (green dots). Simulation of radiatively-forced diabatic lofting for various ε are shown over observations. Prince George radar echotop-based injection $\theta = 370$ K is noted. (b) The stratospheric AOD derived from CALIOP extinction.

Table 4.1: 2017 PNE pyroCb plume potential temperature observations (θ) and model-predicted (θ_ε) using various efficiency parameters (ε). Also shown are CALIOP stratospheric AOD and SBDART radiative heating rate anomalies (ΔQ) in K day^{-1}. $n\Delta Q$ is the maximum temperature change assuming a steady state over n days between observations (K; only shown where $n > 1$, otherwise $\Delta Q = n\Delta Q$). Last row gives total change in θ and each θ_ε. θ_ε values in bold are closest match to plume θ.

date	plume θ	AOD	ΔQ ($n\Delta Q$)	$\theta_{\varepsilon=100\%}$	$\theta_{\varepsilon=50\%}$	$\theta_{\varepsilon=30\%}$	$\theta_{\varepsilon=10\%}$
08/13	352	8.51	18.30	–	–	–	–
08/14	347	6.46	22.95	371	361	358	**354**
08/15	361	6.62	13.02	394	372	**365**	356
08/16	357	3.34	33.79	407	379	369	**358**
08/17	388	10.65	37.62	440	**396**	379	361
08/18	392	10.47	36.84	478	415	**390**	365
08/19	415	8.76	25.55	515	434	**401**	369
08/20	418	3.76	13.76	540	446	**409**	371
08/21	438	1.75	22.64	554	**453**	413	372
08/22	420	3.28	30.31	577	465	**419**	375
08/23	432	3.91	16.35	607	480	**429**	378
08/24	407	2.01	30.85	623	488	**434**	379
08/25	437	4.25	23.88	654	503	**443**	383
08/26	437	2.74	23.38	678	515	**450**	385
08/27	448	2.65	33.07	702	527	**457**	387
08/28	448	3.56	19.79	735	543	**467**	391
08/29	458	2.03	18.34	754	553	**473**	393
08/30	482	1.64	22.67	773	563	**478**	394
08/31	493	1.82	27.23	795	574	**485**	397
09/01	480	1.93	23.28	823	587	**493**	399
09/02	496	1.96	9.47	846	599	**500**	402
09/03	508	0.78	16.55	855	604	**503**	403
09/04	501	1.18	9.02 (99.23)	872	612	**508**	404
09/15	521	0.49	5.51	971	662	**538**	414
09/16	498	0.40	4.65	977	665	**540**	415
09/17	530	0.28	5.39	981	667	**541**	415
09/18	538	0.35	3.80 (117.92)	987	670	**543**	416
10/19	586	0.18	3.39 (30.52)	1105	728	**578**	428
10/28	593	0.17	10.76 (86.06)	1135	744	**587**	431
11/05	593	0.64	5.44 (70.77)	1221	787	**613**	439
11/18	596	0.33	–	1292	822	**634**	446
$\Delta\theta$	244	–	–	940	470	**282**	94

Environment Canada WSR-98R site at Prince George.

Also shown in Figure 4.8a are the model-simulated plume rise using three different ε values (red; 30%, yellow; 50%, gray; 100%). Solid lines represent the time prior to the CALIOP data gap, after which interpolation is used to estimate extinction for input into SBDART. Before this gap, there is a fairly linear and consistent rise seen in the observations, and computed by each model estimate. $\varepsilon = 0.3$ gives the best agreement, matching both the θ and $\Delta\theta$ almost exactly. This time period (mid-August–early-September) is a relatively early part of the plume's life when extinctions were large, as shown where stratospheric AOD > 1.0 (b). After the gaps, CALIOP shows a slower ascent, and the $\varepsilon = 0.3$ modeled uplift is still in agreement. The earliest four days show very little diabatic rise (12–16 August; gray bar), and are denoted as the NP time period (See Figure 4.7), and the days that follow are labeled as the EP as the plume begins to undergo strong ascent.

Table 4.1 lists the observed plume θ and AOD, and the model heating rates and predicted plume θ_ε at each time step. There are several days early in the plume's lifetime where $\varepsilon = 50\%$ or 30% yield a closer match to observations, but on the whole $\varepsilon = 30\%$ has better agreement. The last line in Table 4.1 shows the net change in the plume potential temperature and the net change in each ε-value prediction. $\theta_{\varepsilon=30\%}$ is the closest match of the choices here, but still has a net difference = 38 K. However, the observation on 5 November had a jump in AOD from 0.17 to 0.64 that may be causing an overestimation of heat accumulation on that day. Ignoring the last two observations would reduce this disagreement $(244 - (587 - 352))$ K = 9 K for $\varepsilon = 30\%$. It is unknown why there is a jump in AOD during this last couple of

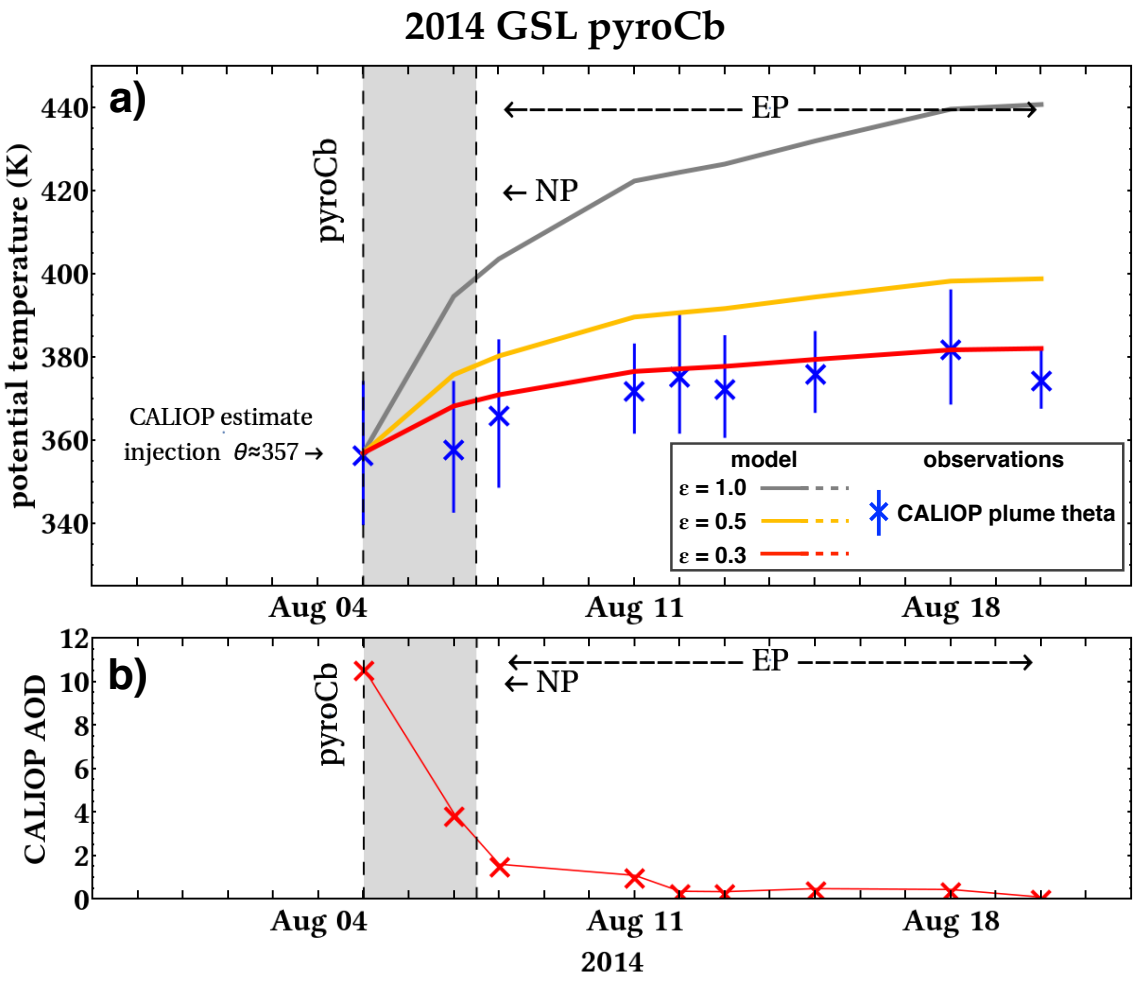

Figure 4.9: As in Figure 4.8, but for the GSL pyroCb plume. NP phase is shorter than the 2017 PNE case before stratospheric ascent is observed. Also, this plume was only trackable for approximately two weeks, and had a much smaller total $\Delta\theta$. Injected plume $\theta = 357$ K, averaged over depth of CALIOP observation is noted.

CALIOP observations. As shown in Figure 4.5d (inset) these AODs were calculated during a "recurve" in the plume's trajectory as it move back toward the northeast and out of the tropics. It is possible that the model atmosphere (from GEOS-5) has changed in a way that increases the extinction estimation from CALIOP profiles.

Table 4.2: As in Table 4.1, but for the 2014 GSL pyroCb plume.

date	plume θ	AOD	ΔQ ($n\Delta Q$)	$\theta_{\varepsilon=100\%}$	$\theta_{\varepsilon=50\%}$	$\theta_{\varepsilon=30\%}$	$\theta_{\varepsilon=10\%}$
08/05	357	10.61	19.45 (38.91)	–	–	–	–
08/07	359	3.94	9.36	384	371	365	**360**
08/08	367	1.61	6.50 (19.51)	403	380	**371**	362
08/11	373	1.10	2.19	412	384	**373**	362
08/12	376	0.37	2.07	418	387	**375**	363
08/13	373	0.35	2.90 (5.81)	420	388	**376**	363
08/15	377	0.49	2.67 (8.00)	422	389	**376**	363
08/18	383	0.44	0.59 (1.18)	425	391	**377**	364
08/20	375	0.10	–	427	392	**378**	364
$\Delta\theta$	18	–	–	70	35	**21**	7

The 2014 GSL and the 2009 Black Saturday Event pyroCb plumes are also analyzed with this observation/modeling framework (Figures 4.9, 4.10, respectively). Using the same values, $\varepsilon = 30\%$ appears to be the best approximation of the instrument-observed diabatic rise for these events as well, despite each event having a different scale and duration. Figure 4.9 shows that the GSL plume had fewer observations, and was only trackable for a little over two weeks. The NP stage lasted less than three days before significant plume rise was observed. Again, the AOD (b) was strong initially with values > 3 during the first two days, and then gradually reduced to < 1 after the third day. Table 4.2 shows the observed $\Delta\theta = 18$ K with a small overestimation by $\Delta\theta_{\varepsilon=30\%}$ of only 3 K.

Similar results are seen in the 2009 Black Saturday case (Figure 4.10). This case was similar to 2017 PNE in that there were several pyroCb plumes contributing to the total aerosol loading. An early AOD ~ 8 was observed by CALIOP during

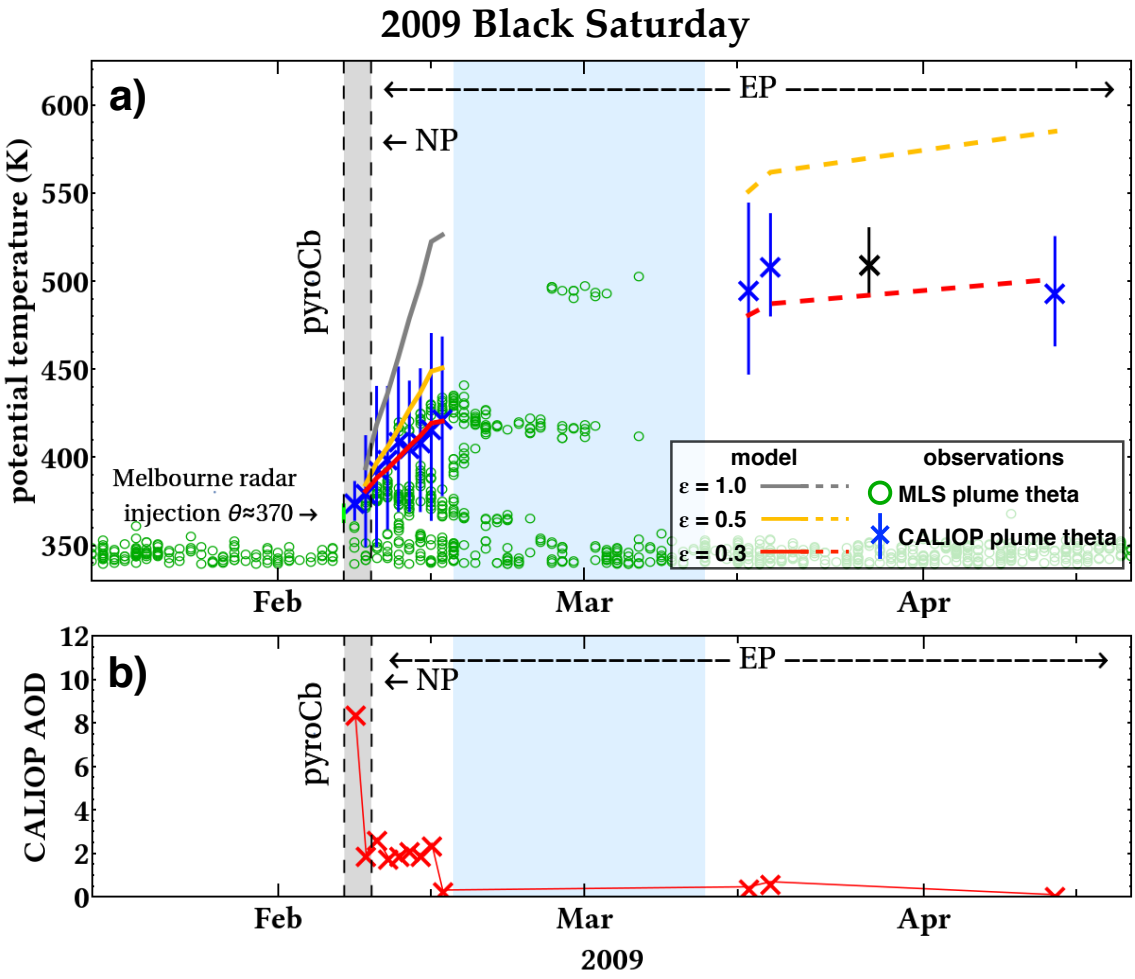

Figure 4.10: As in Figure 4.8, but for the 2009 Black Saturday pyroCb plume. Green "○" in this case are MLS observations colocated HCN/CO maxima to fill CALIOP gap (light blue vertical bar between mid-February to mid-March). Blue "×" are CALIOP observations, and black "×" is surface lidar observation from São José dos Campos, Brazil. Melbourne surface radar echotop-based $\theta = 370$ K is noted.

the NP (b). AOD dropped to ~ 2 within about 3 days, and was steady for about one week. During this week, the plume experienced a significant rise ($= 42$ K), and $\Delta\theta_{\varepsilon=30\%}$ applied over this time period yields 44 K, a minimal overestimation.

Table 4.3: As in Table 4.1, but for the 2009 Black Saturday pyroCb plume.

date	plume θ	AOD	ΔQ ($n\Delta Q$)	$\theta_{\varepsilon=100\%}$	$\theta_{\varepsilon=50\%}$	$\theta_{\varepsilon=30\%}$	$\theta_{\varepsilon=10\%}$
02/08	376	8.46	18.75	–	–	–	–
02/09	381	2.00	24.46	394	385	**381**	377
02/10	395	2.72	17.70	419	**397**	388	380
02/11	400	1.86	20.86	436	**406**	**394**	382
02/12	411	1.99	21.89	457	**416**	400	384
02/13	407	2.19	19.54	479	427	**407**	386
02/14	410	2.00	23.93	499	437	**412**	388
02/15	418	2.47	3.80	522	449	**420**	390
02/16	424	0.33	7.16 (200.46)	526	451	**421**	391
03/16	496	0.48	10.81 (21.62)	727	551	**481**	411
03/18	510	0.72	1.77 (46.45)	749	562	**487**	413
04/13	495	0.12	–	795	585	**501**	417
$\Delta\theta$	119	–	–	419	209	**125**	41

Unfortunately, after 15 February there was a prolonged data outage from CALIOP, and when data acquisition resumed in mid-March there was significant ambiguity in connecting the plume to the observations before the gap. This case did not have a significant MLS H_2O anomaly (discussed further in Chapter 5), so another biomass burning tracer HCN was thresholded with CO to document θ increases (green "$\circ$" in Figure 4.10a). When the model is reapplied to CALIOP observations after the data gap, $\Delta\theta_{\varepsilon=30\%}$ underestimates θ by about 15–20 K. At the end of CALIOP's trackable lifetime, however, the net difference is a small overestimation by 6 K (last line in Table 4.3).

The take home message from these cases is that pyroCb plumes, regardless of the scale and duration of the initial convective event, appear to have an empirical heat accumulation efficiency of 30%. Once again, this model is an oversimplification.

Potentially useful because of its simplicity, but it does not explicitly account for LS dynamics, and the effects that instrument retrievals and radiative transfer assumptions such as optical properties have on the heating. For example, the delineation between black and brown (organic) carbon contained within the aerosol plume is known to have a strong effect on the overall absorption and scattering properties of the plume. For the sake of simplicity and portability, these properties herein are assumed to be constant over the life of the plume in this empirical algorithm. Thus by design, this is an unrealistic accounting of the "efficiency" of smoke plumes to convert solar insolation to diabatic lofting, but has the benefit of computational efficiency and avoidance of non-confirmable assumptions about aerosol optical properties and local turbulence/diffusion. It must be stressed that this approach does not attempt to quantify the dynamic nature of evolving Mie-theory single scatter albedo or asymmetry parameter, only to account for the diminishing extinction coefficient as measured by CALIOP.

Additional pyroCb cases with observed diabatic rise are shown in Table 4.4 with citations. Up until now there has been very little focus on diabatic self-lofting after stratospheric injection. With the large scale 2017 PNE case, and the understanding that pyroCb are a seasonal occurrence, this work will be useful in the future as more evidence is gathered. The stratospheric aerosol mass estimation combined with a plume-rise modeling framework is a good first step in understanding the net impact that pyroCb have on climate through stratospheric processes. Another remaining question is the role of radiatively active gases within these plumes. As was shown in Chapters 2 and 3, the local WVMR contribution can be significant,

Table 4.4: PyroCb events with significant observational evidence of diabatic plume rise that have been published in peer-reviewed literature. Included are three additional cases not analyzed herein (all values of z in km and θ in K).

pyroCb event	z_0 (θ)	z_1 (θ)	$z_{\text{max.}}$ (θ)	duration (months)
Chisholm[1,2,3], 2001	14 (379)	12 (337)	18 (450)	3
Canberra[4], 2003	15 (367)	16 (385)	19 (450)	2
Great Divide[5], 2006	12 (340)	13 (343)	18 (425)	1-2
Black Saturday[6,7,8], 2009	15 (364)	16 (376)	22 (525)	4
GSL[9], 2014	14 (357)	14 (359)	15 (383)	0.5
PNE[10,11], 2017	14 (378)	14 (373)	24 (> 600)	> 6

1. *Rosenfeld et al.* (2007)
2. *Fromm et al.* (2008b)
3. *Fromm et al.* (2006)
4. *Dirksen et al.* (2009)
5. *Dirksen et al.* (2009)
6. *Siddaway and Petelina* (2011)
7. *Pumphrey et al.* (2011)
8. *Dowdy et al.* (2017)
9. *Kablick et al.* (2018)
10. *Khaykin et al.* (2018)
11. *Peterson et al.* (2018)

through both direct specific humidity enhancements and down stream sublimation of injected ice (Figure 2.18). The next chapter discusses the radiative impact of this process.

Chapter 5: Radiative Effects of Residual PyroCb-Injected UTLS Water Vapor

The global energy budget contains an average clear sky radiative forcing from water vapor of $RF = +71$ W m^{-2} (*Kiehl and Trenberth*, 1997). Compounding the climate issue of direct radiative forcing is the possibility of feedbacks from increased WVMR, thereby making the problem nonlinear. As discussed in Chapter 1, the sources of LS H_2O are thought to be mostly constrained, but recent studies have disagreements about the trends since the early 1980s. Quantifying the ability of deep convection, if any, to increase moisture in the UTLS under certain climate change scenarios is a problem that cannot be answered without understanding how deep convection itself would respond to climate forcing. The observationally-based water vapor feedback of +0.3 W m^{-2} as concluded by *Dessler et al.* (2013) was inferred from a correlation between the increase in observed stratospheric WVMR and an increase in tropospheric temperature, and was reproduced in a global chemistry-climate model. Their conclusion is a start to the conversation, but it cannot be considered axiomatic simply because of the disagreement on what the UTLS H_2O trend actually is; this conflicting data is assimilated by their model.

It is yet to be shown—or studied for that matter—what effect climate would

have on pyroCb frequency, seasonality, or intensity. To undertake such a study would require several decades (centuries, even) of pyroCb and fire data, and a complete understanding of the mechanics behind pyroconvection so that a detailed climate model could be parameterized to handle these events. Using the climate questions surrounding cloud-radiation and cloud-feedback as analogs to questions about pyroCbs, it seems likely that such a study would require several decades of research, dedicated observation platforms/campaigns and closure experiments.

On the other hand, the first-order question of "what effect do pyroCbs have on climate?" is one that can probably be answered with current instruments and models. The first things to investigate are the impact of stratospheric aerosol (discussed in Chapter 4), and other relevant climate forcing agents such as water vapor. The work contained in this chapter seeks to assess what the "real-time" water vapor forcing is of the 2017 PNE pyroCb plumes. Chapter 4 discussed the enhancements of H_2O in the context of tracking the plume, and this chapter will put these enhancements in context with a long-term global data record, compute the stratospheric WVMR *RF* using a highly-detailed radiative transfer model, and compare the sensitivity of this *RF* using two different techniques to determine the H_2O anomalies associated with this case.

5.1 Observed Water Vapor Enhancements

The WVMR impact of the 2017 PNE plume is put into better context when first analyzing statistics of all H_2O observations in the northern hemisphere. Fig-

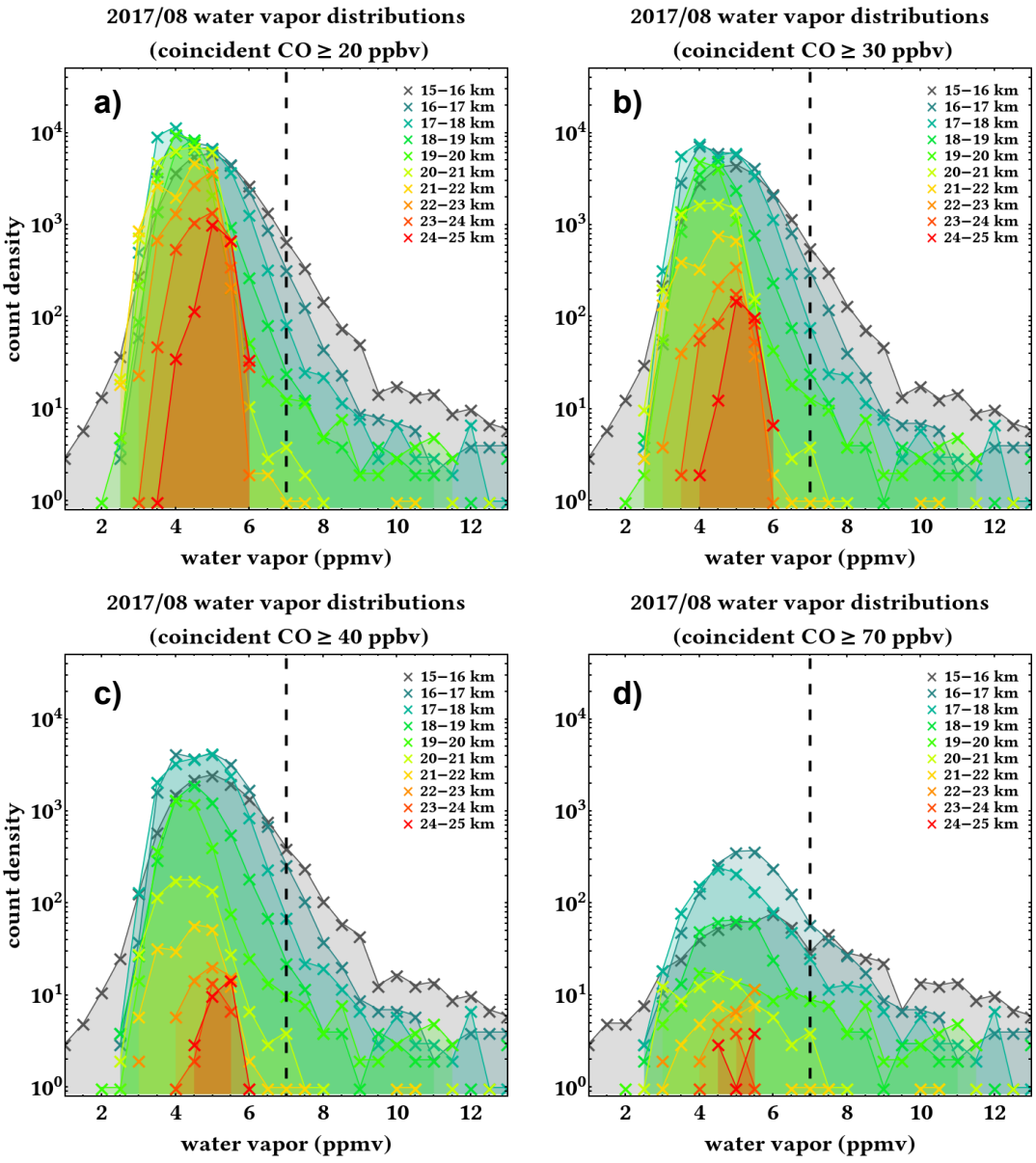

Figure 5.1: August 2017 histograms of all Aura MLS H_2O observations in the Northern Hemisphere lower stratosphere using coincident CO thresholds (a) $\geq$ 20 ppbv, (b) $\geq$ 30 ppbv, (c) $\geq$ 40 ppbv, (d) $\geq$ 70 ppbv. Count densities shown for each 1 km layer between GPH = 15–25 km for observations constrained by $380 \leq \theta \leq 600$ K.

(Continued on following page)

Figure 5.1: (continued) Note logarithmic scale. Observations to the left of 7 ppmv threshold (dashed line) were ignored for plume identification used in Chapter 4.

ures 5.1-5.4 show these statistics. MLS H_2O count densities are presented in 1 km altitude bins between 15–25 km for August through November 2017. In each Figure, panel a) shows WVMR distributions where coincident CO$\geq$ 20 ppbv, b) CO$\geq$ 30 ppbv, c) CO$\geq$ 40 ppbv, and d) CO$\geq$ 70 ppbv. The vertical dashed line is the 7 ppmv H_2O threshold used in tracking the plume throughout the observation period (see Figures 4.5 and 4.6).

In August, prior to the plume reaching above 20 km, there are relatively few H_2O observations at altitudes greater than this height for all coincident CO values. In fact, all H_2O observations at $z \geq 22$ km are ≤ 6 ppmv, even for low CO threshold, and the water vapor distributions in this part of the lower stratosphere consistently have a peak at $\sim$ 5 ppmv with an approximate range of $\pm$1 ppmv, irrespective of the coincident CO (see orange/red distributions in Figure 5.1). It appears that there is little correlation between H_2O/CO during the month of August in the northern hemisphere at these altitudes because the H_2O count densities are consistently centered at 5 ppmv in (a–d) even with absolute counts decreasing with greater CO mixing ratios.

This lack of correlation in August makes sense in general because the major sources of LS H_2O and CO are not correlated in the northern hemisphere at this time (*Filipiak et al.*, 2005). CO has a photochemical lifetime between 1–3 months

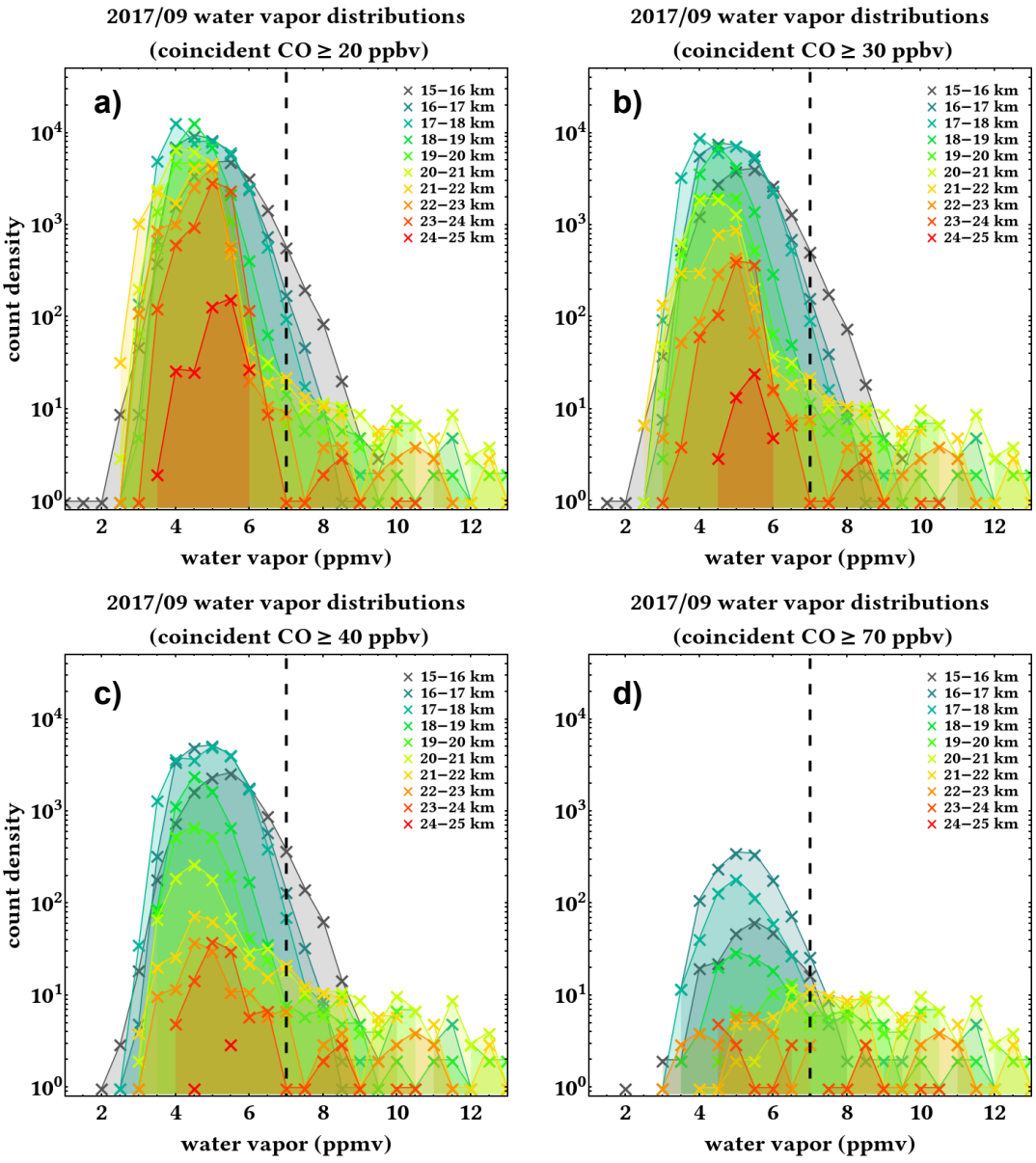

Figure 5.2: As in Figure 5.1 but for September 2017.

in the stratosphere, and approximately two months in the troposphere, so it can be a useful tracer of tropospheric air entering the stratosphere if the time scale of transport is shorter than these lifetimes; e.g., deep convection. Strong correlations between stratospheric CO and H_2O are typically only present within the polar vor-

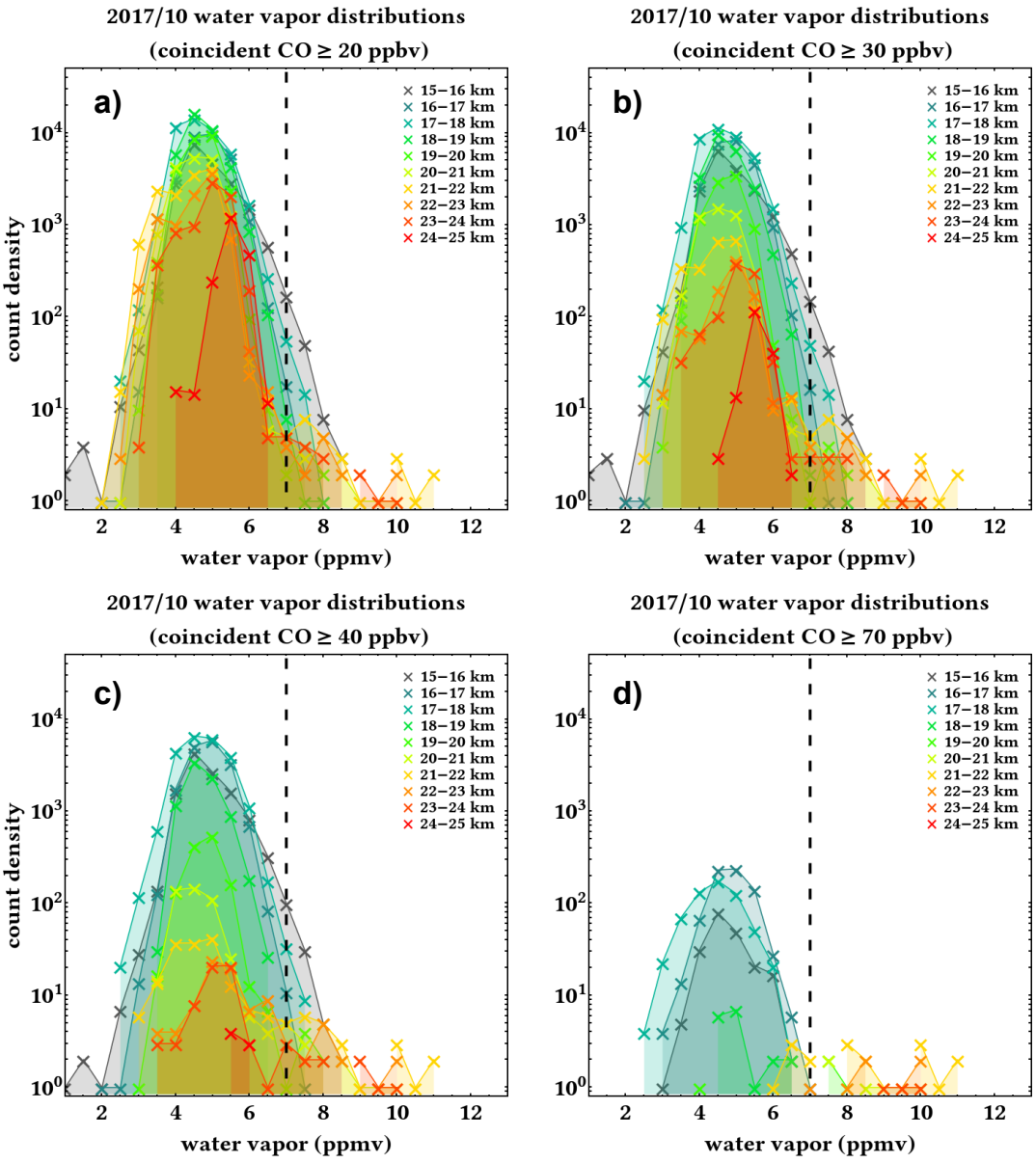

Figure 5.3: As in Figure 5.1 but for October 2017.

tex during the winter months when air is descending from the upper stratosphere and lower mesosphere. CH_4 oxidation is primarily responsible for H_2O production and photolytic chemistry of CO_2 in the thermosphere is the primary source of stratospheric CO. Other correlations, especially in the lower stratosphere tend to be

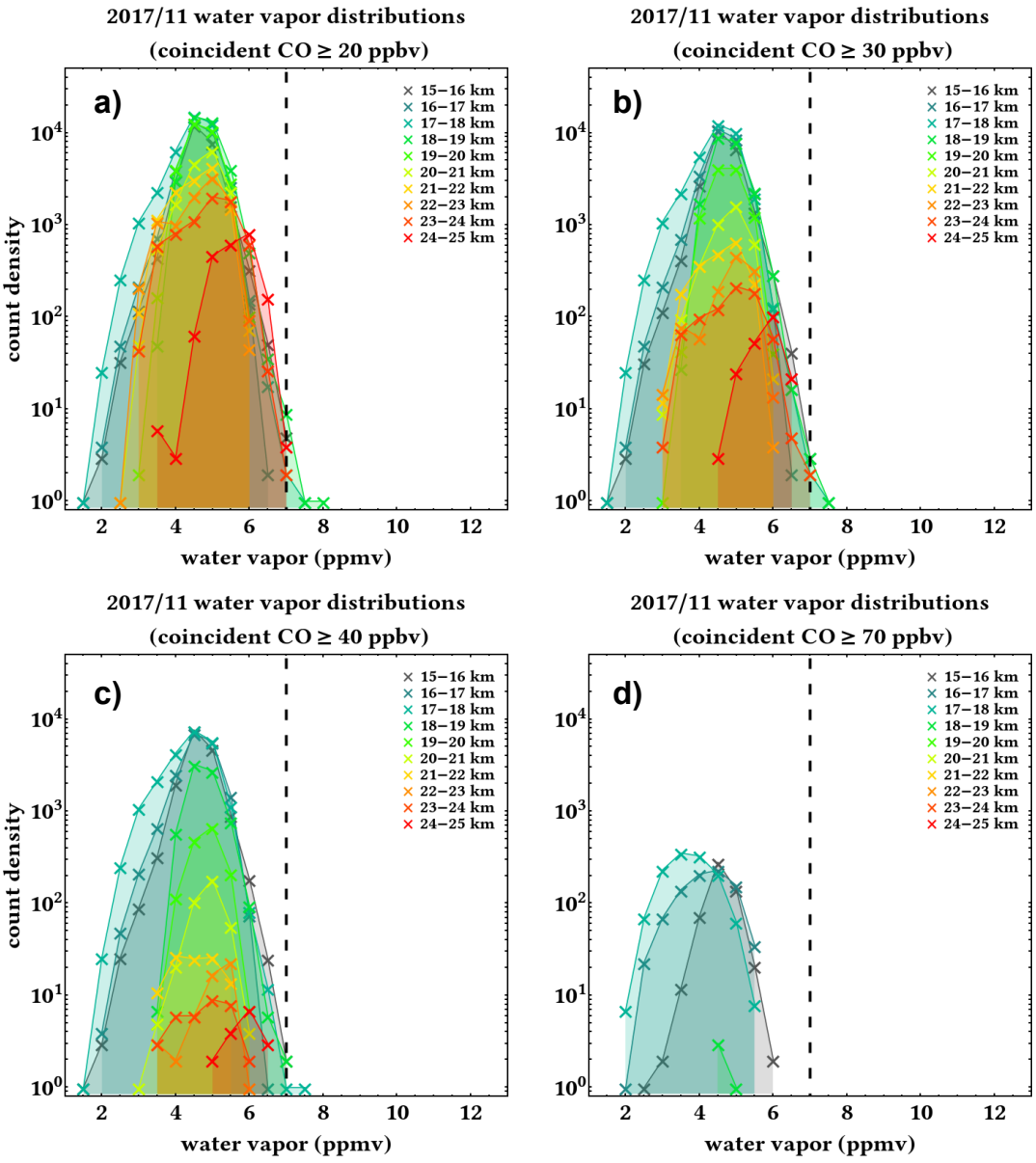

Figure 5.4: As in Figure 5.1 but for November 2017.

indicative of a tropospheric source (*Randel et al.*, 2010).

At $z \leq 19$ km, the concurrence of CO and H_2O is apparent in the distributions for August, when deep convection is strongest in the NH (gray, blue, light green distributions in Figure 5.1). The majority of the CO $\geq$ 70 ppbv H_2O counts occur

in the lower-most stratosphere (15–16 km), which is to be expected since there is a relatively large amount of continental and monsoon convection during that month. However, since most of these large CO mixing ratios are confined to the lower altitudes it does not appear that much, if any, tropospheric air intrudes into $z >\sim 20$ km, at least not on the time scale of 1–2 months when the convection is most active during July–August. During September–November, the concurrence is not as apparent at the altitudes between 15–20 km, but at higher altitudes the distributions indicate a stronger correlation. For example, in September when CO concentrations within the plume are still large, there are many more concurrent H_2O counts at $z > 22$ km (compare Figure 5.2d where water vapor ≥ 10 ppmv and CO ≥ 70 ppbv coexist at high altitude with Figure 5.1d where there are no concurrences).

In October (Figure 5.3), the count density distributions at lower altitudes become narrower as tropospheric sources from deep convection become less frequent, but there are still several observations of large H_2O/CO concentrations at $z > 22$ km. In November (Figure 5.4), all high-altitude observations of H_2O now have coincident CO concentrations < 70 ppbv. It is interesting to note that it appears the median value of H_2O has increased at by ~ 1 ppmv by this point. This is demonstrated when comparing the upper altitude distributions in Figure 5.1 to those in Figure 5.4. Median values of count density are centered around 5 ppmv in August, and have increased to 6 ppmv in November for the entire NH.

As shown in Chapter 4, even intense radiatively-induced self-lofting can be $\sim$ 1–2 km week^{-1} in the LS. So, diminishing CO concentration is to be expected

over this time period as the plume ages. On the other hand water vapor is longer lived, but undergoes the same fate as all concentrated plumes over time: dilution through diffusion. Using the plume tracking described in the previous chapter, the next section uses these H_2O enhancements to estimate changes to boundary fluxes, and stratospheric heating rates.

5.2 Line-by-Line Simulations

The Line-By-Line Radiative Transfer Model (LBLRTM, *Clough et al.*, 1992) is the framework used to estimate the longwave water vapor forcing associated with the 2017 PNE plume. This model was developed by Atmospheric and Environmental Research corporation, and uses the extremely detailed HITRAN 2016 database of line spectra for H_2O and about 50 additional species (*Gordon et al.*, 2017). The model and spectral database are freely available, and have both been validated several times over using both laboratory experiments, and long term atmospheric data records from the Department of Energy's Atmospheric Research Program site at the Southern Great Plains (*Clough et al.*, 2005).

The methodology of the forcing simulation experiments used herein is based on plume-centric H_2O anomalies. These anomalies are created by first constructing a spatiotemporal stratospheric climatology of all 2006–2017 Aura MLS H_2O observations, and subtracting it from plume observations. It is similar to the climatology used in Chapter 2 with a couple of key differences: i) it is zonally-averaged for both the tropical (30 °S to 30 °N) and mid-latitude (30 °N to 60 °N) bands, and ii) the

troposphere temperature, pressure and humidity profiles are held constant using the AFGL Tropical (TRP), MidLatitude Summer (MidLatS) and MidLatitude Winter (MidLatW) standard soundings. The TRP sounding is applied during the entire year in the 30 °S to 30 °N band, but for 30 °N to 60 °N the MidLatS is applied between August–October, and the MidLatW is applied between November–March. The stratospheric component to this climatology is individual-date-specific, according to the value determined by averaging the MLS record on that date for that latitude band for every year during 2006–2017.

This climatology is used to calculate WVMR anomalies for the Square, Triangle and Circle plume lifetimes (see Figure 4.5) using two different methods. The first method is called the "Fixed Anomaly," and computes an anomaly that is confined to the plume altitudes only within the stratosphere. The plume altitude is determined using the H_2O/CO threshold, and then the WVMR climatology is subtracted from the MLS plume observations at those altitudes only. Other altitudes in the stratospheric portion of the profile are assigned climatological WVMR values. This technique removes the small scale variation in day-to-day UTLS H_2O at altitudes that are not associated with the plume. Additionally, the Square plume uses the TRP tropospheric profile for its entire lifetime for the Fixed Anomaly. The reason for this choice will become apparent when making comparisons, but the short explanation is that this removes the seasonal variation in RF.

The second methodology is termed the "Lagrangian Anomaly," and does not place a plume-altitude constraint on the stratospheric anomaly profile. In other words, this anomaly does consider the small H_2O variations at all stratospheric

altitudes, regardless of whether they are associated with the plume or a CO enhancement. Also, the Square plume's tropospheric profile is allowed to vary as it is tracked from the tropics to the midlatitudes during September–November 2017. It therefore contains tropospheric profiles from any of the three AFGL standard atmospheres mentioned above, depending on the date and latitude of the MLS observation. This is in contrast to the TRP-only troposphere for the Square plume in the Fixed Anomaly methodology.

The idea behind this Lagrangian Anomaly is that RF should be closer to reality since the seasonality, longitude, and full-depth stratospheric H_2O are taken into account when considering the "background" H_2O conditions. The purpose of these calculations is to put a finite real-time RF estimate on stratospheric water vapor intrusions for the three separate long-lived plume sections of the 2017 PNE event. If one were to have a broadband radiometer at the tropopause looking upward and one at the top of the atmosphere (TOA) looking downward at the same column, the actual RF could be measured and compared with this estimate. Unfortunately, such a system is not in place, but these estimates nonetheless are a starting benchmark. The next two sections detail the results for the three plume sections using the above two methodologies.

5.2.1 Fixed Anomaly Results

The Fixed Anomalies following the Square, Triangle, and Circle plume sections are shown in the three left-hand panels Figure 5.5. The red shaded contours are

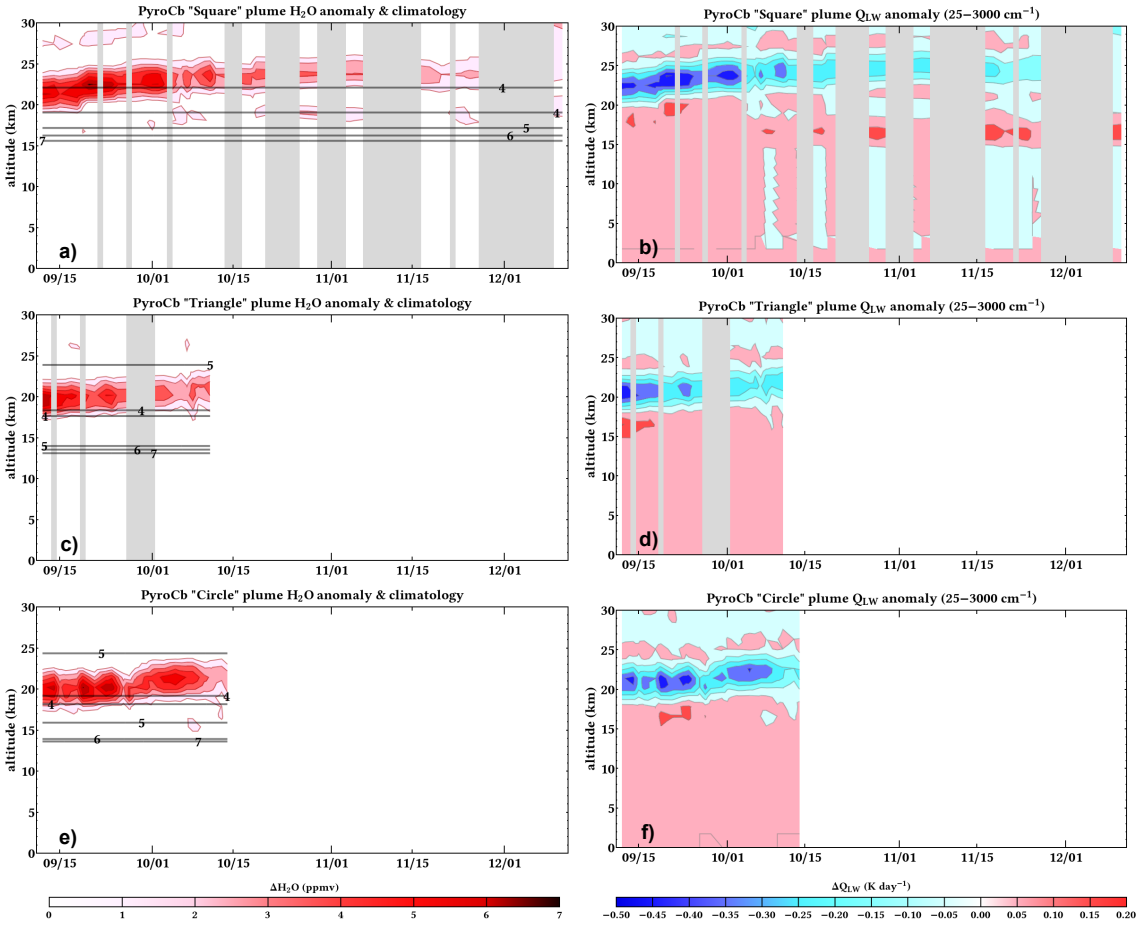

Figure 5.5: (left column) Aura MLS WVMR anomalies (red contours) and fixed local climatologies (black contours) within the three 2017 PNE pyroCb plumes after the 12 September separation. All contours in ppmv. (right column) Longwave LBLRTM heating rate anomalies throughout the troposphere and lower stratosphere computed from these observations. Square plume (top row), Triangle plume (middle row) and Circle plume (bottom row). Vertical gray bars indicate where MLS missed observations.

the WVMR anomalies: values greater than the climatological background amounts (dark gray contours). Light gray vertical bars show dates when MLS did not observe the plumes. The most apparent aspect of all three plumes is the upward motion of each as it ages (See Chapter 4). Note the temporally-invariant WVMR climatology shows typical values $\sim$ 4–5 ppmv within the altitude of the Square plume at $20 < z < 25$ km (a). This plume has anomalies > 7 ppmv in the early days of this time series. Similar results are seen for the midlatitude Triangle and Circle plumes with slightly smaller anomalies, and shorter durations. As each plume ages, the anomalies reduce to values between 2–3 ppmv. Because the climatological background values are between 4–5 ppmv, this puts the total concentrations less than the 7 ppmv threshold, and they are no longer tracked. Note that tropospheric climatological values are not displayed here because the WVMR profile gains several orders of magnitude at lower altitudes (see Figure 1.1a for reference).

The right-hand panels in Figure 5.5 are the corresponding longwave heating anomalies (ΔQ_{LW}) from LBLRTM, and profiles of these Q_{LW} and ΔQ_{LW} are shown in Figure 5.6. The model is run for both the MLS observation profile (with Fixed Anomaly vertical constraints) and the climatology profile, and then differenced to determine ΔQ_{LW}. There is a cooling enhancement within the Square plume down to -0.5 K day^{-1} during the early days (Figure 5.5b), and a very small warming enhancement throughout the depth of the troposphere of $< +0.05$ K day^{-1}. During mid-to-late October, there is an increase in warming at the tropical tropopause ($\sim$ 16 km) and slight cooling below in the troposphere. There is cooling within and above the upper section of WVMR plume anomaly because it of its enhanced absorp-

tion and re-emission at colder temperatures of terrestrial longwave radiation from below. Results from this plume recreate the classic positive RF scenario discussed in introductory radiative transfer texts used to illustrate first-order global warming. The Triangle and Circle ΔQ_{LW} time series panels (d,f) show similar results.

Individual heating rate and the anomaly profiles from this methodology using these plume-centric MLS observations are shown in Figure 5.6. Profiles are colored according to their date (see inset legend for each plume's dates). The ΔQ_{LW} in the right-hand column show the cooling within and above the plumes and the warming at and below the tropopause. The two midlatitude plumes have a slightly smoother warming in the UTLS below the plume (d,f) than the tropical plume (c). The MidLatS profile used to compute the Fixed Anomaly has a climatologically lower tropopause height ($\sim$ 13 km) than the TRP profile ($\sim$ 16 km). An interesting result seen here is that the level of maximum cooling from the plumes (minimum in ΔQ_{LW}) rises to the same distance from the tropopause (9 km) in each case just prior to dissipation (with these thresholds). Stratospheric cooling is strongest in the early observations of the plumes when WVMRs are largest.

Figure 5.7 shows longwave RF at TOA and the tropopause for the Fixed Anomaly of these three plumes. The square plume is above the level of maximum cooling in the standard TRP atmosphere, and its presence slightly decreases the outgoing longwave radiation (OLR) in the tropics throughout the duration of its lifetime. Square plume TOA RF (a) is between 0.00 and -0.15 W m^{-2} for the entire time series. The midlatitude Triangle and Circle plumes on the other hand have weakly positive RF at TOA ($< +0.05$ W m^{-2}) for both of these plumes (c,e).

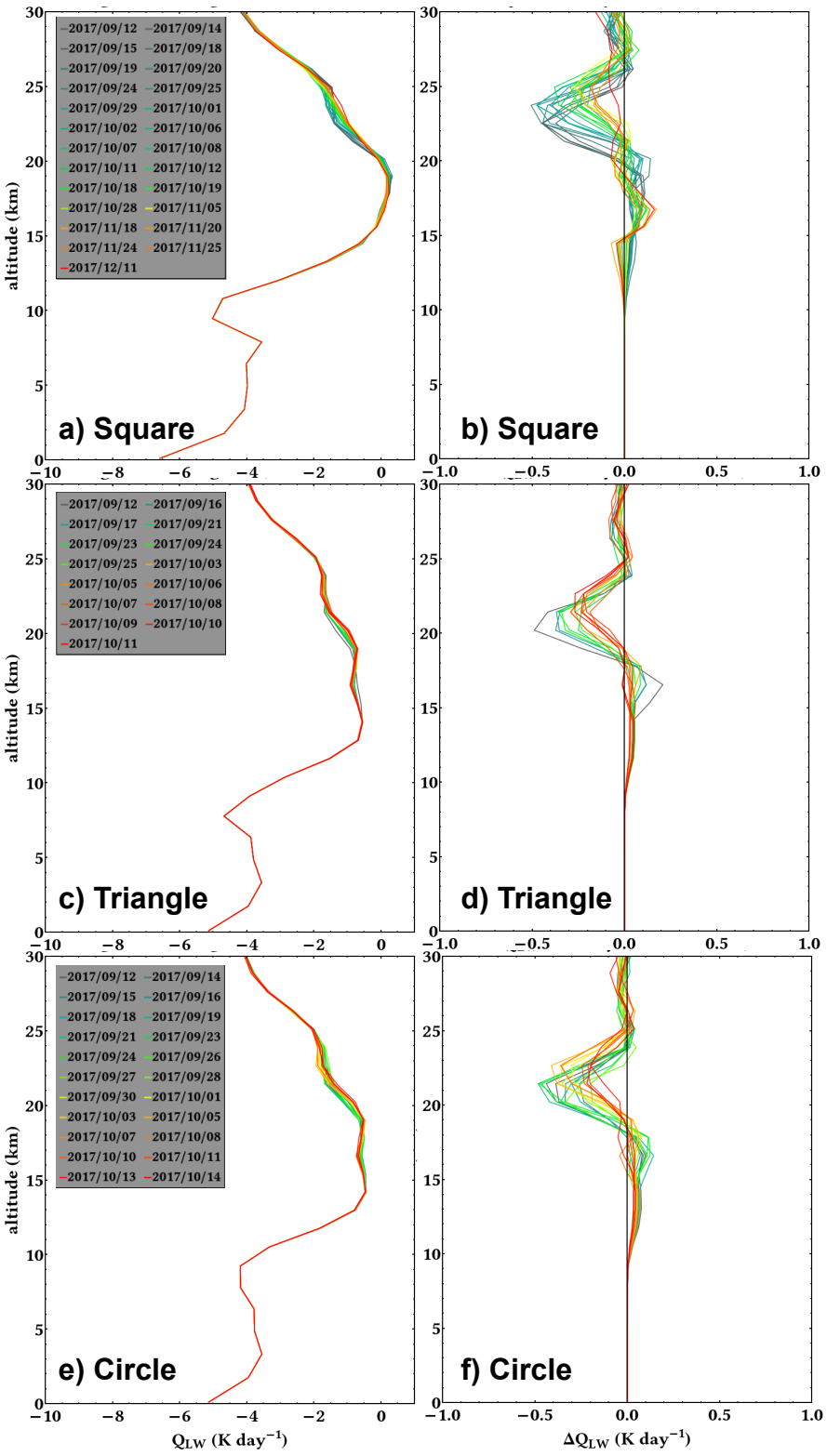

Figure 5.6: (Continued on following page)

Figure 5.6: (continued) Fixed Anomaly H_2O longwave radiative heating (left column) and radiative heating anomalies (right column) for the individual dates of the three plume sections. Note the significant cooling within and above the plume and mild warming below the plume to the tropopause.

This positive RF is from an increase in OLR because the peak in the WVMR anomalies remain within a fairly weak layer of radiative cooling between 17–24 km for the MidLatS atmosphere (see Figure 5.6c, d). The converse is true for the Square plume. There is a decrease in OLR because the H_2O anomaly exists at the top of the minimum (maximum) in longwave cooling (heating) between 20–25 km, and temperature decreases with height much quicker in the TRP lower stratosphere above 25 km, which enhances the "cooling to space" aspect of stratospheric energy budgets (Figure 5.6a).

However, with the exception of the latter half of the Square plume the associated tropopause RF is strongly positive for all cases (b, d, f), and is approximately an order of magnitude greater than TOA forcing. All three plumes show a stronger initial RF with a maximum value reaching between +0.5 and +1.0 W m^{-2} in the first two weeks of this time series, indicating a substantial increase in downward longwave irradiance. Recall from Equations 1.1 and 1.2 that RF is a measure of the change in net flux between the anomaly and control atmospheres, so $RF > 0$ at the tropopause is an increase in $F^{\downarrow}$ into the troposphere.

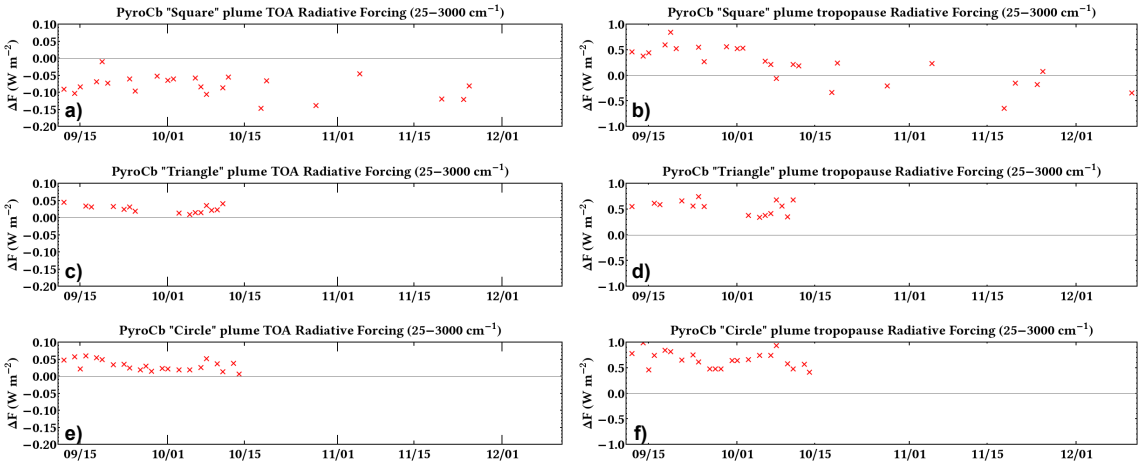

Figure 5.7: TOA (left) and tropopause-level (right) longwave RF using the H_2O Fixed Anomalies from Figure 5.5. Note the Square plume is confined to the tropics for most of its observable duration, and has a negative RF at TOA (a decrease in OLR), whereas the Triangle and Circle plumes are in the mid-latitudes, and have a positive RF at TOA. In all cases, there is a positive RF at the tropopause.

5.2.2 Lagrangian Anomaly Results

Figure 5.8 shows the WVMR anomalies and climatology using this methodology. The dark gray contours on panels (a,c,e) vary with time and location as the plumes are tracked, and the anomalies (red shaded contours) are computed against these background values. The results shown here are similar to the Fixed Anomaly results shown in Figure 5.5 with some small differences. First, the maximum anomaly in the Square plume (= +7.0 ppmv) is +0.5 ppmv greater than the Fixed Anomaly. Absolute WVMR in this case is 11 ppmv with background concentrations between 4.0–4.5 ppmv. Another difference is that there is no positive

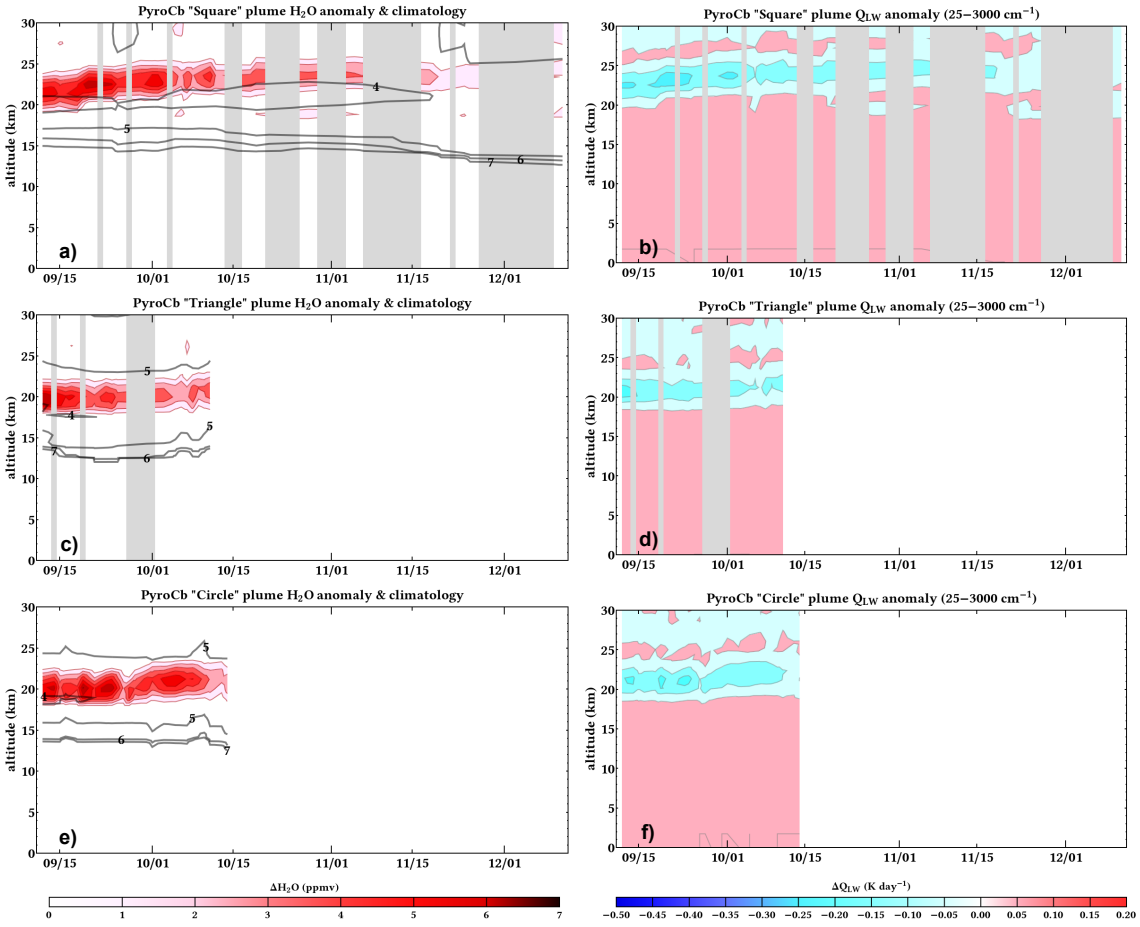

Figure 5.8: As in Figure 5.5, but vapor concentration anomalies and radiative heat flux differences are calculated using the Aura MLS Lagrangian H_2O climatology.

anomaly between $z = 25$–30 km around in the first two weeks of the Square plume as there is in the fixed anomaly (see Figure 5.5a). The most apparent difference is the mitigation of ΔQ_{LW}.

The effect of using a different temperature and vapor climatology is apparent when comparing Figure 5.9 with Figure 5.6. Q_{LW} profiles in Figure 5.9a,c,e show different clusters of heating rates that correspond to the latitude/time regime the

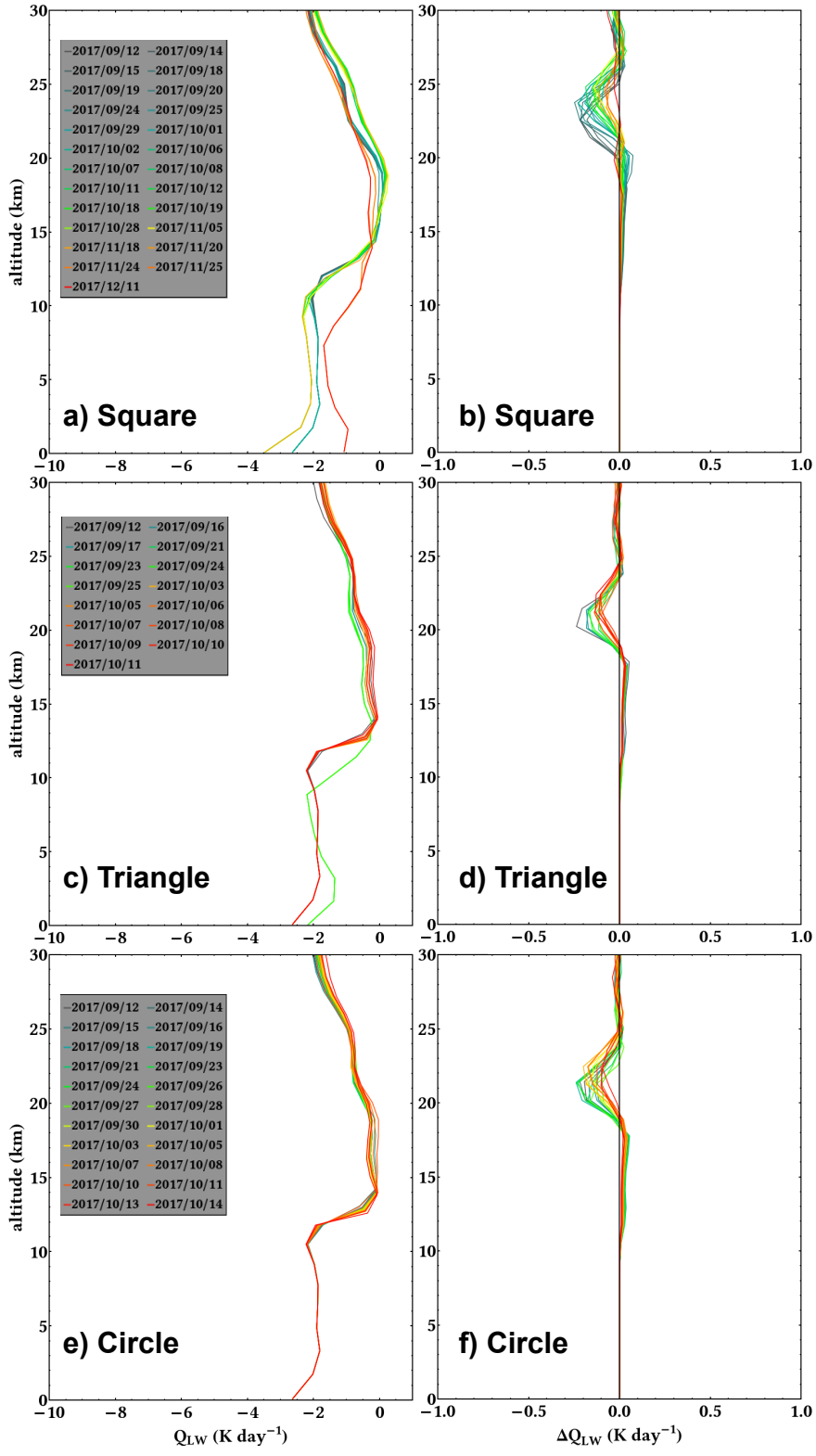

Figure 5.9: (Continued on following page)

Figure 5.9: (continued) As in Figure 5.6, but for the Lagrangian climatology. (a) Note the Square plume has three general Q_{LW} profiles, and (c) the Triangle has two as these plumes move to different latitude bands through summer and winter months.

plume is in. Easily visible at $z < 15$ km, for example, the Square plume moves from the MidLatS to TRP to MidLatW background profiles over its lifetime, and therefore has different Q_{LW} profiles that represent these regimes. Profiles in Figure 5.9b,d,f show that ΔQ_{LW} is approximately half as intense as the Fixed Anomaly at the plume centroid. Once again, there is cooling within an above each of the plumes, but the extrema in ΔQ_{LW} are approximately -0.25 K day^{-1} for all cases. The warming between the tropopause and the plume is significantly mitigated with values < 0.1 K day^{-1} for all cases.

Figure 5.10 illustrates that using a more realistic i) tropospheric climatology, and ii) full-depth stratospheric WVMR has strong effects on the radiative outcomes of the simulation. In the case of these three plumes, the sign of the forcing is the same for all TOA and tropopause RF (Figure 5.7), but the magnitude is again reduced by $\sim 50\%$ as the heating rate anomalies were. These values are smaller than the Fixed Climatology, but are hypothetically more likely to represent reality. It would be very useful to have validation in these results with observations of longwave boundary fluxes.

These results serve as a starting point for the estimation of pyroCb-generated

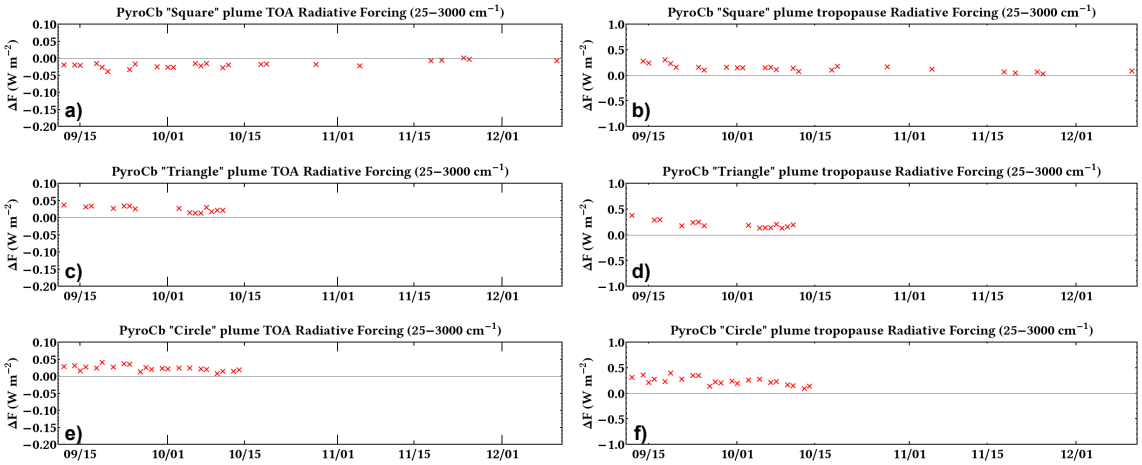

Figure 5.10: As in Figure 5.7, but for the Lagrangian climatology.

stratospheric water vapor forcing. An obvious conclusion from these H_2O *RF* results is that this component is not as important as the aerosol absorption for plume-lofting. In fact, within the plumes, the presence of anomalous H_2O at these altitudes has a cooling effect on the air at the top, and just above the plume; the opposite effect of shortwave absorption by aerosol. This would have a stabilizing effect by reducing the buoyancy of the parcel. Empirically, therefore it must be that the aerosol presence is more important for plume dynamics than H_2O. Although in the long run, H_2O enhancements outlive the relatively large aerosol particles, and would likely contribute for a longer time period to tropopause *RF* as demonstrated here.

5.3 The Big Picture

Having established estimates of H_2O-induced boundary *RF* and stratospheric ΔQ_{LW} for the different 2017 PNE plumes, the next question is how important is this

phenomenon for climate? The answer to this question remains unknown at this time largely because of inadequate observational capability of tropopause flux anomalies on the spatiotemporal scale of the plume. However, given our understanding that lower stratospheric water vapor is a climate relevant variable, it is useful to analyze a longer dataset to determine the frequency with which events of this magnitude occur. Figure 5.11 shows this analysis. The dual H_2O/CO threshold of 7 ppmv/70 ppbv was reapplied to the Aura MLS data record between 2005–2017 for both the northern and southern hemispheres. The data was gridded onto θ-coordinates using the co-located Level 2 MLS Temperature product and the pressure surface of the MLS retrieval, and all data in the range $380 \geq \theta \geq 600$ are analyzed for concurrent measurements meeting this dual threshold criteria.

Immediately apparent in Figure 5.11 is the diabatic rise from the 2017 PNE plumes towards the end of the time series in the northern hemisphere (a). Also noted in Figure 5.11b is the date of the 2009 Black Saturday plume. This latter case does not appear to have any measurements that meet the threshold. In this figure there are annual signals at $550 < \theta < 600$ in both hemispheres from the polar vortex, and annual northern hemisphere signals $380 < \theta < 400$ are from the Asian Monsoon. The polar vortex contains H_2O/CO-rich air from descent at higher stratospheric altitudes. The Monsoon is a time when convection and tropical features can cause pressure increases and temperature decreases at the levels of neutral buoyancy, which can lead to a lower θ at the tropopause level, even thought the geometric height may not significantly change.

Although the PNE plumes are significant, this analysis shows that pyroCb

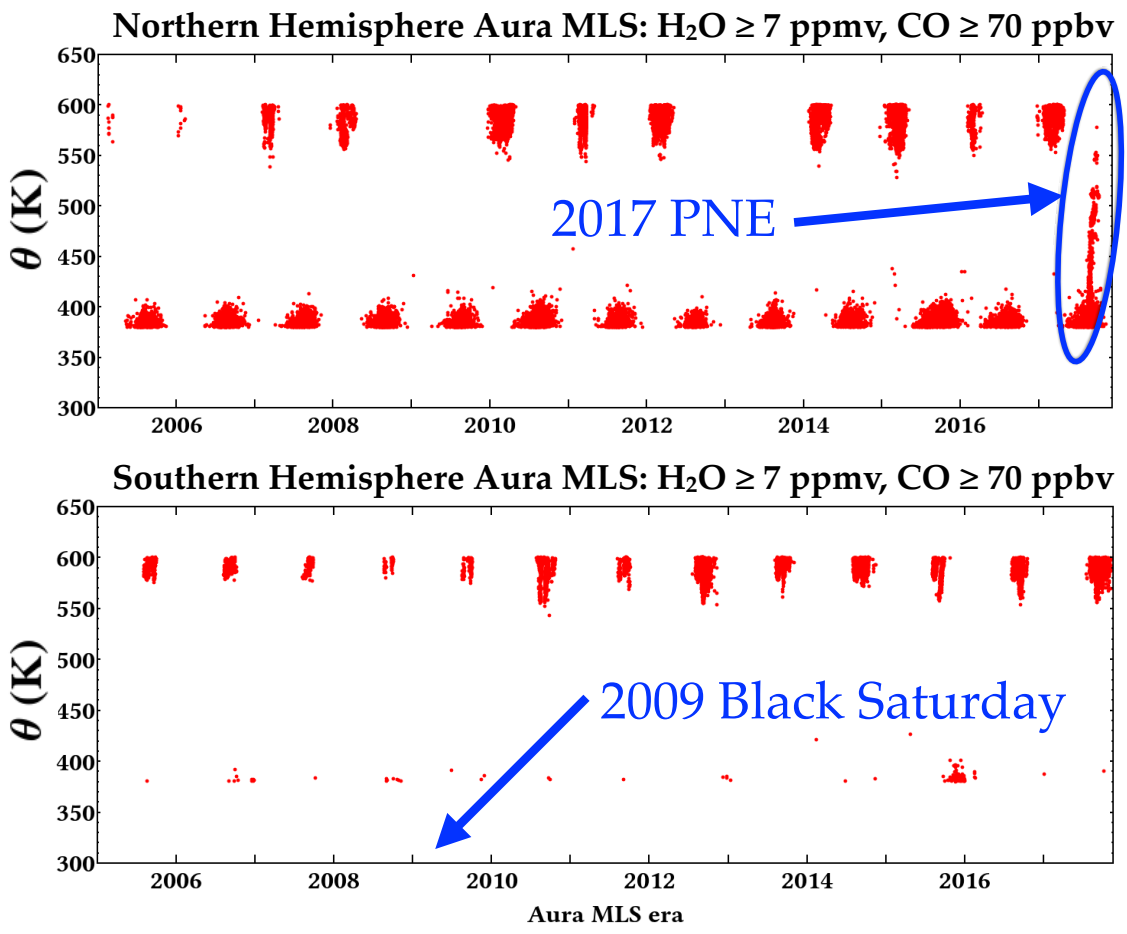

Figure 5.11: The global Aura MLS H_2O/CO data record with constant thresholds. All potential temperature observations are shown for the a) northern hemisphere and b) southern hemisphere where MLS observes $H_2O \geq 7$ ppmv and CO ≥ 70 ppbv. Highlighted are the 2017 PNE plume in the northern hemisphere and the lack of 2009 Black Saturday signal in the southern hemisphere. Note the annual signals between $380 < \theta < 400$ K are from the Monsoon and those between $550 < \theta < 600$ K are from each hemispheres polar vortex.

events of this scale are certainly not common. One *caveat* is the dual threshold used to construct this time series is somewhat conservative for UTLS mixing ratios. An additional analysis was performed with the H_2O threshold lowered to 6 ppmv (not shown), but it did not show an increase in frequency of occurrence. Admittedly, the 2017 PNE case from which the three H_2O-rich plumes emanated was an extremely large and unprecedented event. A seasonal integration of the more typical smaller enhancements from individual events would be a way to estimate the net impact of RF. But given that the largest anomalies from this event produced a highly-localized $RF < +1.0$ W m^{-2}, it seems unlikely that individual events would have a measurable global impact on climate, at least in terms of instantaneous forcing.

However, local effects are still relevant, and the slow-moving, long-lived nature of the 2017 PNE plumes may have significant effects on LS dynamics and heat budgets, which would constitute a second-order effect. The question does remain whether there is a net pyroCb contribution to background stratospheric H_2O in any meaningful way, especially considering the conflicting estimates in water vapor trends mentioned in Chapter 1. This is another question that could be answered by seasonal integration of the smaller events, which is reserved for future research. But the $RF < +1.0$ W m^{-2} result of these plumes is significant when comparing the observationally-based results of *Solomon et al.* (2010) that showed a 1 ppmv stratospheric H_2O reduction "paused" increases in global surface temperature over 2000–2010.

Chapter 6: Summary of Work, Conclusions, and a Future Direction for PyroCb Impact Studies

6.1 PyroCb Convection and Cloud Modeling

A case study of the Great Slave Lake (GSL) pyrocumulonimbus (pyroCb) from 5 August 2014 in Northwest Territories of Canada was analyzed using satellite- and ground-based observations, and multiple ARW cloud-resolving simulations. This pyroCb was an intense storm that penetrated the tropopause, reaching up to $\sim$ 14 km ($\theta \simeq$380 K). Passive imagery from the polar-orbiting MODerate resolution Imaging Spectroradiometer (MODIS) and Visible Infrared Imaging Radiometer Suite (VIIRS) and the Geostationary Operational Environmental Satellite (GOES)-West detailed the convective lifecycle of this pyroCb, and allowed for comparisons with a concurrent meteorological cumulonimbus (Cb) that formed to the south in Alberta. Brightness Temperatures (BT) at thermal- and near-infrared channels indicated the cloud had a large number density of ice particles with a very small effective radius.

The CloudSat 94 GHz Cloud Profiling Radar (CPR) and Cloud-Aerosol Lidar with Orthogonal Polarization (CALIOP) instruments made fortuitous intersections within a few minutes of the active core of both the GSL pyroCb and the Alberta

Cb, and allowed for direct comparison of the internal structure of the storms based on radar reflectivity profiles. Additional deep convective core (DCC) cases from June–August 2014 in the same region were identified using the CPR and also analyzed. The pyroCb CPR profiles indicated a suppression of precipitation, and rapid hydrometeor growth between the freezing level (FL) and homogeneous freezing level (HFL), whereas the Alberta Cb and 15 other meteorological DCC CPR profiles showed the presence of precipitation, and smaller changes in radar reflectivity between the FL and HFL.

An analysis of the meteorology indicated that the GSL pyroCb formed in favorable convective conditions, but fire radiative power (FRP) retrievals from GOES-West and a lack of meteorological trigger showed that the fire itself likely initiated the convection. Surface observations from the Buffalo Junction ground station, over which the pyroCb advected during the active convection stage, showed no precipitation reached the surface. GOES-West showed the GSL pyroCb anvil was detectable in thermal infrared imagery for at least 24 hours until it became indistinguishable from nearby (and lower-altitude) cirrus clouds. This lifetime was approximately 50% longer than the Alberta Cb anvil, which is in agreement with anvil lifetime results published by *Lindsey and Fromm* (2008).

The detrained GSL pyroCb anvil was tracked in the lower stratosphere over two weeks using a combination of HYbrid Single Particle Lagrangian Integrated Trajectories (HYSPLIT) and CALIOP observations of the aerosol/ice plume. Concurrent Microwave Limb Sounder (MLS) observations of this plume indicated that ice was present initially, but sublimated within a week. MLS also observed a sub-

stantial increase in water vapor mixing ratio (WVMR) values over this time that produced plume-averaged anomalies as large as +2 ppmv (> 50%) relative to a 2005–2014 climatology. In general, these WVMR anomalies appeared to be anti-correlated with ice water content (IWC) observations, which implies aging pyroCb plumes that undergo ice sublimation could enhance WVMR on short timescales.

Simulations of the GSL pyroCb using Advanced Research WRF (ARW) showed that updraft mass fluxes, cloud ice concentrations, and detrained WVMR were heavily influenced by the surface sensible and latent heat fluxes prescribed over the fire. Sensitivity tests on other initial conditions, such as lowering the surface aerosol concentrations and limiting the moisture entrainment indicated these had a smaller effect. These tests were performed using a full simulation of the GSL pyroCb as a control. Although the pyroCb was less sensitive to both aerosol and moisture entrainment, the aerosol concentration had the least influence.

This approach is unique from most convective modeling studies in that the control is based on the most intense situation (pyroCb). Other convective modeling studies have found that aerosol increases substantially impact updraft intensity and microphysics (*Khain et al.*, 2005; *Fan et al.*, 2013), but when starting with a pyroCb, the model showed that aerosols are not nearly as important as the surface heat fluxes. This case agrees with previous idealized pyroCb modeling (*Reutter et al.*, 2014). The ARW simulations shown here also indicated there is a substantial amount of vapor detrainment in the case of the GSL pyroCb, but by itself the absolute humidity is not enough to match MLS observations of the plume one week later. We estimate that a 30% survival of all water produced in the model (including both sublimation

from ice clouds and absolute humidity detrained at cloud top levels) would account for the 7-9 ppmv values observed in the aging plume.

6.2 Stratospheric PyroCb Aerosol

The methodology of estimating the stratospheric injection mass of the August 2017 Pacific Northwest pyroCb Event (PNE) published in *Peterson et al.* (2018) was demonstrated to be valid by simulating the plume's Ultra-Violet Aerosol Index (UVAI) signal from the Ozone Mapping and Profiler Suite (OMPS) instrument. Total mass estimates were 0.2 ± 0.1 Tg ($\pm$50% error) based on a mass density (M_ρ)-lidar backscatter relationship using a range of optical properties and vertical plume depth estimates. The 532 nm total attenuated backscatter (β'_{532}; CALIOP's main measurement) suggested the stratospheric depth of the plume was 1.5–2.0 km. This information was colocated with OMPS UVAI imagery to determine that UVAI = 15 is a sufficient threshold for determining stratospheric aerosol presence in locations where the nadir-viewing CALIOP lidar is not able to measure depth. The area of the plume equals the total area of pixels subtended by this UVAI threshold and was multiplied by the stratospheric depth to determine an overall initial plume volume $V \simeq 1.475 \times 10^{15}$ km^3.

The Santa Barbara DISORT Atmospheric Radiative Transfer (SBDART) model was used to simulate the two-wavelength OMPS UVAI signal using a CALIOP stratospheric aerosol optical depth (AOD) estimate along the track of the observation. This simulation validated the total mass estimate, and provided confidence in

both the empirical UVAI threshold of 15, and the total volume estimate of the 2017 PNE plume.

The radiatively-induced self-lofting of this plume was analyzed both from an observational and modeling standpoint. The plume was tracked using a dual MLS threshold for CO/H_2O, and was shown to separate into three distinct plume sections (referred to herein as the "Square," "Circle," and "Triangle" plumes) over central Asia one month after the 12 August pyroCb date. Each of these plumes was shown to circumnavigate the globe in either the midlatitudes (Circle and Triangle) or the tropics (Square). The Square plume was lofted to approximately 25 km ($\theta \simeq 600$ K) over the course of three months, and encountered the Easterly winds in the tropical lower stratosphere (LS). WVMR for these plumes was ≥ 7 ppmv for the entire three months of observation, which is approximately 2–3 ppmv (+40–75%) above the background values for this part of the LS.

This diabatic rise was simulated using a simple 1D modeling framework that combined heating rate anomalies (ΔQ) computed from SBDART with an empirical heat accumulation efficiency parameter (ε). Using CALIOP stratospheric extinction profiles as input into SBDART, ΔQ was estimated at each observation time, and $\varepsilon = 30\%$ was shown to closely match the rate of observed diabatic rise. Two additional cases were examined for this phenomenon: the much smaller GSL pyroCb plume, and the relatively-large 2009 Black Saturday event from Australia. Both cases had similar results showing $\varepsilon = 30\%$ best matched the observed rates of rise, in spite of their differences in overall aerosol loading and the large difference in lifetimes.

6.3 Water Vapor Forcing

The 2017 PNE plumes were shown to have significant enhancements in stratospheric H_2O. Monthly global statistics showed the plume's high correlation with CO (an excellent biomass burning tracer), and the upward movement of the plume as it aged. During August 2017, there are very little enhancements at altitudes $20 \leq z \leq 25$ km, and the H_2O that is present at these altitudes is between 4–6 ppmv with coincident CO mixing ratios mostly ≤ 40 ppbv. In October and November at these higher altitudes, median WVMR has increased to > 5 ppmv with a larger width in count density histograms. From these statistics alone, it appeared that this event increased the LS median WVMR concentration by $\sim 20\%$ (for all locations where CO mixing ratios ≥ 20 ppbv.

The longwave ($25 \leq \tilde{\nu} \leq 3000$ cm^{-1}) radiative effects of this WVMR increase were tested for each of the Square, Circle and Triangle plumes using two different anomaly computations: "Fixed" and " Lagrangian" frameworks. Both anomaly methodologies had similar results, but the more realistic Lagrangian Anomaly reduced the stratospheric ΔQ_{LW} from -0.5 to -0.25 K day^{-1}, and also reduced the tropopause radiative forcing RF from +0.5–1.0 W m^{-2} to +0.25–0.5 W m^{-2}. These boundary RF were shown to slightly weaken as the plume aged and the WVMR enhancements were reduced. The tropical Square plume showed $RF \simeq -0.025$ W m^{-2} at the top of the atmosphere (TOA) corresponding to a decrease in outgoing longwave radiation (OLR). This is in contrast with the midlatitude Circle and Triangle plumes that showed $RF \simeq +0.025$ W m^{-2} for the observable lifetimes.

The reasons behind this difference were explained to be the local (tropical or mid-latitude) levels of maximum radiative cooling (for the longwave). The Square plume existed toward the top of this level, and had a steeper lapse rate above it than did the Circle and Triangle plumes.

The water vapor effects of the PNE event were put into context by showing global statistics for both hemispheres. This event is unprecedented in the Aura MLS data record, even when comparing with the previously-known largest pyroCb event: Black Saturday. The record showed that this type of event is very uncommon. However, the localized effects of many smaller pyroCbs over the course of a season may be important.

6.4 Future Work

The observations made by the A-Train and the ARW model results indicate that lower stratospheric water vapor may be influenced by pyroCb activity, at least on short time scales. As recent studies have shown, these pyroCb events are a relatively common occurrence every season (*Peterson et al.*, 2017a). Given the radiative significance of this greenhouse gas in the UTLS, it is worth considering a larger research effort into understanding the net impact that these events may have. Integrating the smaller events into a larger estimate of the seasonal impact of pyroCb on stratospheric water vapor forcing, and further advancements in tracking and modeling the self-lofting mechanism are needed. Tracking individual plumes is a valuable technique, but it is now possible to undertake a seasonal, global ap-

proach to the impact of these events. There are rich and large observational datasets from various earth-observing satellites in place that are underutilized for this type of research. Satellite-based sounding instruments such as MLS, Atmospheric Infrared Sounder (AIRS, *Chahine et al.*, 2006), Infrared Atmospheric Sounding Interferometer (IASI, *Blumstein et al.*, 2004) and Measurements of Pollution in the Troposphere (MOPITT, *Emmons et al.*, 2004) have different capabilities that complement each other on long time scales when quantifying tropospheric and UTLS H_2O and CO. It would be beneficial to both the meteorological-, climate-, and fire behavior-communities to explore the local and global impact of pyroCb.

Bibliography

Austin, R., A. Heymsfield, and G. Stephens (2009), Retrieval of ice cloud microphysical parameters using the CloudSat millimeter-wave radar and temperature, *J. Geophys. Res.*, *114*(D8).

Bates, D. R., and M. Nicolet (1950), The photochemistry of atmospheric water vapor, *J. Geophys. Res.*, *55*(3), 301–327.

Bedka, K. (2011), Overshooting cloud top detections using MSG SEVIRI Infrared brightness temperatures and their relationship to severe weather over Europe, *Atmos. Res.*, *99*(2), 175–189.

Beringer, J., L. Hutley, N. Tapper, A. Coutts, A. Kerley, and A. O'grady (2003), Fire impacts on surface heat, moisture and carbon fluxes from a tropical savanna in northern Australia, *Int. J. Wildland Fire*, *12*(4), 333–340.

Blumstein, D., G. Chalon, T. Carlier, C. Buil, P. Hebert, T. Maciaszek, G. Ponce, T. Phulpin, B. Tournier, D. Simeoni, et al. (2004), IASI instrument: Technical overview and measured performances, in *Infrared Spaceborne Remote Sensing XII*, vol. 5543, pp. 196–208, International Society for Optics and Photonics.

Brasseur, G., and S. Solomon (1986), *Aeronomy of the Middle Atmosphere*, 452 pp., Reidel, Dordrecht.

Brewer, A. (1949), Evidence for a world circulation provided by the measurements of helium and water vapour distribution in the stratosphere, *Q. J. Roy. Meteor. Soc.*, *75*(326), 351–363.

Chahine, M., T. Pagano, H. Aumann, R. Atlas, C. Barnet, J. Blaisdell, L. Chen, M. Divakarla, E. Fetzer, M. Goldberg, et al. (2006), Airs: Improving weather forecasting and providing new data on greenhouse gases, *B. Am. Meteorol. Soc.*, *87*(7), 911–926.

Clough, S., M. Iacono, and J. Moncet (1992), Line-by-Line Calculation of Atmospheric Fluxes and Cooling Rates: Application to Water Vapor, *J. Geophys. Res.*, *97*(D14), 15,761–15,785.

Clough, S., M. Shephard, E. Mlawer, J. Delamere, M. Iacono, K. Cady-Pereira, S. Boukabara, and P. Brown (2005), Atmospheric radiative transfer modeling: a summary of the AER codes, *J. Quant. Spectrosc. Ra.*, *91*(2), 233–244.

Crutzen, P. J., and J. W. Birks (1982), The atmosphere after a nuclear war: Twilight at noon, *Ambio*, *11*(2/3), 114–125.

Damoah, R., N. Spichtinger, R. Servranckx, M. Fromm, E. Eloranta, I. Razenkov, P. James, M. Shulski, C. Forster, and A. Stohl (2006), A case study of pyro-convection using transport model and remote sensing data, *Atmos. Chem. Phys.*, *6*(1), 173–185, doi:10.5194/acp-6-173-2006.

Delanoë, J., and R. Hogan (2010), Combined CloudSat-CALIPSO-MODIS retrievals of the properties of ice clouds, *J. Geophys. Res.*, *115*(D4).

Dessler, A., M. Schoeberl, T. Wang, S. Davis, and K. Rosenlof (2013), Stratospheric water vapor feedback, *P. Natl. Acad. Sci. USA*, *110*(45), 18,087–18,091, doi:10.1073/pnas.1310344110.

Dessler, A. E. (2002), The effect of deep, tropical convection on the tropical tropopause layer, *J. Geophys. Res*, *107*(4033), 9169–9205.

Dirksen, R. J., K. F. Boersma, J. De Laat, P. Stammes, G. R. Van Der Werf, M. V. Martin, and H. M. Kelder (2009), An aerosol boomerang: Rapid around-the-world transport of smoke from the December 2006 Australian forest fires observed from space, *J. Geophys. Res.*, *114*(D21), D21,201, doi:10.1029/2009JD012360.

Dowdy, A., M. Fromm, and N. McCarthy (2017), Pyrocumulonimbus lightning and fire ignition on Black Saturday in southeast Australia, *J. Geophys. Res.*, *122*(14), 7342–7354.

Emmons, L., M. Deeter, J. Gille, D. Edwards, J. Attié, J. Warner, D. Ziskin, G. Francis, B. Khattatov, V. Yudin, et al. (2004), Validation of Measurements of Pollution in the Troposphere (MOPITT) CO retrievals with aircraft in situ profiles, *J. Geophys. Res*, *109*(D3).

Fan, J., L. Leung, D. Rosenfeld, Q. Chen, Z. Li, J. Zhang, and H. Yan (2013), Microphysical effects determine macrophysical response for aerosol impacts on deep convective clouds, *P. Natl. Acad. Sci. USA*, *110*(48), E4581–E4590.

Field, R., M. Luo, M. Fromm, A. Voulgarakis, S. Mangeon, and J. Worden (2016), Simulating the Black Saturday 2009 smoke plume with an interactive composition-climate model: Sensitivity to emissions amount, timing, and injection height, *J. Geophys. Res.*, *121*(8), 4296–4316.

Filipiak, M., R. Harwood, J. Jiang, Q. Li, N. Livesey, G. Manney, W. Read, M. Schwartz, J. Waters, and D. Wu (2005), Carbon monoxide measured by the eos microwave limb sounder on aura: First results, *Geophys. Res. Lett.*, *32*(14).

Forster, P., V. Ramaswamy, P. Artaxo, T. Berntsen, R. Betts, D. W. Fahey, J. Haywood, J. Lean, D. C. Lowe, G. Myhre, J. Nganga, R. Prinn, G. Raga, M. Schulz, and R. Van Dorland (2007), Changes in Atmospheric Constituents and in Radiative Forcing, *Climate Change 2007: The Physical Science Basis. Contribution of Working Group I to the Fourth Assessment Report of the Intergovernmental Panel on Climate Change*.

Fouquart, Y., and B. Bonnel (1980), Computations of solar heating of the earth's atmosphere: A new parameterization, *Contrib. Atmos. Phys.*, *53*, 35–62.

Fromm, M., A. Tupper, D. Rosenfeld, R. Servranckx, and R. McRae (2006), Violent pyro-convective storm devastates Australia's capital and pollutes the stratosphere, *Geophys. Res. Lett.*, *33*(5), doi:10.1029/2005GL025161.

Fromm, M., E. Shettle, K. Fricke, C. Ritter, T. Trickl, H. Giehl, M. Gerding, J. Barnes, M. O'Neill, S. Massie, et al. (2008a), Stratospheric impact of the Chisholm pyrocumulonimbus eruption: 2. Vertical profile perspective, *J. Geophys. Res.*, *113*(D8), D08,203, doi:10.1029/2007JD009147.

Fromm, M., O. Torres, D. Diner, D. Lindsey, B. Hull, R. Servranckx, E. Shettle, and Z. Li (2008b), Stratospheric impact of the Chisholm pyrocumulonimbus eruption: 1. Earth-viewing satellite perspective, *J. Geophys. Res.*, *113*(D8), D08,202, doi:10.1029/2007JD009153.

Fromm, M., D. T. Lindsey, R. Servranckx, G. Yue, T. Trickl, R. Sica, P. Doucet, S. Godin-Beekmann, et al. (2010), The untold story of pyrocumulonimbus, *B. Am. Meteorol. Soc.*, *91*(9), 1193, doi:10.1175/2010BAMS3004.1.

Fromm, M., R. McRae, J. Sharples, and G. Kablick (2012), Pyrocumulonimbus Pair in Wollemi and Blue Mountains National Parks, 22 November 2006, *Aust. Meteorol. Ocean. J.*, (62), 117–126.

Fromm, M., G. Kablick, G. Nedoluha, E. Carboni, R. Grainger, J. Campbell, and J. Lewis (2014), Correcting the record of volcanic stratospheric aerosol impact: Nabro and Sarychev Peak, *J. Geophys. Res.*, *119*(17), doi:10.1002/2014JD021507.

Fromm, M. D., and R. Servranckx (2003), Transport of forest fire smoke above the tropopause by supercell convection, *Geophys. Res. Lett.*, *30*(10), 1542, doi:10.1029/2002GL016820.

Fromm, M. D., R. M. Bevilacqua, R. Servranckx, J. Rosen, J. P. Thayer, J. Herman, and D. Larko (2005), Pyro-cumulonimbus injection of smoke to the stratosphere: Observations and impact of a super blowup in northwestern Canada on 3–4 August 1998, *J. Geophys. Res.*, *110*(D8), doi:10.1029/2004JD005350.

Fueglistaler, S., A. E. Dessler, T. J. Dunkerton, I. Folins, Q. Fu, and P. W. Mote (2009), Tropical tropopause layer, *Rev. Geophys.*, *47*, RG1004, doi:10.1029/2008RG000267.

Gatebe, C., T. Varnai, R. Poudyal, C. Ichoku, and M. King (2012), Taking the pulse of pyrocumulus clouds, *Atmos. Environ.*, *52*, 121–130.

Gordon, I., L. Rothman, C. Hill, R. Kochanov, Y. Tan, P. Bernath, M. Birk, V. Boudon, A. Campargue, K. Chance, et al. (2017), The HITRAN2016 molecular spectroscopic database, *J. Quant. Spectrosc. Ra.*, *203*, 3–69.

Haines, D. (1988), A lower atmosphere severity index for wild-land fires, *Natl. Wea. Dig.*, *13*(3), 23–27.

Hegglin, M., D. Plummer, T. Shepherd, J. Scinocca, J. Anderson, L. Froidevaux, B. Funke, D. Hurst, A. Rozanov, J. Urban, et al. (2014), Vertical structure of stratospheric water vapour trends derived from merged satellite data, *Nat. Geosci.*, *7*(10), 768, doi:10.1038/NGEO2236.

Holton, J., P. H. Haynes, M. E. McIntyre, A. Douglass, R. Rood, and Pf. (1995), Stratosphere-troposphere exchange, *Rev. Geophys.*, *33*(4), 403–439, doi:10.1029/95RG02097.

Hu, Y., D. Winker, M. Vaughan, B. Lin, A. Omar, C. Trepte, D. Flittner, P. Yang, S. Nasiri, B. Baum, et al. (2009), CALIPSO/CALIOP cloud phase discrimination algorithm, *J. Atmos. Ocean. Tech.*, *26*(11), 2293–2309.

Hurst, D., S. Oltmans, H. Vömel, K. Rosenlof, S. Davis, E. Ray, E. Hall, and A. Jordan (2011), Stratospheric water vapor trends over Boulder, Colorado: Analysis of the 30 year Boulder record, *J. Geophys. Res.*, *116*(D2), D02,306, doi:10.1029/2010JD015065.

Jensen, E., P. Lawson, B. Baker, B. Pilson, Q. Mo, A. Heymsfield, A. Bansemer, T. Bui, M. McGill, D. Hlavka, et al. (2009), On the importance of small ice crystals in tropical anvil cirrus, *Atmos. Chem. Phys.*, *9*(15), 5519–5537.

Jensen, E. J., L. Pfister, A. S. Ackerman, A. Tabazadeh, and O. B. Toon (2001), A conceptual model of the dehydration of air due to freeze-drying by optically thin, laminar cirrus rising slowly across the tropical tropopause, *J. Geophys. Res.*, *106*(D15), 17–237.

Kablick, G., M. Fromm, S. Miller, P. Partain, D. Peterson, S. Lee, Y. Zhang, A. Lambert, and Z. Li (2018), The Great Slave Lake pyroCb of 5 August 2014: observations, simulations, comparisons with regular convection, and impact on UTLS water vapor, *J. Geophys. Res.*, *123*(21), 12–332, doi:10.1029/2018JD028965.

Khain, A., D. Rosenfeld, and A. Pokrovsky (2005), Aerosol impact on the dynamics and microphysics of deep convective clouds, *Q. J. Roy. Meteor. Soc.*, *131*(611), 2639–2663.

Khaykin, S., S. Godin-Beekmann, A. Hauchecorne, J. Pelon, F. Ravetta, and P. Keckhut (2018), Stratospheric smoke with unprecedentedly high backscatter

observed by lidars above southern France, *Geophys. Res. Lett.*, *45*(3), 1639–1646, doi:10.1002/2017GL076763.

Kiehl, J., and K. Trenberth (1997), Earth's annual global mean energy budget, *B. Am. Meteorol. Soc.*, *78*(2), 197–208.

Kley, D., J. Russell III, and C. Phillips (2000), SPARC Assessment of Water Vapour in the Stratosphere and Upper Troposphere, *WMO/TD No. 1043 WCRP 113*, World Climate Research Programme, Geneva.

Laat, A., D. Stein Zweers, and R. Boers (2012), A solar escalator: Observational evidence of the self-lifting of smoke and aerosols by absorption of solar radiation in the February 2009 Australian Black Saturday plume, *J. Geophys. Res.*, *117*(D4).

Lareau, N., and C. Clements (2016), Environmental controls on pyrocumulus and pyrocumulonimbus initiation and development, *Atmos. Chem. Phys.*, *16*(6), 4005.

Li, Z., F. Niu, J. Fan, Y. Liu, D. Rosenfeld, and Y. Ding (2011), Long-term impacts of aerosols on the vertical development of clouds and precipitation, *Nat. Geosci.*, *4*(12), 888–894, doi:10.1038/NGEO1313.

Lindsey, D., and M. Fromm (2008), Evidence of the cloud lifetime effect from wildfire-induced thunderstorms, *Geophys. Res. Lett.*, *35*(22), L22,809, doi:10.1029/2008GL035680.

Lindsey, D., D. Hillger, L. Grasso, and J. Knaff, J.and Dostalek (2006), GOES Climatology and Analysis of Thunderstorms with Enhanced 3.9-μ m Reflectivity, *Monthly weather review*, *134*(9), 2342–2353.

Livesey, N., W. Read, P. Wagner, L. Froidevaux, A. Lambert, G. Manney, L. Millán, H. Pumphrey, M. Santee, M. Schwartz, S. Wang, R. Fuller, et al. (2018), Version 4.2x Level 2 data quality and description document, *JPL D-33509 Rev. D*.

Lossow, S., D. F. Hurst, K. H. Rosenlof, G. P. Stiller, T. von Clarmann, S. Brinkop, M. Dameris, P. Jöckel, D. E. Kinnison, J. Plieninger, D. A. Plummer, F. Ploeger, W. G. Read, E. E. Remsberg, J. M. Russell, and M. Tao (2018), Trend differences in lower stratospheric water vapour between Boulder and the zonal mean and their role in understanding fundamental observational discrepancies, *Atmos. Chem. Phys.*, *18*(11), 8331–8351, doi:10.5194/acp-18-8331-2018.

Luderer, G., J. Trentmann, T. Winterrath, C. Textor, M. Herzog, H. Graf, and M. Andreae (2006), Modeling of biomass smoke injection into the lower stratosphere by a large forest fire (part ii): sensitivity studies, *Atmos. Chem. Phys.*, *6*(12), 5261–5277.

Mesinger, F., G. DiMego, E. Kalnay, K. Mitchell, P. Shafran, W. Ebisuzaki, D. Jović, J. Woollen, E. Rogers, E. Berbery, et al. (2006), North American regional reanalysis, *B. Am. Meteorol. Soc.*, *87*(3), 343–360.

Miller, S. D., and G. L. Stephens (2001), CloudSat instrument requirements as determined from ECMWF forecasts of global cloudiness, *J. Geophys. Res*, *106*(D16), 17,713–17, doi:10.1029/2000JD900645.

Minschwaner, K., H. Su, and J. Jiang (2016), The upward branch of the Brewer-Dobson circulation quantified by tropical stratospheric water vapor and carbon monoxide measurements from the Aura Microwave Limb Sounder, *J. Geophys. Res*, *121*(6), 2790–2804, doi:10.1002/2015JD023961.

Mlawer, E., S. Taubman, P. Brown, M. Iacono, and S. Clough (1997), Radiative transfer for inhomogeneous atmospheres: Rrtm, a validated correlated-k model for the longwave, *J. Geophys. Res.*, *102*(D14), 16,663–16,682.

Mote, P., K. Rosenlof, M. McIntyre, E. Carr, J. Gille, J. Holton, J. Kinnersley, H. Pumphrey, J. Russell, and J. Waters (1996), An atmospheric tape recorder: The imprint of tropical tropopause temperatures on stratospheric water vapor, *J. Geophys. Res.*, *101*(D2), 3989–4006.

Nikonovas, T., P. North, and S. Doerr (2017), Particulate emissions from large North American wildfires estimated using a new top-down method, *Atmos. Chem. Phys.*, *17*(10), 6423–6438, doi:10.5194/acp-17-6423-2017.

Oinas, V., A. A. Lacis, D. Rind, D. T. Shindell, and J. E. Hansen (2001), Radiative cooling by stratospheric water vapor: Big differences in GCM results, *Geophys. Res. Lett.*, *28*(14), 2791–2794.

Peterson, D., M. Fromm, J. Solbrig, E. Hyer, M. Surratt, and J. Campbell (2017a), Detection and inventory of intense pyroconvection in western North America using GOES-15 daytime infrared data, *J. Appl. Meteorol. Clim.*, *56*(2), 471–493.

Peterson, D., E. Hyer, J. Campbell, J. Solbrig, and M. Fromm (2017b), A conceptual model for development of intense pyrocumulonimbus in western North America, *Mon. Wea. Rev.*, *145*(6), 2235–2255.

Peterson, D., J. Campbell, E. Hyer, M. Fromm, G. Kablick, J. Cossuth, and M. DeLand (2018), Wildfire-driven thunderstorms cause a volcano-like stratospheric injection of smoke, *Clim. Atmos. Sci.*, *1*, 30.

Potter, B. (2005), The role of released moisture in the atmospheric dynamics associated with wildland fires, *Int. J. Wildland Fire*, *14*(1), 77–84.

Pruppacher, H. R., and J. D. Klett (1997), *Microphysics of Clouds and Precipitation*, Kluwer Academic Publishers.

Pumphrey, H., M. Santee, N. Livesey, M. Schwartz, and W. Read (2011), Microwave Limb Sounder observations of biomass-burning products from the Australian bush fires of February 2009, *Atmos. Chem. Phys.*, *11*(13), 6285–6296, doi:10.5194/acp-11-6285-2011.

Radke, L., J. Lyons, P. Hobbs, and R. Weiss (1990), Smokes from the burning of aviation fuel and their self-lofting by solar heating, *J. Geophys. Res.*, *95*(D9), 14,071–14,076.

Ramaswamy, V., M. L. Chanin, J. Angell, J. Barnett, D. Gaffen, M. Gelman, P. Keckhut, Y. Koshelkov, K. Labitzke, J. J. R. Lin, et al. (2001), Stratospheric temperature trends: Observations and model simulations, *Rev. Geophys.*, *39*(1), 71–122.

Randel, W., and E. Jensen (2013), Physical processes in the tropical tropopause layer and their roles in a changing climate, *Nat. Geosci.*, *6*(3), 169.

Randel, W., M. Park, L. Emmons, D. Kinnison, P. Bernath, K. A. Walker, C. Boone, and H. Pumphrey (2010), Asian monsoon transport of pollution to the stratosphere, *Science*, *328*(5978), 611–613, doi:10.1126/science.1182274.

Reid, J., T. Eck, S. Christopher, R. Koppmann, O. Dubovik, D. Eleuterio, B. Holben, E. Reid, and J. Zhang (2005), A review of biomass burning emissions part III: intensive optical properties of biomass burning particles, *Atmos. Chem. Phys.*, *5*(3), 827–849.

Reutter, P., J. Trentmann, A. Seifert, P. Neis, H. Su, D. Chang, M. Herzog, H. Wernli, M. Andreae, and U. Pöschl (2014), 3-D model simulations of dynamical and microphysical interactions in pyroconvective clouds under idealized conditions, *Atmos. Chem. Phys.*, *14*(14), 7573–7583.

Ricchiazzi, P., S. Yang, C. Gautier, and D. Sowle (1998), SBDART: A research and teaching software tool for plane-parallel radiative transfer in the Earth's atmosphere, *B. Am. Meteorol. Soc.*, *79*(10), 2101–2114.

Robock, A., and B. Zambri (2018), Did Smoke From City Fires in World War II Cause Global Cooling?, *J. Geophys. Res.*, *123*(18), 10–314.

Robock, A., L. Oman, G. Stenchikov, O. Toon, C. Bardeen, and R. Turco (2007a), Climatic consequences of regional nuclear conflicts, *Atmos. Chem. Phys.*, *7*(8), 2003–2012, doi:10.5194/acp-7-2003-2007.

Robock, A., L. Oman, and G. Stenchikov (2007b), Nuclear winter revisited with a modern climate model and current nuclear arsenals: Still catastrophic consequences, *J. Geophys. Res.*, *112*, D13,107, doi:10.1029/2006JD008235.

Rosenfeld, D., and W. Woodley (2000), Deep convective clouds with sustained supercooled liquid water down to $-37.5°c$, *Nature*, *405*(6785), 440.

Rosenfeld, D., M. Fromm, J. Trentmann, G. Luderer, M. Andreae, and R. Servranckx (2007), The Chisholm firestorm: observed microstructure, precipitation and lightning activity of a pyro-cumulonimbus, *Atmos. Chem. Phys.*, *7*(3), 645–659.

Rosenfeld, D., U. Lohmann, G. Raga, C. O'Dowd, M. Kulmala, S. Fuzzi, A. Reissell, and M. Andreae (2008), Flood or drought: How do aerosols affect precipitation?, *Science*, *321*(5894), 1309–1313.

Sagan, C., R. Turco, P. Ehrlich, H. Geiger, and P. R. Archive (1983), *The nuclear winter*, Scott Meredith Literary Agency.

Saleeby, S., and W. Cotton (2008), A binned approach to cloud-droplet riming implemented in a bulk microphysics model, *J. Appl. Meteorol. Clim.*, *47*(2), 694–703.

Schoeberl, M., E. Jensen, L. Pfister, R. Ueyama, M. Avery, and A. Dessler (2018), Convective hydration of the upper troposphere and lower stratosphere, *J. Geophys. Res*, *123*(9), 4583–4593.

Schwartz, M., A. Lambert, G. Manney, W. Read, N. Livesey, L. Froidevaux, C. Ao, P. Bernath, C. Boone, R. Cofield, et al. (2008), Validation of the Aura Microwave Limb Sounder temperature and geopotential height measurements, *J. Geophys. Res.*, *113*, D15S11, doi:10.1029/2007JD008783.

Schwartz, M., W. Read, M. Santee, N. Livesey, L. Froidevaux, A. Lambert, and G. Manney (2013), Convectively injected water vapor in the North American summer lowermost stratosphere, *Geophys. Res. Lett.*, *40*(10), 2316–2321.

Setvák, M., D. Lindsey, P. Novák, P. Wang, M. Radová, J. Kerkmann, L. Grasso, S.-H. Su, R. Rabin, J. Šťástka, et al. (2010), Satellite-observed cold-ring-shaped features atop deep convective clouds, *Atmos. Res.*, *97*(1-2), 80–96.

Sherwood, S. (2002a), A microphysical connection among biomass burning, cumulus clouds, and stratospheric moisture, *Science*, *295*, 1272–1275.

Sherwood, S. (2002b), Aerosols and ice particle size in tropical cumulonimbus, *J. Climate*, *15*(9), 1051–1063.

Sherwood, S., and A. Dessler (2001), A model for transport across the tropical tropopause, *J. Atmos. Sci.*, *58*(7), 765–779.

Siddaway, J., and S. Petelina (2011), Transport and evolution of the 2009 Australian Black Saturday bushfire smoke in the lower stratosphere observed by OSIRIS on Odin, *J. Geophys. Res*, *116*(D6), D06,203, doi:10.1029/2010JD015162.

Simpson, J. (1980), Downdrafts as linkages in dynamic cumulus seeding effects, *J. Appl. Meteorol.*, *19*(4), 477–487.

Skamarock, W., J. Klemp, J. Dudhia, D. Gill, D. Barker, W. Wang, and J. Powers (2005), A description of the advanced research WRF Version 2, *NCAR Tech. Note NCAR/TN-475+STR*, p. 88 pp.

Solomon, S., K. Rosenlof, R. Portmann, J. Daniel, S. Davis, T. Sanford, and G. Plattner (2010), Contributions of stratospheric water vapor to decadal changes in the rate of global warming, *Science*, *327*, 1219–1223.

Stein, A., R. Draxler, G. Rolph, B. Stunder, M. Cohen, and F. Ngan (2015), NOAA's HYSPLIT atmospheric transport and dispersion modeling system, *B. Am. Meteorol. Soc.*, *96*(12), 2059–2077.

Stephens, G., D. Vane, R. Boain, G. Mace, K. Sassen, Z. Wang, A. Illingworth, E. O'Connor, W. Rossow, S. Durden, et al. (2002), The CloudSat mission and the A-Train, *B. Am. Meteorol. Soc.*, *83*(12), 1771–1790, doi:10.1175/BAMS-83-12-1771.

Thompson, S., and S. Schneider (1986), Nuclear winter reappraised, *Foreign Aff.*, *64*(5), 981–1005.

Thompson, S., V. Aleksandrov, G. Stenchikov, S. Schneider, C. Covey, and R. Chervin (1984), Global climatic consequences of nuclear war: simulations with three dimensional models, *Ambio*, pp. 236–243.

Toon, O., R. Turco, A. Robock, C. Bardeen, L. Oman, and G. Stenchikov (2007), Atmospheric effects and societal consequences of regional scale nuclear conflicts and acts of individual nuclear terrorism, *Atmos. Chem. Phys.*, *7*(8), 1973–2002, doi:10.5194/acp-7-1973-2007.

Torres, O., R. Decae, J. Veefkind, and G. De Leeuw (2002), OMI aerosol retrieval algorithm, OMI algorithm theoretical basis document: clouds, aerosols, and surface UV irradiance, Vol. 3, version 2, edited by P. Stamnes, NASA Goddard Space Flight Cent., Greenbelt, MD. (OMI-ATBD-03. Available at http://eospso.gsfc.nasa.gov/eoshomepage/forscientists/atbd/docs/OMI/ATBD-OMI-03.pdf).

Trentmann, J., G. Luderer, T. Winterrath, M. Fromm, R. Servranckx, C. Textor, M. Herzog, H.-F. Graf, and M. Andreae (2006), Modeling of biomass smoke injection into the lower stratosphere by a large forest fire (part i): reference simulation, *Atmos. Chem. Phys.*, *6*(12), 5247–5260.

Turco, R. P., O. B. Toon, T. P. Ackerman, J. B. Pollack, and C. Sagan (1983), Nuclear winter: global consequences of multiple nuclear explosions, *Science*, *222*(4630), 1283.

Turco, R. P., O. B. Toon, T. P. Ackerman, J. B. Pollack, and C. Sagan (1984), The climatic effects of nuclear war, *Sci. Am.*, *251*(2), 33–43.

Turco, R. P., O. B. Toon, T. P. Ackerman, J. B. Pollack, and C. Sagan (1990), Climate and smoke: An appraisal of nuclear winter, *Science*, *247*(4939), 166.

Uccellini, L., and D. Johnson (1979), The coupling of upper and lower tropospheric jet streaks and implications for the development of severe convective storms, *Mon. Wea. Rev.*, *107*(6), 682–703.

Vaughan, M. A., D. M. Winker, and K. A. Powell (2005), Part 2: Feature Detection and Layer Properties Algorithms, in *CALIOP Algorithm Theoretical Basis Document*, PC-SCI-202, p. 87 pp., Langley Research Center, Hampton, VA.

Walko, R., W. Cotton, M. Meyers, and J. Harrington (1995), New RAMS cloud microphysics parameterization part I: the single-moment scheme, *Atmos. Res.*, *38*(1-4), 29–62.

Wallace, J. (2003), General Circulation: Overview, in *Encyclopedia of Atmospheric Sciences*, edited by J. R. Holton, J. A. Curry, and J. A. Pyle, pp. 821–829, Academic.

Wang, H., W. Skamarock, and G. Feingold (2009), Evaluation of scalar advection schemes in the Advanced Research WRF model using large-eddy simulations of aerosol–cloud interactions, *Mon. Wea. Rev.*, *137*(8), 2547–2558.

Wang, P. (2003), Moisture plumes above thunderstorm anvils and their contributions to cross-tropopause transport of water vapor in midlatitudes, *J. Geophys. Res.*, *108*(D6).

Wang, T., and A. Dessler (2012), Analysis of cirrus in the tropical tropopause layer from CALIPSO and MLS data: A water perspective, *J. Geophys. Res.*, *117*, D04,211, doi:10.1029/2011JD016442.

Weisman, M., and J. Klemp (1982), The dependence of numerically simulated convective storms on vertical wind shear and buoyancy, *Mon. Wea. Rev.*, *110*(6), 504–520.

Winker, D., M. Vaughan, A. Omar, Y. Hu, K. Powell, Z. Liu, W. Hunt, and S. Young (2009), Overview of the CALIPSO mission and CALIOP data processing algorithms, *J. Atmos. Ocean. Tech.*, *26*(11), 2310–2323, doi:10.1175/2009JTECHA1281.1.

World Meteorological Organization (1992), *International Meteorological Vocabulary (2nd ed.)*, 636 pp., doi:(ISBN)978-92-63-02182-3.

Yan, H., Z. Li, J. Huang, M. Cribb, and J. Liu (2014), Long-term aerosol-mediated changes in cloud radiative forcing of deep clouds at the top and bottom of the atmosphere over the Southern Great Plains, *Atmos. Chem. Phys.*, *14*(14), 7113–7124, doi:10.5194/acp-14-7113-2014.